nature synthesis

Article

https://doi.org/10.1038/s44160-024-00679-2

Phase-switchable preparation of solution-processable WS_2 mono- or bilayers

Received: 22 March 2024

Accepted: 10 October 2024

Published online: 15 November 2024

Check for updates

Liang Mei[1,13], Zhan Gao[2,13], Ruijie Yang[1,13], Zhen Zhang[1,13], Mingzi Sun[3], Xiongyi Liang[1], Yuefeng Zhang[1], Ting Ying[1], Honglu Hu[1], Dengfeng Li[2], Qinghua Zhang[4], M. Danny Gu[5] ✉, Lin Gu[6], Jiang Zhou[7], Bolong Huang[3], Damien Voiry[8], Xiao Cheng Zeng[1], Yang Chai[9], Ju Li[10] ✉, Xinge Yu[2,11] ✉ & Zhiyuan Zeng[1,12] ✉

Crystal phase plays a crucial role in determining the properties of two-dimensional (2D) transition metal dichalcogenides. Here we achieve phase-switchable preparation of 2D transition metal dichalcogenides using an electrochemical lithium-ion intercalation-based exfoliation strategy by controlling the discharge current density and cutoff voltage. We discover that a small discharge current density (0.005 A g^{-1}, with a 0.9 V cutoff voltage) produces pure semiconducting 2H phase WS_2 bilayers. In contrast, a large discharge current density (0.02 A g^{-1}, with a 0.7 V cutoff voltage) leads to the dominant semimetallic 1T′ phase WS_2 monolayers. The phase-switching mechanism was clarified through cryo-electron microscopy, annular dark-field scanning transmission electron microscopy, Raman, X-ray photoelectron spectroscopy, etc. The device (humidity sensor) application of produced 2D WS_2 was then demonstrated, showing phase-dependent humidity-sensing performances confirming the potential of our produced 2D WS_2 with switchable phase in device applications.

The crystal phase is a pivotal parameter when determining the properties and applications of two-dimensional (2D) transition metal dichalcogenides (TMDs)[1–3]. Group-VI TMDs, such as MoS_2 and WS_2, can exist in diverse phases (2H, 1T or 1T′), depending on the coordination geometries of the transition metal atom (Supplementary Fig. 1). The 1T (octahedral coordination) and 1T′ (distorted octahedral coordination) group-VI TMDs exhibit metallic and semimetallic properties, respectively, rendering them promising candidates for applications in energy storage[4–6], energy conversion[7–10] and superconductivity[11]. In contrast, the 2H (trigonal prismatic coordination) group-VI TMDs are typically semiconductors with a bandgap of 1–2 eV (ref. 12), making them exceptionally well suited for applications in nanoelectronics and optoelectronics[13–15].

The preparation of 2D group-VI TMDs (solution-processable TMDs in particular) with a designated phase tailored to intended applications is therefore important, as solution-processable 2D TMDs are compatible with solution-based deposition techniques (such as inkjet printing, industrial roll-to-roll coating, drop-casting and spin-coating), facilitating the easy and scalable manufacture of customizable devices[16,17]. Although such printable 2D group-VI TMD solutions could be prepared via direct liquid exfoliation in solvents[18] and foreign species (for example, tetraalkylammonium ions[19,20], sulfate ions[21] and small molecules[22]) intercalation-based liquid exfoliation, the phase of the final 2D products is not adjustable, remaining the same phase as their initial bulk counterparts.

Previous studies suggest that 2H-to-1T/1T′ phase transition occurs in group-VI TMDs during lithium-ion (Li^+) intercalation-based exfoliation, resulting in 2D nanosheets (NSs) with a mixed phase of 2H and 1T/1T′[9,23,24]. In theory, this is because the Li^+ intercalation involves the electron injection from the *s* orbitals of guest lithium to the *d* orbitals of the host transition metal atoms to maintain overall charge neutrality[25]. When the electron injection is beyond a certain threshold (in terms of MoS_2, this threshold is 0.29 electrons per formula unit[19]), the stability of the 2H phase group-VI TMDs will be lower than that of the 1T or

A full list of affiliations appears at the end of the paper. ✉e-mail: m.danny.gu@gmail.com; liju@mit.edu; xingeyu@cityu.edu.hk; zhiyzeng@cityu.edu.hk

1T′ phase, causing the corresponding phase transition. The occurrence of phase transition implies that Li^+ intercalation-based exfoliation can theoretically become a plausible way for the preparation of solution-processable group-VI 2D TMDs with on-demand phases. Still, this has not yet been truly achieved experimentally, as the switch (on–off) for the phase transition is still unknown[24].

Here, we discover the electric switch of phase transition during the electrochemical Li^+ intercalation-based exfoliation, achieving phase-switchable exfoliation of solution-processable WS_2 mono- or bilayers from their bulk counterparts (Supplementary Fig. 2). Specifically, we found that Li^+ intercalation under a small discharge current density (0.005 A g^{-1}, with a 0.9 V cutoff voltage) will cause the formation of dense solid electrolyte interface (SEI) film at the edge of WS_2, which limits the insertion of Li^+ below the phase transition threshold, resulting in semiconducting 2H-WS_2 bilayers. Conversely, a large discharge current density (0.02 A g^{-1}, with a 0.7 V cutoff voltage) will lead to 2H-to-1T/1T′ phase transition and thereby produces semimetallic 1T′-WS_2 monolayers. In this case, no obvious SEI film is formed. Thus, Li^+ can be fully intercalated in WS_2, resulting in a phase transition. Our findings give new vitality to the electrochemical Li^+ intercalation-based exfoliation strategy, making it a feasible method for large-scale production of solution-processable group-VI 2D TMDs with designated phases.

Phase-switchable preparation and characterization

Figure 1a illustrates the overall phase-switchable preparation of 2H- and 1T′-WS_2 NSs using our electrochemical Li^+ intercalation-based exfoliation strategy with controllable discharge current density and cutoff voltage (small current density: 0.005 A g^{-1}, 0.9 V; large current density: 0.02 A g^{-1}, 0.7 V), (see Methods for details). These parameters were determined through a serial of control experiments with different discharge current densities and cutoff voltages. Detailed results are presented in Supplementary Fig. 3, which shows that the threshold discharge current density required to initiate the formation of 2H-phase WS_2 NSs is 0.005 A g^{-1}. Raman (Fig. 1d and Supplementary Fig. 4) and X-ray photoelectron spectroscopy (XPS; Fig. 1e and Supplementary Fig. 5) analyses confirmed this conclusion.

The small current density-driven Li^+ intercalation-based exfoliated WS_2 NS dispersion exhibits a light-green colour (Fig. 1b, inset and Supplementary Figs. 6 and 7), signifying partial absorption in the visible range, as verified via the ultraviolet–visible absorption spectrum (Fig. 1b), which confirm the formation of semiconducting 2H phase WS_2 NSs under a small discharging current density[19]. Conversely, the large current density exfoliated WS_2 NS dispersion shows a black colour (Fig. 1b, inset and Supplementary Figs. 6 and 7), indicating the complete and featureless absorption in the visible range (Fig. 1b), marking the emergence of phase transition and the formation of metallic 1T/1T′ phase WS_2 NSs under a large discharging current density. Photoluminescence (PL), Raman spectroscopy and XPS further confirm the above phase analysis. Prominent PL appears in small current density exfoliated WS_2 NSs (Fig. 1c), signifying its semiconducting nature (2H phase). Only two dominant peaks (the in-plane phonon E^1_{2g} at 350.3 cm^{-1} and the out-of-plane phonon A_{1g} modes at 419.2 cm^{-1}, corresponding to 2H WS_2 (ref. 11)) appear in the Raman spectroscopy of small current density exfoliated WS_2 NSs (Fig. 1d), indicating their 2H phase. By contrast, the J_1, J_2 and J_3 peaks located at low-frequency regions are observed for large current density exfoliated WS_2 NSs (Fig. 1d), indicative of the 1T′ phase[9]. The yields of 2H-WS_2 (under small current density) and 1T′-WS_2 (under large current density) NSs are ~100% and ~67%, respectively, as confirmed by the deconvolution of the W 4*f* regions of exfoliated WS_2 in the XPS spectrum (Fig. 1e).

The phases of exfoliated WS_2 NSs are further confirmed by aberration-corrected annular dark-field scanning transmission electron microscopy (ADF-STEM). The ADF-STEM image of the small current density exfoliated WS_2 NSs shows a hexagonal lattice structure of individual W and S atoms (Fig. 1f), confirming the 2H phase[20], whereas the one-dimensional zigzag chains of W atoms dominate the entire image of the large current density exfoliated WS_2 NSs (Fig. 1g), indicative of the 1T′ phase[26]. Notably, a small area of 2H phase is also observed in the top-right corner of the image (Fig. 1g), suggesting the co-existence of 1T′ and 2H phases in large current density exfoliated WS_2 NSs, and 1T′ phase is dominant. Figure 1f,g in the bottom part show line intensity profiles scan along the white-boxed atoms. The intensity of S atoms is much more pronounced in 2H WS_2 owing to the enhanced signal resulting from the overlap of two S atoms along the direction of the electron beam[27]. In contrast, for the 1T′-WS_2 structures, the intensity ratio of S atoms between the two W sites is much lower. This is attributed to the S atoms in the upper and lower layers being staggered, creating a triangular lattice.

Sulfur vacancies are clearly observed in the ADF-STEM images of the prepared 2H- and 1T′-WS_2 NSs (Supplementary Figs. 8 and 9), and the electron paramagnetic resonance (EPR) results indicate that the sulfur vacancies in 2H-WS_2 NSs are more abundant than those in 1T′-WS_2 NSs (Supplementary Fig. 10). Transmission electron microscopy (TEM) reveals that the exfoliated 2H- and 1T′-WS_2 NSs have a lateral size ranging from 300 to 600 nm and 100 to 200 nm, respectively (Supplementary Fig. 11). Large quantities of 2H- and 1T′-WS_2 NSs were successfully prepared as confirmed by scanning electron microscope images (SEM; Supplementary Fig. 12). Atomic force microscopy (AFM) images show that the thickness of the 2H- and 1T′-WS_2 NSs is 1.8 nm and 1.2 nm (Fig. 1h,i; thickness distribution histograms are shown in Supplementary Fig. 13), respectively, indicating the formation of bilayer 2H- and monolayer 1T′-WS_2 NSs. Besides WS_2, phase-switchable preparation of WSe_2 was also successfully achieved and characterized (see detailed information in Supplementary Figs. 14–16). However, this method is not suitable for MoS_2; only 1T′-MoS_2 NSs can be prepared (SupplementaryFigs. 17 and 18). This discrepancy might be due to the varying interaction energies between Li^+ and different TMDs.

Phase-switching mechanism

To investigate the phase-switching mechanism, cryo-TEM is employed due to the sensitivity of lithium discharged samples to electron beams[28]. When Li^+ intercalation is driven by a small discharge current density, a dense compact and amorphous SEI film and Li_2S at the edge of WS_2 are observed (Fig. 2a–c). The ADF-STEM and electron energy loss spectroscopy (EELS) analyses (Fig. 2f and Supplementary Fig. 19) indicate that lithium predominantly localizes within the SEI. There is a minimal presence of Li^+ intercalation occurring at the edge of WS_2 (ref. 29). This minimal Li^+ edge intercalation is revealed by a small increase in interlayer spacing from 6.19 Å to 6.26 Å (Supplementary Fig. 20). The hexagonal symmetry structure (Fig. 2b), A–B–A stacking mode (Fig. 2d) and greenish colour (Fig. 2e) of the intercalated WS_2 confirm the 2H polytype.

Fig. 1 | Preparation and characterization of 2H- and 1T′-WS_2 NSs. a, A schematic of the phase-switchable synthesis of 2H- and 1T′-WS_2 NSs through a controllable electrochemical lithium intercalation-based exfoliation method. **b**, Visible–near-infrared absorption spectra of exfoliated 2H- and 1T′-WS_2 NS solution. A, B and C indicate the three absorption peaks in the spectrum of exfoliated 2H-WS_2. The insets show the photographs of exfoliated 2H- and 1T′-WS_2 NS solution. **c**, PL spectra of exfoliated 2H- and 1T′-WS_2. **d**, Raman spectra of bulk WS_2 and exfoliated 2H- and 1T′-WS_2. **e**, XPS W 4*f* spectra of bulk WS_2 and exfoliated 2H- and 1T′-WS_2. **f**, ADF-STEM image of 2H-WS_2. The enlarged atomic-resolution image is presented in the left corner. Line intensity profile scans along the white-boxed atoms in the enlarged image are shown below. **g**, An ADF-STEM image of 1T′-WS_2. The enlarged atomic-resolution image is presented in the left corner. Line intensity profile scans along the white-boxed atoms in the enlarged image are displayed below. A small area of 2H-WS_2 was found in the top right corner. **h**,**i**, AFM images of 2H- (**h**) and 1T′-WS_2 (**i**) NSs. The inset height profiles reveal the thickness of selected NSs.

https://doi.org/10.1038/s44160-024-00679-2

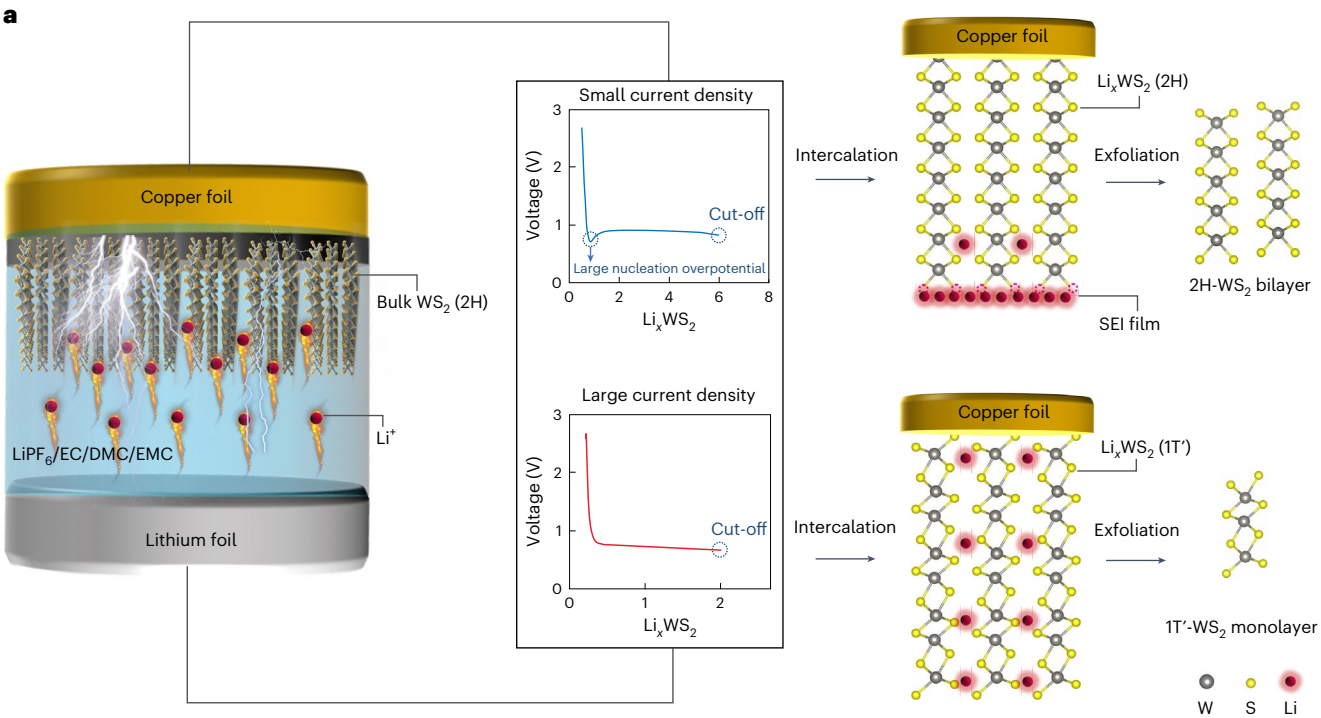

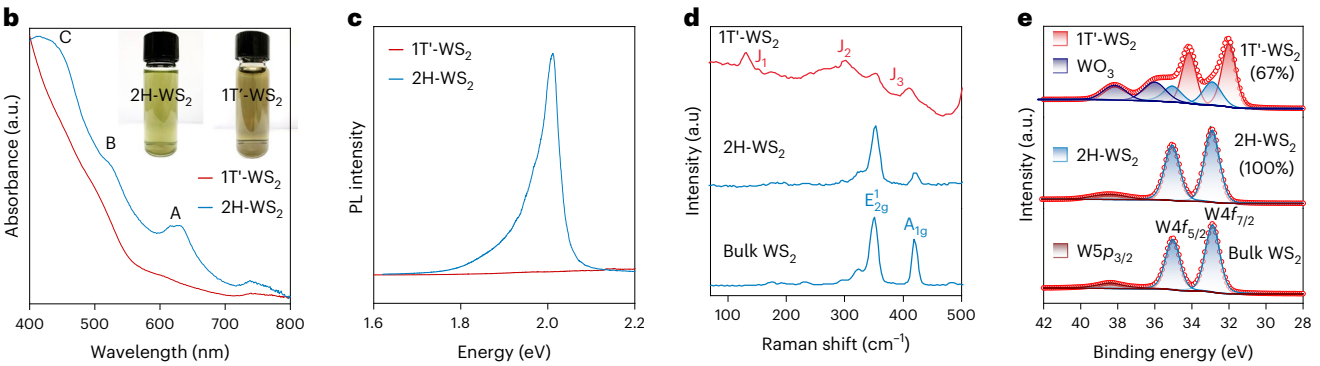

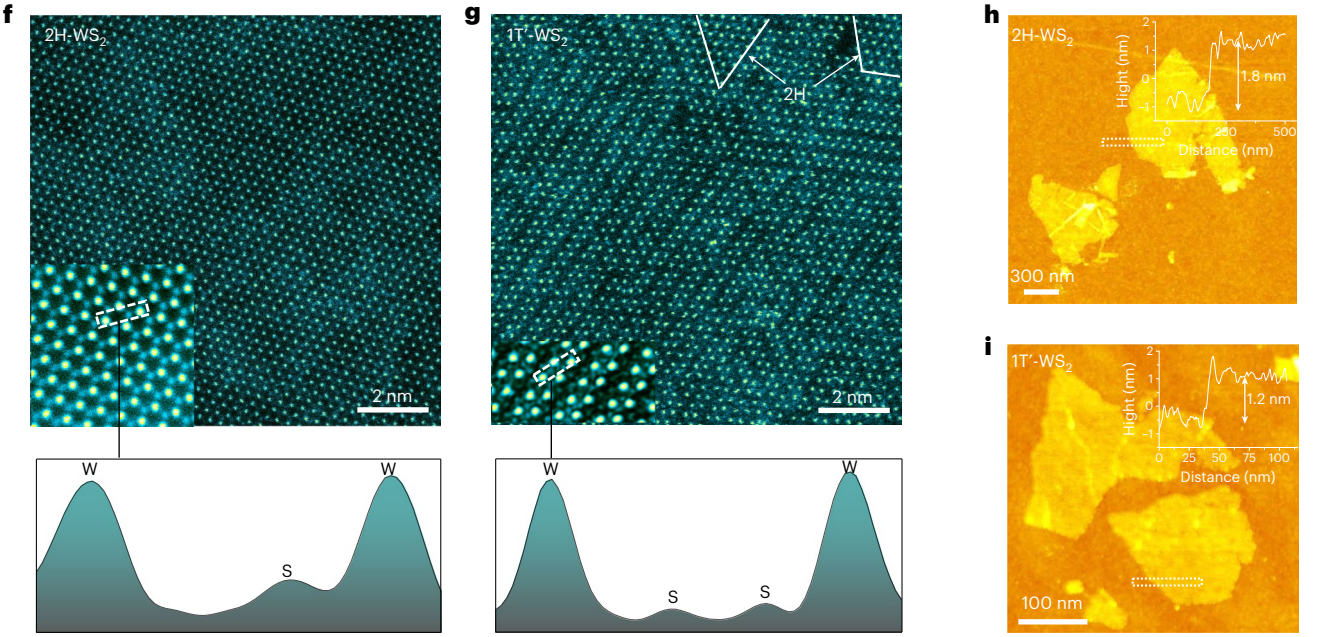

In contrast, when a large discharge current density is applied, no significant SEI film is observed at the edge of WS_2, but exfoliated WS_2 appears (Fig. 2g–i). The ADF-STEM image and high-resolution EELS mapping confirm that Li^+ indeed intercalates into the interior structure of WS_2 (Fig. 2l and Supplementary Fig. 21). The distorted A–B–C stacking mode (Fig. 2j) and the black colour (Fig. 2k) of the intercalated WS_2 reveals the 1T′ phase. The XPS (Supplementary Figs. 22–24) and X-ray diffraction (Supplementary Fig. 20) characterizations further confirmed the 2H phase of small current density intercalated WS_2 and the 1T′ phase of large current density intercalated WS_2.

Bringing together the findings from the analyses mentioned above, it becomes evident that a small discharge current density results in the creation of a dense SEI films at the edge of WS_2, which acts as a barrier preventing Li^+ intercalation into the interlayer of WS_2 and thereby limits the electron injection (from the *s* orbitals of lithium to the *d* orbitals of the W atom) below the phase transition threshold (0.3 electrons per WS_2 formula unit, as confirmed by density functional theory (DFT) calculation; Supplementary Figs. 25–27 and Supplementary Table 1). This, in turn, results in the phase of the final product being consistent with the starting bulk materials (both being 2H phase) without a phase transition. Furthermore, the SEI caused irreversibility during the intercalation process, which is revealed through the charge–discharge curves (Supplementary Fig. 28) and corresponding EPR results (Supplementary Fig. 29). Conversely, a large discharge current density does not allow for the establishment of a well-defined SEI film; therefore, Li^+ can be fully intercalated into the interlayer of WS_2. This process causes a charge density wave and a transition from the 2H phase to the 1T′ phase, which, in turn, results in the dominance of 1T′ phase in the final product.

To explain how the discharge current density influences SEI formation and ultimately affects WS_2 phase transition, we conducted theoretical simulations. The large and small discharge current densities were simulated as the high and low concentrations of Li^+ near WS_2. We also introduced different external electric fields along the WS_2 layers as the reaction potentials. It is observed that, under different potential conditions, smaller potentials promote the Li^+ diffusions into the WS_2 interlayers (Supplementary Fig. 30a,b). This proves that a higher discharge current density with lower reaction potential benefits the thorough diffusions of Li^+ into the WS_2 interlayers. For the smaller discharge current density with lower Li^+ concentration, the single Li^+ diffusion into the WS_2 interlayer is challenging due to the increasing energy barriers, indicating that the lower-concentration Li^+ are prone to be limited near the edge of WS_2 (Supplementary Fig. 30c).

During the molecular dynamics (MD) simulations of high-concentration Li^+, the intercalation of Li^+ into the WS_2 layers is clearly observed, which results in the exfoliations of WS_2 layers (Supplementary Fig. 30d–f). In addition, the WS_2 layers experience the formation of superstructure rather than the amorphizations, which initiates the phase change to 1T′ structures under the high discharge current density. In contrast, when the WS_2 layers are interacting with a small concentration of Li^+ under a low discharge current density, we notice that the strong interactions with the WS_2 layer are limited only near the edge by strong adsorptions, which induces the evident amorphization of WS_2 towards the SEI formation (Supplementary Fig. 30g–i). In addition, the interlayer spaces are blocked by Li–S bonding and the amorphous structures, which further hinder the diffusions of the Li^+ into the WS_2 interlayers and maintain the original 1H structures. These observations are supportive of experimental results and confirm that the diffusion behaviours of Li^+ are strongly related to the discharge condition, supplying important insights into the understanding of SEI formation and WS_2 phase change.

Device applications

Since the prepared 1T′-WS_2 monolayers and 2H-WS_2 bilayers possess high surface areas and exposed sulfur atoms, they are ideal platforms for humidity sensors. In addition, different phases of WS_2 interact with H_2O molecules in distinct ways. The solution-prepared 2H- and 1T′-WS_2 NSs are therefore examined for humidity sensor applications. Drop-casting is used to deposit the WS_2 NSs onto a polyethylene terephthalate (PET) substrate. After drying, Au electrodes are sputtered onto WS_2 NSs for wiring purposes (Fig. 3a and Supplementary Fig. 31). The basic humidity-sensing properties are investigated using a home-made humidity sensor test system (Supplementary Fig. 32).

The significant variations in device current under different relative humidity (RH) conditions indicate a wide humidity response range of our fabricated 2H-WS_2 humidity sensor (Fig. 3b,c). As the RH varies from 15% to 90%, the current of the devices at a bias of 10 V increases by nearly two orders of magnitude, suggesting excellent humidity-sensing capabilities of our device. Notably, the 2H-WS_2 humidity sensor exhibits a stronger response when the applied RH exceeds 65%, signifying that such a humidity sensor is well suited for applications requiring detection in high-humidity environments, such as breath rate monitoring and non-touch positioning interfaces. This behaviour can be explained by the presence of two distinct conduction mechanisms corresponding to different humidity ranges (refer to Supplementary Figs. 33 and 34)[30]. The dynamic humidity response and recovery measurements of the WS_2 humidity sensors are shown in Fig. 3d, demonstrating excellent selectivity and repeatability when responding to different levels of RH. Response and recovery times are crucial parameters that determine the sensitivity of humidity sensors. Figure 3e shows the repeatable dynamic humidity response of the 2H-WS_2 humidity sensors from RH 60% to RH 75%, demonstrating ultrafast response and recovery times below 1 s. An enlarged *I*–*T* (*I*, current; *T*, time) curve (Fig. 3f) reveals that the response and recovery times for 2H-WS_2 humidity sensor are 0.48 s and 0.32 s, respectively. In comparison, these values are 0.30 s and 1.20 s for the 1T′-WS_2 humidity sensor tested under the same conditions (Fig. 3g,h). Compared with the 2H-WS_2 humidity sensor, the 1T′-WS_2 humidity sensor exhibits a faster response but a slower recovery time. This difference can be attributed to the fact that 1T′-WS_2 has more negative adsorption energy towards water molecules than 2H-WS_2 (Supplementary Figs. 35 and 36, −0.73 eV versus −0.18 eV), implying that water molecules are more easily adsorbed on 1T′-WS_2. Conversely, water molecules are more challenging to desorb from the surface of 1T′-WS_2, resulting in a longer recovery time.

When comparing the response and recovery times with other reported humidity sensors, both our fabricated 2H- and 1T′-WS_2 sensors demonstrate the fastest recovery and response times (Fig. 3i and

Fig. 2 | Characterization of intercalated WS_2. **a**, A cryo-TEM image of a small current density intercalated WS_2 electrode, showing the amorphous SEI and Li_2S on the surface of WS_2. **b**,**c**, High-resolution (HR)TEM images of WS_2 (**b**) and Li_2S (**c**) shown in **a**. The insets in **b** and **c** are the corresponding diffraction patterns. The lattice distances of 0.28 and 0.27 nm are attributed to the (010) and (10$\bar{1}$) planes of WS_2 (**b**). For Li_2S (**c**), the lattice distances of 0.32 and 0.19 nm correspond to the (200) and (020) planes, respectively. **d**, A cross-sectional ADF-STEM image of small current density intercalated WS_2. The red and yellow circles denote the W and S atoms, respectively. **e**, An optical image of small current density intercalated WS_2 electrodes after the discharging process. **f**, An ADF-STEM image and EELS elemental mapping of small current density intercalated WS_2. **g**, A cryo-TEM image of a large current density intercalated electrode showing exfoliated WS_2 on the surface. **h**,**i**, HRTEM images of WS_2 (**h**) and surface exfoliated WS_2 (**i**) shown in **g**. The insets in **h** and **i** are the corresponding diffraction patterns. The lattice distances of 0.27 and 0.21 nm are attributed to the (100) and (01$\bar{4}$) planes of WS_2 (**h**). The lattice distance of 0.63 nm corresponds to the (002) plane of WS_2 (**i**). **j**, A cross-sectional ADF-STEM image of large current density intercalated WS_2. The red and yellow circles denote the W and S atoms. **k**, An optical image of large current density intercalated WS_2 electrodes after the discharging process. **l**, An ADF-STEM image and EELS elemental mapping of large current density intercalated WS_2.

https://doi.org/10.1038/s44160-024-00679-2

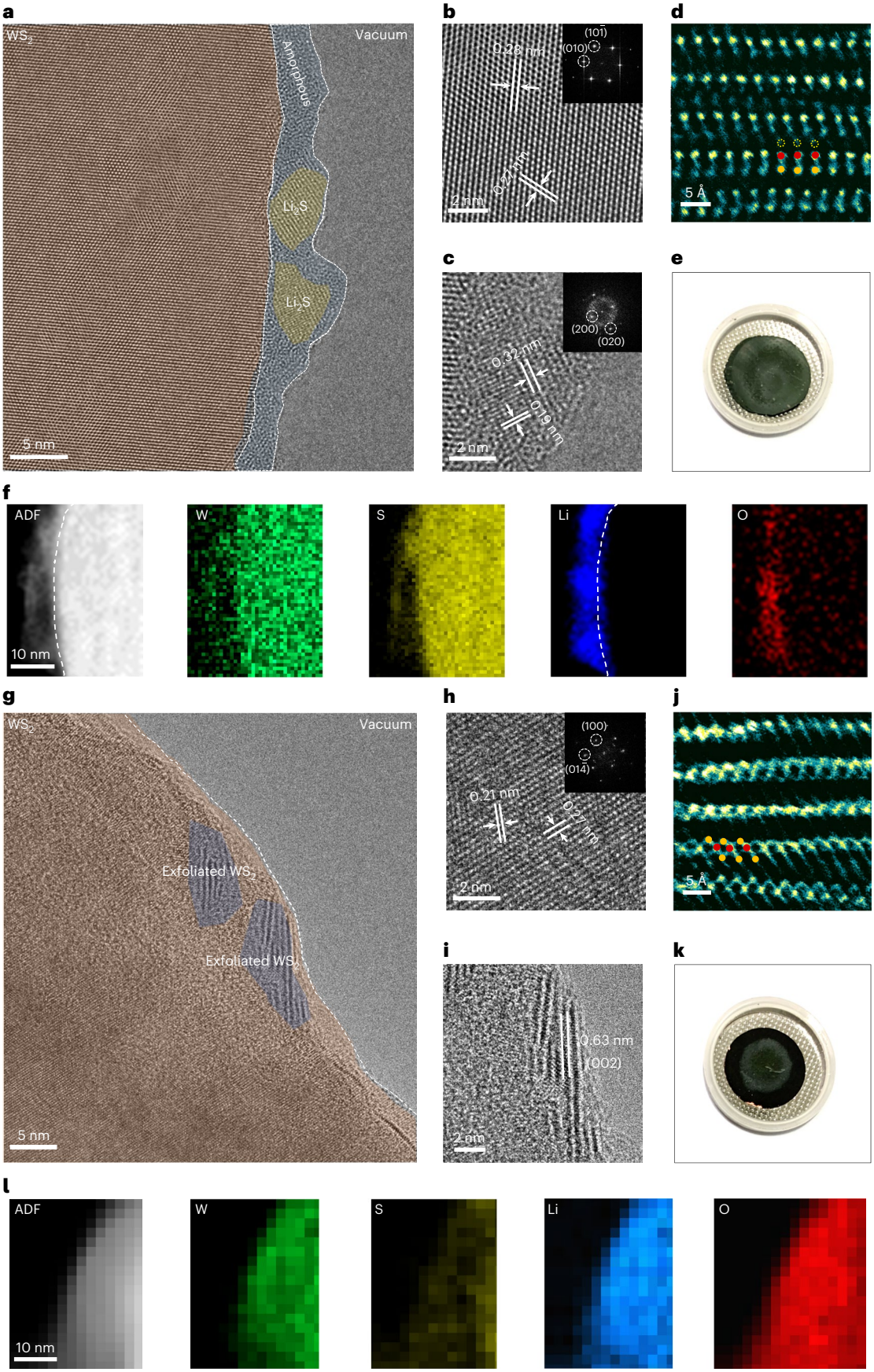

https://doi.org/10.1038/s44160-024-00679-2

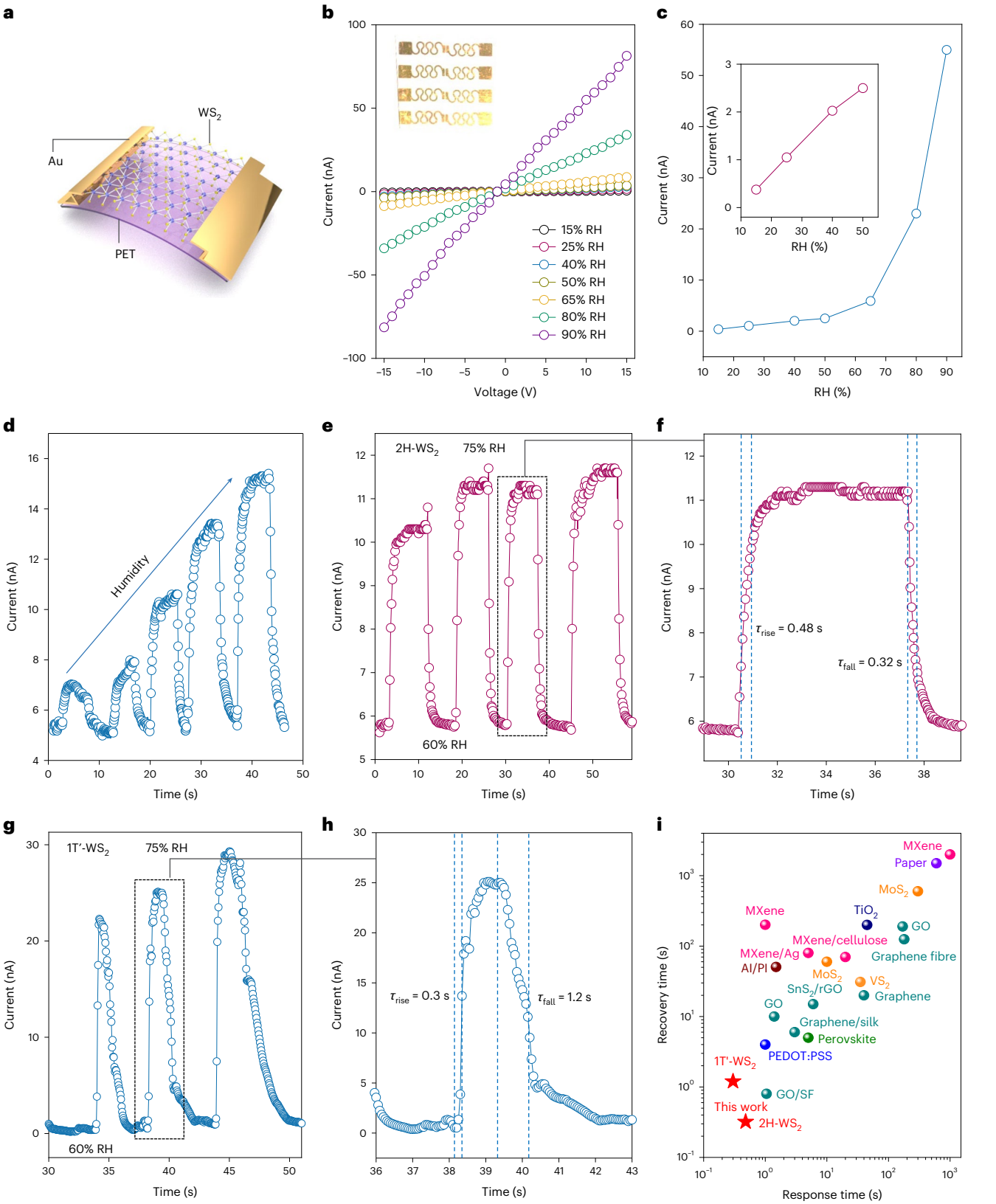

Fig. 3 | Humidity-sensing performance. a, A schematic illustration of the WS_2-based humidity sensor. **b**, *I*–*V* measurement of 2H-WS_2 humidity sensor under different levels of RH. *I*, current; *V*, voltage. **c**, *I*–RH curves. The inset is the enlarged curve of low RH levels between 15% and 50%. **d**, The dynamic humidity response and recovery measurement under different levels of RH. **e**, The response and recovery curve of 2H-WS_2 from 60% RH to 75% RH. **f**, The amplified response and recovery curve from **e**. τ_{rise} and τ_{fall} represent response and recover times. **g**, The response and recovery curve of 1T′-WS_2 from 60% RH to 75% RH. **h**, The amplified response and recovery curve from **g**. **i**, A comparison of the humidity-sensing performance of fabricated 2H- and 1T′-WS_2 NSs with other reported humidity sensors in literatures. MXene reprents transition metal carbides, nitrides and carbonitrides. GO/SF denotes graphene oxide and silk fibroin, and PEDOT refers to poly(3,4-ethylenedioxythiophene) polystyrene sulfonate. The details can be found in Supplementary Table 2.

Supplementary Table 2). The origin of short recovery and response time in Fig. 3i is due to the ultrathin structure of the exfoliated WS_2 NSs and the presence of abundant S defects. Specifically, the prepared 1T′-WS_2 and 2H-WS_2 NSs, being monolayer and bilayer, respectively, are significantly thinner than other humidity sensor materials, as shown in Fig. 3i. The prepared 1T′-WS_2 and 2H-WS_2 materials possess an exceptionally high surface-to-volume ratio, which results in a greater number of atoms being exposed on the surface, enhancing the interaction with water molecules. This high surface area facilitates increased adsorption of water molecules, leading to substantially increased changes in electrical properties (Supplementary Fig. 33) and, consequently, higher sensitivity to humidity variations[31]. Hence, the minimal thickness of these 2D materials enables rapid adsorption and desorption of water molecules, contributing to faster response and recovery times. Furthermore, the prepared 1T′-WS_2 and 2H-WS_2 NSs possess abundant sulfur defects (as confirmed by the EPR spectra in Supplementary Fig. 10), which enhance conductivity (as confirmed by DFT calculations in Supplementary Fig. 37)[32] and subsequently shorten the response time and improve the recovery speed. These factors sufficiently explain the short response and recovery times observed in our prepared 1T′-WS_2 and 2H-WS_2 NSs, as illustrated in Fig. 3i. Based on the relatively faster response and recovery speed, 2H-WS_2 NSs were selected for the following humidity-sensing demonstration.

The mechanical properties of the 2H-WS_2 humidity sensor are examined by analysing its response current under RH 65% after subjecting it to different cycles of bending. The WS_2 humidity sensor demonstrates exceptional flexibility, with the response current remaining nearly unchanged even after 1,300 cycles of bending (Fig. 4a). This resilience can be attributed to the use of exfoliated WS_2 NSs, which are intrinsically flexible ultrathin 2D materials with a high fracture strain of approximately 25–30% (refs. 33–35). These properties significantly contribute to the stability of the fabricated devices. Leveraging the highly sensitive and ultrafast response and recovery properties, we demonstrate the application of our WS_2 humidity sensor for breath monitoring, a critical aspect of diagnosing and treating slowly progressing diseases with few early indicators (for example cancer, diabetes and sleep apnoea–hypopnoea syndrome)[36]. The WS_2 humidity sensor is easily attached under the human nose to demonstrate nasal breath monitoring. As shown in Fig. 4b, the device's current value simultaneously varies in response to changes in breath rate. During the 3–7 s of measurement, the tested subject took a deep breath and exhaled a high RH level flow, resulting in a significant rise and fall in current. Subsequently, the subject breathes at a quick and uneven rate within 8 s, leading to low-amplitude and high-frequency fluctuations in the device's current. These results demonstrate that the ultrafast response and recovery properties of the WS_2 humidity sensor can effectively support precise real-time breath monitoring. In addition, the WS_2 humidity sensor can be employed to test the protective performance of various types of mask (Supplementary Fig. 38), which holds significant importance, such as during the coronavirus disease 2019 epidemic.

A prototype speech recognition device has also been developed. When a person speaks, the pronunciation of different words leads to variations in the concentration of exhaled water vapour. As shown in Supplementary Fig. 39, the ultrafast response and recovery of the WS_2-based humidity sensor allow it to detect real-time changes in breath humidity associated with spoken words. Consequently, this generates characteristic current curves corresponding to each word. Supplementary Figs. 40–43 shows the characteristic current curves recorded by the device for various spoken words, including 'Hi', 'people', 'thank you', 'you are welcome', 'question', 'unbelievable' and 'beautiful'. These current response curves exhibit unique and distinct characteristic peaks with high repeatability, highlighting the device's significant potential for voice recognition applications.

The long-range manipulation of devices offers promising potential for future electronics, particularly in applications like non-touch switches and touchless localization interfaces. Moisture detection can serve as a compelling stimulus signal to enable these innovative applications[37–39]. The high sensitivity and rapid responsiveness of the fabricated WS_2 humidity sensor are more than capable of meeting the requirements for real-time touchless localization interfaces. As illustrated in Fig. 4c (inset), the human finger serves as the moisture source. Quantitative measurements under a bias of 10 V in Fig. 4c demonstrate an exponential relationship between finger distance and the response current of a single WS_2 humidity sensor. The sensor begins to show a slight response at a vertical height of 6 mm that gradually increases as the finger approaches. Figure 4d reveals the dynamic current of the device in response to an approaching finger in an indoor environment. Benefitting from the ultrafast response and recovery time, the device's current increases as the finger approaches without any hysteresis. Furthermore, the superior stability of the WS_2 humidity sensor is confirmed by exposing it to the indoor environment (65% RH, room temperature) for 96 h (Supplementary Fig. 44).

Prompted by the excellent response capabilities, a touchless localization interface can be realized using the WS_2 humidity sensor array. Figure 4e shows a 5 × 5 WS_2 humidity sensor array on a PET substrate. The as-fabricated touchless localization interface retains its flexibility as demonstrated in Supplementary Fig. 45. Even under bending conditions, the response and recovery properties remain nearly unchanged compared with the flat condition. The successful distinction of the relative position and depth of two fingers using the WS_2-based localization interface is showcased in Fig. 4e,f. To enhance the image quality, we use the interpolation function in origin software to obtain a higher-density and clearer current distribution map (the original array density is 5 × 5, and the initial current distribution of the array is summarized in Supplementary Fig. 46). The current distribution map in Fig. 4f reveals the location of the two fingers, with colours indicating the vertical distance between the fingers and the sensor array. By incorporating the information of the location and depth of the fingers in a three-dimensional (3D) cuboid, a reconstructed 3D model that closely resembles the actual positions of the two fingers can be achieved (Fig. 4f). These results suggest that the WS_2-based localization interface can be employed to reconstruct the spatial distribution of subjects on the basis of moisture stimulus signals. Furthermore, due to its fast response and recovery properties, real-time location monitoring can be realized using our touchless localization interface. As shown in Fig. 4g,h, the contour map of the current distribution can reveal the areas covered by fingers as a single finger sweeps past our touchless localization interface at a very low height. To highlight the reconfigurability and advantages of the humidity sensor array, we showcase its potential application in monitoring baby diaper wetness. The detailed results and analysis are shown in Supplementary Fig. 47.

Conclusions

This study demonstrates the successful realization of a phase-switchable synthesis for solution-processable 2H- and 1T′-WS_2 NSs. An electrochemical Li^+ intercalation-based exfoliation strategy with precise control over Li^+ intercalation electrochemistry was developed. We found that a small discharge current density results in the production of pure semiconducting 2H phase WS_2 bilayers, while a large discharge current density leads to the prevalence of semimetallic 1T′ phase WS_2 monolayers. The phase-switching mechanism is clarified through cryo-electron microscopy, ADF-STEM, Raman, XPS, etc. The device application potential of the produced solution-processable 2D WS_2 is demonstrated. Together, our work presents a phase engineering method for the exfoliation of solution-processable 2D TMDs with implications in future electronics.

https://doi.org/10.1038/s44160-024-00679-2

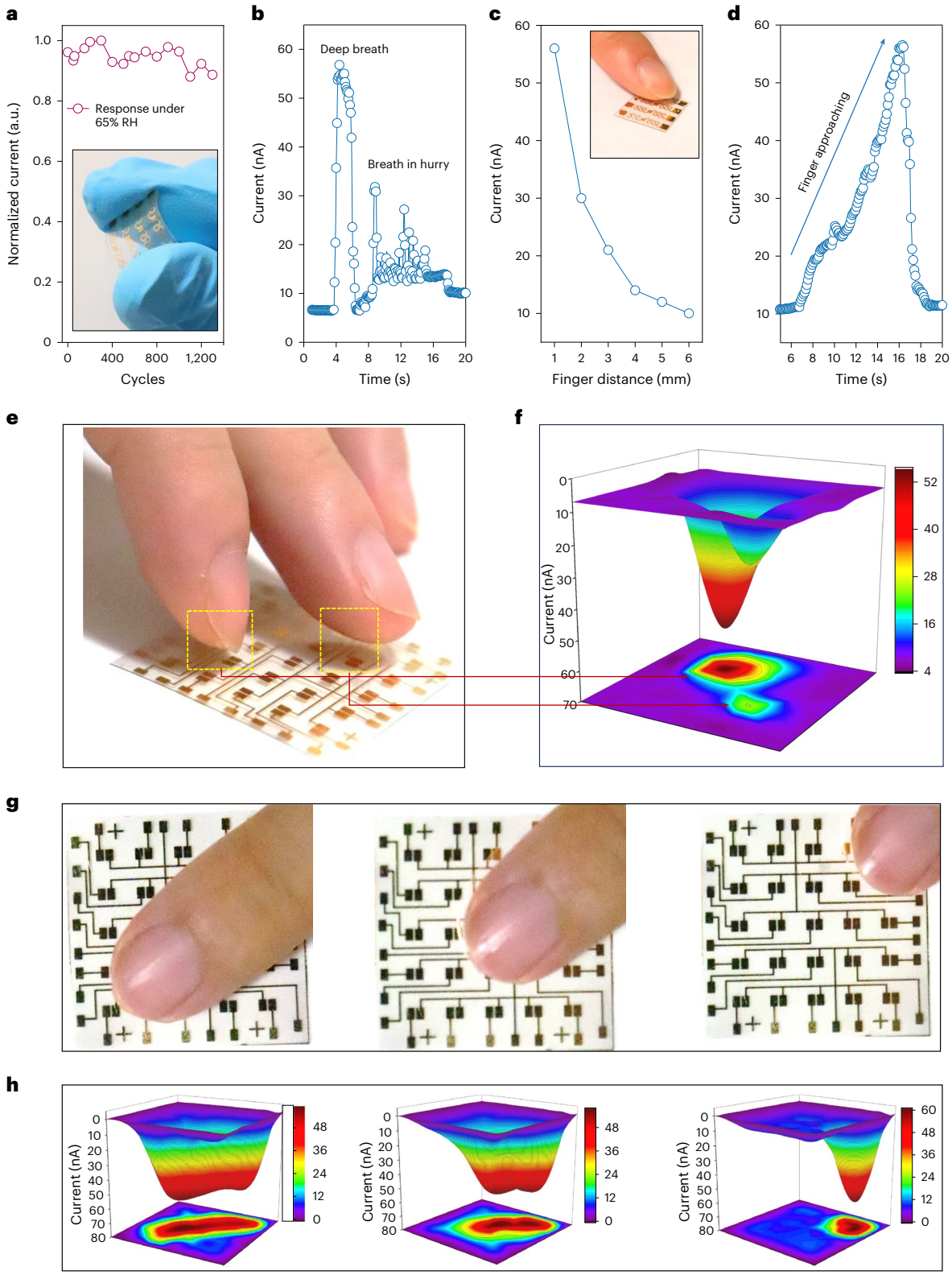

Fig. 4 | Sensor array for touchless localization interfaces. a, Mechanical property measurement of the WS_2 humidity sensor. The inset shows the flexibility of the device. **b**, Nasal breath monitoring curve. **c**, Quantitative measurement between finger distance and device current under a bias of 10 V. The inset shows the finger approaching the device. **d**, The dynamic current curve of the WS_2 humidity sensor as the finger approaches. **e**, An optical image of the relative localization of two approaching fingers above the 5 × 5 arrays. **f**, The corresponding 3D mapping of the approaching of two fingertips. **g**, Optical images of the finger sweeping above the touchless localization interfaces based on the WS_2 humidity sensor array. The corresponding 3D mapping of current distribution is shown in **h**.

Methods

Chemicals

Tungsten disulfide (WS_2, 99.9%, Macklin), carbon black (Bay Carbon), polyvinylidene difluoride (Sigma-Aldrich), 1-methyl-2-pyrrolidinone (99%, J&K Scientific), copper foil (Shenzhen Kejing Star Technology Company), lithium foil (DoDoChem), polypropylene film (Celgard 2300), Li^+ battery electrolyte (1.0 M $LiPF_6$ in ethylene carbonate (EC):dimethyl carbonate (DMC):ethyl methyl carbonate (EMC) = 1:1:1 vol%, DoDoChem), 3-aminopropyltriethoxysilane (99%, Aladdin), acetone (American Chemical Society grade, Anaqua Global International), ethanol (American Chemical Society reagent, ≥99.5%, Macklin). The deionized water was purified using Milli-Q System (Millipore).

Synthesis of 2H- and 1T′-WS_2 NSs

The 2H- and 1T′-WS_2 NSs were synthesized through a precise electrochemical Li^+ intercalation-based exfoliation process. This method was carried out within a coin cell setup, utilizing a copper foil-coated bulk WS_2 cathode (weighing 5 mg), lithium foil as the anode and an electrolyte solution comprising lithium hexafluorophosphate ($LiPF_6$) dissolved in a mixture of EC, DMC and EMC in a 1:1:1 volume ratio. A galvanostatic discharge was applied to initiate the Li^+ intercalation of the bulk WS_2. Upon completion of the intercalation process, the resulting lithium-intercalated WS_2 (Li_xWS_2) was carefully extracted from the coin cell and subjected to sonication in appropriate solvents to achieve exfoliation. The key differences in the synthesis of 2H- and 1T′-WS_2 NSs are associated with the specific discharge current density and cutoff voltage settings during the galvanostatic discharge. For the production of 2H-WS_2 NSs, these critical parameters were established at 0.005 A g^{-1} and 0.9 V, whereas for 1T′-WS_2 NSs, the parameters were fine-tuned to 0.02 A g^{-1} and 0.7 V (the galvanostatic discharge curves are shown in Supplementary Fig. 3). In addition, 2H-WS_2 NSs were prepared by sonication in ethanol, whereas 1T′-WS_2 NSs were fabricated through sonication in deionized water. Following the sonication step, both the 2H- and 1T′-WS_2 suspensions underwent centrifugation and multiple washing steps before being ultimately redispersed in a solvent for further characterization and device fabrication.

Characterizations

The following instruments were used in our experiments: ADF-STEM (JEOL ARM200F spherical aberration-corrected transmission electron microscope operated at 200 kV), TEM (FEI talosf200s), cryo-TEM (Titan Krios G3i, operating at 300 kV and equipped with a Ceta-D camera, Falcon 3 direct electron detector, and Gatan K3 direct electron detector camera), SEM (JSM-7600), XPS (Thermo Scientific K-Alpha Nexsa), AFM (Dimension 3100), Raman spectroscopy (WITec alpha 300 confocal Raman microscope, 532 nm), X-ray diffraction (D2 PHASER XE-T, Cu Kα radiation source, 30 kV voltage and 10 mA current), ultraviolet–visible spectrophotometry (UH 4150 UV, Hitachi), EPR (Bruker A300) and zeta potential analysis (Malvern Zetasizer Nano series). Lithiated WS_2 (small discharge current density Li^+-intercalated WS_2 (S-Li_xWS_2), large discharge current density Li^+-intercalated WS_2 (L-Li_xWS_2)) were injected via glove box to prevent oxidation.

Fabrication of WS_2-based device

The PET substrate (1.5 × 1.5 cm^2) underwent a thorough cleaning process in an ultrasonic bath. It was sequentially cleaned with detergent water, acetone, deionized water and isopropyl alcohol, with each cleaning step lasting for 15 min. After this cleaning procedure, an ethanol dispersion of exfoliated WS_2 NSs (32 mg l^{-1}) was drop-cast onto the PET substrate and allowed to dry at room temperature. Finally, 200-nm-thick Au electrodes were sputtered onto the PET substrate using a QUORUM #Q150TS Dual target sputtering system, employing a designed metal mask.

In the fabrication of the WS_2-based sensor array, the PET substrates underwent the previously described cleaning process. Following this, a circuit design based on Au was meticulously created using the QUORUM #Q150TS Dual target sputtering system, with the aid of a precisely designed metal mask. Subsequently, a custom metal mask with a rectangular array pattern was accurately affixed onto the as-fabricated circuit. This attachment was made using specific counterpoints to ensure accuracy. An ethanol dispersion of WS_2 NSs (32 mg l^{-1}) was then drop-cast onto the substrate. Afterwards, the mask was carefully removed once the solution had completely dried, leaving the WS_2 NSs in the desired pattern on the substrate.

Humidity-sensing tests

The humidity-sensing performance was evaluated within a custom-made sealed container, as depicted in Supplementary Fig. 32. Various humidity levels were precisely controlled by adjusting the mass flow of dry and moistened argon gas that was introduced into the container. The chip carrier was connected to external measurement equipment (Keysight B1500A Semiconductor Analyze) for conducting the tests. For the breathing test, a humidity sensor was placed under the nose or on masks to monitor exhaled gas humidity at different breathing rates. In the humidity sensing of the finger approach experiment, the sensor was positioned horizontally, and a finger was gradually brought closer from above. For touchless localization, the finger was held at a fixed height above the sensor array, and the current of each sensor was measured. In the voice recognition test, the sensor was placed 5 cm in front of the subject's mouth, and current changes were recorded as they pronounced English words with different lengths. All sensor currents were recorded in real time using a Keysight B1500A Semiconductor Analyzer.

Cryo-transfer procedure and sample preparation

In ambient air at room temperature, the highly reactive SEI components present on the surface of WS_2 can be susceptible to damage and crystalline amorphization when subjected to electron beam irradiation under TEM mode. To overcome these challenges, we employed super-low-dose and cryogenic-TEM techniques. Following the completion of the discharge process, the coin cells were carefully disassembled within an argon-filled glovebox (with H_2O and O_2 levels maintained below 0.01 ppm). The lithiated WS_2 electrodes, discharged at different current densities, were briefly rinsed with dimethyl carbonate for 30 s to eliminate excess lithium salts from their surfaces. Subsequently, the electrodes were allowed to dry inside the glovebox. After drying, the electrodes were gently scraped into a powder form using a blade and then dispersed onto a copper TEM grid. This copper grid was securely placed within a four-hole sample holder, sealed tightly and then immersed directly into a liquid nitrogen bath to prevent any contact with oxygen and moisture. The sealed cryo-electron microscopy sample holder was transferred to the cryo-electron microscopy auto-sampler system using liquid nitrogen. All data in this study were acquired using the low-dose cryo-electron microscopy platform. Throughout the entire experimental process, the sample temperature was meticulously maintained at 80 K. The high-resolution TEM images had a resolution of 4,096 × 4,096 pixels, with exposure times varying from 10 to 20 s and an electron dose rate of 10–15 e $Å^{-2}$ s^{-1}. Cryo-STEM EELS mapping data were collected using the Gatan K3 direct electron detector camera with a probe current of 50 pA.

Theoretical calculations

To investigate the interactions between WS_2 and Li^+ ions under different discharge current density conditions, we applied the Forcite package to perform MD simulations and to compute diffusion barriers of Li^+ ions. Three layers of 2H-WS_2 were constructed in an 8 × 8 supercell. Forty-eight Li^+ ions with random distributions were introduced near the WS_2 structure as the high discharge current density conditions. In comparison, we reduced the number of Li^+ ions to 12 as the low discharge current density. Meanwhile, the external electric field was also introduced

along the *y* axis to align with the WS_2 layers. The MD simulations were under NVT mode at 298 K for 1 ns with 1 fs step size, and the Anderson strategy was used to control the temperature during MD simulations.

The calculations for H_2O adsorption energy and partial density of states in WS_2 were conducted using spin-polarized within the Vienna Ab-initio Simulation Package code[40]. The Perdew–Burke–Ernzerhof version of the generalized gradient approximation[41] was employed to describe the exchange-correlation density functional. The cutoff energy for the plane-wave basis was set to 420 eV, and *k*-point meshes were generated according to the Monkhorst–Pack scheme. The projected augmented wave potentials were utilized to solve the electronic structure self-consistently using a *k*-point mesh of 8 × 8 × 1 and 3 × 3 × 1 for unit cell and supercell of size 3 × 3 × 1, respectively. The electronic relaxation was performed within an energy tolerance of 10^{-6} eV for self-consistency, while ionic optimizations continued until all the residual forces were smaller than 0.02 eV $Å^{-1}$. W d^4s^2 and S s^2p^4 electrons were treated as valence electrons. A vacuum region of 15 Å was set to avoid the interaction along the *z* direction between adjacent images.

For calculations of phase formation energy for different intercalated Li amounts in Li_xWS_2, the ion–electron interaction was described using the projector augmented-wave method with a kinetic energy cutoff of 600 eV. Van der Waals interactions were considered using Grimme's DFT-D3 method[42]. Tighter convergence criteria (10^{-8} eV for energy and 10^{-5} eV $Å^{-1}$ for force) and a denser Monkhorst–Pack grid (8 × 8 × 8) were applied for unit cell geometric optimization. To investigate interactions between WS_2 and Li atoms, the calculations were conducted until the total energy and force values reached less than 10^{-5} eV per atom and 0.02 eV $Å^{-1}$, respectively. For sampling the Brillouin zone, a Monkhorst–Pack *k*-point grid of 5 × 5 × 5 was used. To evaluate the thermal stability of Li-intercalated WS_2, the formation energy (ΔH_f) was calculated and can be expressed by $\Delta H_f = E_{total} - \sum_i \mu_i x_i$, where ΔE_{total} represents the DFT total energy of the compound, μ_i is the chemical potential of element *i* and x_i is the quantity of element *i* in the compound.

Data availability

The data that support the findings of this study are available within the article and its Supplementary Information. Source data are provided with this paper.

References

1. Yang, R. J. et al. Intercalation in 2D materials and in situ studies. *Nat. Rev. Chem.* **8**, 410–432 (2024).
2. Mei, L. et al. Metallic 1T/1T' phase TMD nanosheets with enhanced chemisorption sites for ultrahigh-efficiency lead removal. *Nat. Commun.* **15**, 7770 (2024).
3. Chhowalla, M. et al. The chemistry of two-dimensional layered transition metal dichalcogenide nanosheets. *Nat. Chem.* **5**, 263–275 (2013).
4. Li, Z. N. et al. Lithiated metallic molybdenum disulfide nanosheets for high-performance lithium-sulfur batteries. *Nat. Energy* **8**, 84–93 (2023).
5. Chen, W. S. et al. Two-dimensional quantum-sheet films with sub-1.2 nm channels for ultrahigh-rate electrochemical capacitance. *Nat. Nanotechnol.* **17**, 153–158 (2022).
6. Acerce, M. et al. Metallic 1T phase MoS_2 nanosheets as supercapacitor electrode materials. *Nat. Nanotechnol.* **10**, 313–318 (2015).
7. Yu, Y. F. et al. High phase-purity 1T'-MoS_2- and 1T'-$MoSe_2$-layered crystals. *Nat. Chem.* **10**, 638–643 (2018).
8. Voiry, D. et al. Conducting MoS_2 nanosheets as catalysts for hydrogen evolution reaction. *Nano Lett.* **13**, 6222–6227 (2013).
9. Voiry, D. et al. Enhanced catalytic activity in strained chemically exfoliated WS_2 nanosheets for hydrogen evolution. *Nat. Mater.* **12**, 850–855 (2013).
10. Shi, Z. Y. et al. Phase-dependent growth of Pt on MoS_2 for highly efficient H_2 evolution. *Nature* **621**, 300–305 (2023).
11. Lai, Z. C. et al. Metastable 1T'-phase group VIB transition metal dichalcogenide crystals. *Nat. Mater.* **20**, 1113–1120 (2021).
12. Yang, R. J. et al. 2D transition metal dichalcogenides for photocatalysis. *Angew. Chem. Int. Ed.* **62**, e202218016 (2023).
13. Wang, Q. H. et al. Electronics and optoelectronics of two-dimensional transition metal dichalcogenides. *Nat. Nanotechnol.* **7**, 699–712 (2012).
14. Sebastian, A. et al. Benchmarking monolayer MoS_2 and WS_2 field-effect transistors. *Nat. Commun.* **12**, 693 (2021).
15. Radisavljevic, B. et al. Single-layer MoS_2 transistors. *Nat. Nanotechnol.* **6**, 147–150 (2011).
16. Yang, R. et al. Synthesis of atomically thin sheets by the intercalation-based exfoliation of layered materials. *Nat. Synth.* **2**, 101–118 (2023).
17. Pinilla, S. et al. Two-dimensional material inks. *Nat. Rev. Mater.* **7**, 717–735 (2022).
18. Coleman, J. N. et al. Two-dimensional nanosheets produced by liquid exfoliation of layered materials. *Science* **331**, 568–571 (2011).
19. Lin, Z. Y. et al. Solution-processable 2D semiconductors for high-performance large-area electronics. *Nature* **562**, 254–258 (2018).
20. Li, J. et al. Printable two-dimensional superconducting monolayers. *Nat. Mater.* **20**, 181–187 (2021).
21. Liu, N. et al. Large-area atomically thin MoS_2 nanosheets prepared using electrochemical exfoliation. *ACS Nano* **8**, 6902–6910 (2014).
22. Jeong, S. et al. Tandem intercalation strategy for single-layer nanosheets as an effective alternative to conventional exfoliation processes. *Nat. Commun.* **6**, 5763 (2015).
23. Eda, G. et al. Photoluminescence from chemically exfoliated MoS_2. *Nano Lett.* **11**, 5111–5116 (2011).
24. Yang, R. J. et al. High-yield production of mono- or few-layer transition metal dichalcogenide nanosheets by an electrochemical lithium ion intercalation-based exfoliation method. *Nat. Protoc.* **17**, 358–377 (2022).
25. Li, W. et al. Phase transitions in 2D materials. *Nat. Rev. Mater.* **6**, 829–846 (2021).
26. Song, X. Y. et al. Synthesis of an aqueous, air-stable, superconducting 1T'-WS_2 monolayer ink. *Sci. Adv.* **9**, eadd616 (2023).
27. Chou, S. S. et al. Understanding catalysis in a multiphasic two-dimensional transition metal dichalcogenide. *Nat. Commun.* **6**, 8311 (2015).
28. Wang, X. F. et al. Cryogenic electron microscopy for characterizing and diagnosing batteries. *Joule* **2**, 2225–2234 (2018).
29. Fan, X. B. et al. Controlled exfoliation of MoS_2 crystals into trilayer nanosheets. *J. Am. Chem. Soc.* **138**, 5143–5149 (2016).
30. Guo, P. et al. An all-printed, fast-response flexible humidity sensor based on Hexagonal-WO_3 nanowires for multifunctional applications. *Adv. Mater.* **35**, 2304420 (2023).
31. Anichini, C. et al. Chemical sensing with 2D materials. *Chem. Soc. Rev.* **47**, 4860–4908 (2018).
32. He, H. N. et al. Anion vacancies regulating endows MoSSe with fast and stable potassium ion storage. *ACS Nano* **13**, 11843–11852 (2019).
33. Lopez-Sanchez, O. et al. Ultrasensitive photodetectors based on monolayer MoS_2. *Nat. Nanotechnol.* **8**, 497–501 (2013).
34. Akinwande, D. et al. Two-dimensional flexible nanoelectronics. *Nat. Commun.* **5**, 5678 (2014).
35. Chang, H. Y. et al. High-performance, highly bendable MoS_2 transistors with high-K dielectrics for flexible low-power systems. *ACS Nano* **7**, 5446–5452 (2013).

36. Li, S. et al. Humidity-sensitive chemoelectric flexible sensors based on metal-air redox reaction for health management. *Nat. Commun.* **13**, 5416 (2022).
37. Feng, J. et al. Giant moisture responsiveness of VS_2 ultrathin nanosheets for novel touchless positioning interface. *Adv. Mater.* **24**, 1969–1974 (2012).
38. Zhao, J. et al. Highly sensitive MoS_2 humidity sensors array for noncontact sensation. *Adv. Mater.* **29**, 1702076 (2017).
39. Yu, X. G. et al. Skin-integrated wireless haptic interfaces for virtual and augmented reality. *Nature* **575**, 473–479 (2019).
40. Kresse, G. et al. Ab-Initio molecular-dynamics for open-shell transition-metals. *Phys. Rev. B* **48**, 13115–13118 (1993).
41. Perdew, J. P. et al. Generalized gradient approximation made simple. *Phys. Rev. Lett.* **77**, 3865–3868 (1996).
42. Grimme, S. et al. Effect of the damping function in dispersion corrected density functional theory. *J. Comput. Chem.* **32**, 1456–1465 (2011).

Acknowledgements

Z.Zeng thanks the Young Collaborative Research Grant (project no. C1003-23Y) and General Research Fund (GRF) (project no. CityU11308923) support from the Research Grants Council of the Hong Kong Special Administrative Region, China, the Basic Research Project from Shenzhen Science and Technology Innovation Committee in Shenzhen, China (project no. JCYJ20210324134012034), and the Applied Research Grant of City University of Hong Kong (project no. 9667247) and Chow Sang Sang Group Research Fund of City University of Hong Kong (project no. 9229123). Z.Zeng also thanks the funding supported by the Seed Collaborative Research Fund Scheme of State Key Laboratory of Marine Pollution, which receives regular research funding from Innovation and Technology Commission (ITC) of the Hong Kong SAR Government. However, any opinions, findings, conclusions or recommendations expressed in this publication do not reflect the views of the Hong Kong SAR Government or the ITC. X.Y. thanks the support from Research Grants Council of the Hong Kong Special Administrative Region (grant no. RFS2324-1S03) and Shenzhen Science and Technology Innovation Commission (grant no. SGDX20220530111401011). M.G. acknowledges the support from Guangdong Fundamental Research Association (project no. 2022B1515120013), National Natural Science Foundation of China (project no. 52273225) and Guangdong scientific programme (contract no. 2019QN01L057). L.G. thanks the funding support from National Natural Science Foundation of China (project nos. 52250402, 51991344 and 52025025).

Author contributions

Z. Zeng conceived and guided the project. L.M. designed and performed the synthesis and characterizations of all the materials. Z.G. and X.G.Y. performed the device fabrication and performance test. D.L., T.Y., H.H., J.Z., D.V. and Y.C. helped to analyse the results. Z. Zhang and M.D.G. carried out the cryo-electron microscopy test. M.S., X.L., Y.Z., B.H. and X.C.Z. conducted the DFT calculations. Q.Z. and L.G. performed the HAADF-STEM test of the samples. L.M., Z.G., R.Y., J.L., X.Y. and Z. Zeng drafted the paper. All authors checked the paper and agreed with its content.

Competing interests

The authors declare no conflicts of interest.

Additional information

Supplementary information The online version contains supplementary material available at https://doi.org/10.1038/s44160-024-00679-2.

Correspondence and requests for materials should be addressed to M. Danny Gu, Ju Li, Xinge Yu or Zhiyuan Zeng.

Peer review information *Nature Synthesis* thanks Qiaoliang Bao and the other, anonymous, reviewer(s) for their contribution to the peer review of this work. Primary Handling Editor: Alexandra Groves, in collaboration with the *Nature Synthesis* team.

Reprints and permissions information is available at www.nature.com/reprints.

Publisher's note Springer Nature remains neutral with regard to jurisdictional claims in published maps and institutional affiliations.

[1]Department of Materials Science and Engineering and State Key Laboratory of Marine Pollution, City University of Hong Kong, Hong Kong, P. R. China. [2]Department of Biomedical Engineering, City University of Hong Kong, Hong Kong, P. R. China. [3]Department of Applied Biology and Chemical Technology, The Hong Kong Polytechnic University, Hong Kong, P. R. China. [4]Beijing National Laboratory for Condensed Matter Physics, Institute of Physics, Chinese Academy of Sciences, Beijing, P. R. China. [5]Eastern Institute for Advanced Study, Eastern Institute of Technology, Ningbo, P. R. China. [6]Beijing National Center for Electron Microscopy and Laboratory of Advanced Materials, Department of Materials Science and Engineering, Tsinghua University, Beijing, P. R. China. [7]School of Materials Science and Engineering, Hunan Provincial Key Laboratory of Electronic Packaging and Advanced Functional Materials, Central South University, Changsha, P. R. China. [8]Institut Européen des Membranes, UMR 5635, ENSCM, CNRS, Université Montpellier, Montpellier, France. [9]Department of Applied Physics, The Hong Kong Polytechnic University, Hong Kong, P. R. China. [10]Department of Nuclear Science and Engineering and Department of Materials Science and Engineering, Massachusetts Institute of Technology, Cambridge, MA, USA. [11]Hong Kong Institute for Clean Energy, City University of Hong Kong, Hong Kong, P. R. China. [12]Shenzhen Research Institute, City University of Hong Kong, Shenzhen, P. R. China. [13]These authors contributed equally: Liang Mei, Zhan Gao, Ruijie Yang, Zhen Zhang. ✉e-mail: m.danny.gu@gmail.com; liju@mit.edu; xingeyu@cityu.edu.hk; zhiyzeng@cityu.edu.hk

nature synthesis

Supplementary information

https://doi.org/10.1038/s44160-024-00679-2

Phase-switchable preparation of solution-processable WS_2 mono- or bilayers

In the format provided by the authors and unedited

Contents

1. Supplementary Figures 1-47

Supplementary Fig. 1 Schematic illustration of 2H-, 1T- and 1T′-WS_2 structures

Supplementary Fig. 2 Characterizations of bulk WS_2 powder

Supplementary Fig. 3 Galvanostatic discharge curves for the lithium intercalation of WS_2 under different current densities

Supplementary Fig. 4 Raman spectra of WS_2 exfoliated under different discharge current densities

Supplementary Fig. 5 XPS W4*f* spectra of WS_2 exfoliated under different discharge current densities

Supplementary Fig. 6 Photographs of S-Li_xWS_2 and L-Li_xWS_2 after sonication in DI water

Supplementary Fig. 7 XRD pattern of the 2H- and 1T′-WS_2 thin films

Supplementary Fig. 8 STEM image of S vacancies in 2H-WS_2 NSs

Supplementary Fig. 9 STEM image of S vacancies in 1T′-WS_2 NSs

Supplementary Fig. 10 EPR spectrums of exfoliated 2H- and 1T′-WS_2 NSs

Supplementary Fig. 11 TEM images of exfoliated 2H- and 1T′-WS_2 NSs

Supplementary Fig. 12 SEM images of exfoliated 2H- and 1T′-WS_2 NSs

Supplementary Fig. 13 AFM images and thickness distribution of exfoliated 2H- and 1T′-WS_2 NSs

Supplementary Fig. 14 Discharge curves of Li^+ intercalation of WSe_2 under different current densities

Supplementary Fig. 15 UV-vis spectra of exfoliated WSe_2 NSs solution using different discharge current densities

Supplementary Fig. 16 XPS W4*f* spectra of exfoliated WSe_2 NSs solution using different discharge current densities

Supplementary Fig. 17 Discharge curves of Li^+ intercalation of MoS_2 under different current densities

Supplementary Fig. 18 XPS Mo3*d* and Raman spectra of exfoliated MoS_2 using

different discharging current densities
Supplementary Fig. 19 EELS spectra of S-Li_xWS_2 electrode
Supplementary Fig. 20 XRD pattern of bulk WS_2, S-Li_xWS_2 and L-Li_xWS_2
Supplementary Fig. 21 EELS spectra of L-Li_xWS_2 electrode
Supplementary Fig. 22 Raman and XPS W4*f* spectra of S-Li_xWS_2 and L-Li_xWS_2
Supplementary Fig. 23 XPS S2*p* spectra of bulk WS_2, S-Li_xWS_2, L-Li_xWS_2, and the corresponding exfoliated 2H- and 1T′-WS_2 NSs
Supplementary Fig. 24 XPS Li 1*s* spectra of S-Li_xWS_2, L-Li_xWS_2 and Li foil
Supplementary Fig. 25 Phase of 2H and 1T′ formation energy of different intercalated Li content in Li_xWS_2
Supplementary Fig. 26 Atomic models of optimized different Li-intercalated 2H-Li_xWS_2 structures
Supplementary Fig. 27 Atomic models of optimized different Li-intercalated 1T′-Li_xWS_2 structures
Supplementary Fig. 28 Galvanostatic discharge/charge curves of S-Li_xWS_2 and L-Li_xWS_2
Supplementary Fig. 29 EPR spectrums of bulk WS_2, intercalated WS_2 and deintercalated WS_2
Supplementary Fig. 30 Theoretical simulations of the formation of the SEI under large and small discharge current densities
Supplementary Fig. 31 SEM image of 2H-WS_2 based device
Supplementary Fig. 32 Schematic diagram of a home-made setup for humidity sensing performance test
Supplementary Fig. 33 Resistance of 2H-WS_2 based humid sensor under different RH
Supplementary Fig. 34 schematic of the humidity sensing mechanism under different RH
Supplementary Fig. 35 The calculated energy for generating different S vacancies in 1T′-WS_2
Supplementary Fig. 36 Adsorption energy of H_2O molecule on 2H- and 1T′-WS_2

Supplementary Fig. 37 Projected density of states for 2H- and 1T′-WS_2 with S vacancies
Supplementary Fig. 38 The protection performance of different masks via using 2H-WS_2 based humidity sensor
Supplementary Fig. 39 Photograph of humidity sensor set-up for voice recognition
Supplementary Fig. 40 Response current of 2H-WS_2 while speaking different words
Supplementary Fig. 41 Response current of 2H-WS_2 while speaking different words
Supplementary Fig. 42 Response current of 2H-WS_2 while speaking different words
Supplementary Fig. 43 Response current of 2H-WS_2 while speaking different words
Supplementary Fig. 44 The long-term stability of 2H-WS_2 based humidity sensor performance
Supplementary Fig. 45 The flexibility of 2H-WS_2 based humidity sensor device
Supplementary Fig. 46 Original current distribution of 5×5 humid sensor array in none-contact finger localization experiments
Supplementary Fig. 47 2H-WS_2 based humidity sensor array used for monitoring baby diaper wetness

2. Supplementary Tables 1-2

Supplementary Table 1 DFT calculated phase formation energy and corresponding interlayer spacing for lithium intercalation of WS_2
Supplementary Table 2 Comparison of humidity sensing performance of the developed 2H- and 1T′-WS_2 NSs with other reported humidity sensors.

3. Supplementary References

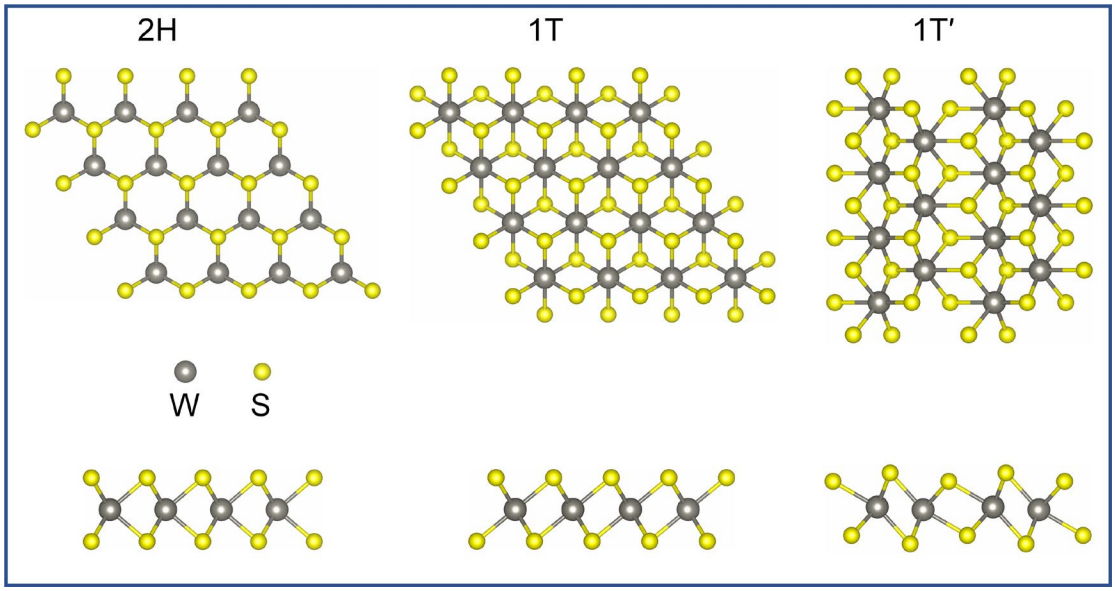

Supplementary Fig. 1 | Atomic models of different phases of WS_2. Schematic illustration of 2H-, 1T- and 1T′-WS_2 structures. Upside: top view of the structures; downside: side view of the structures.

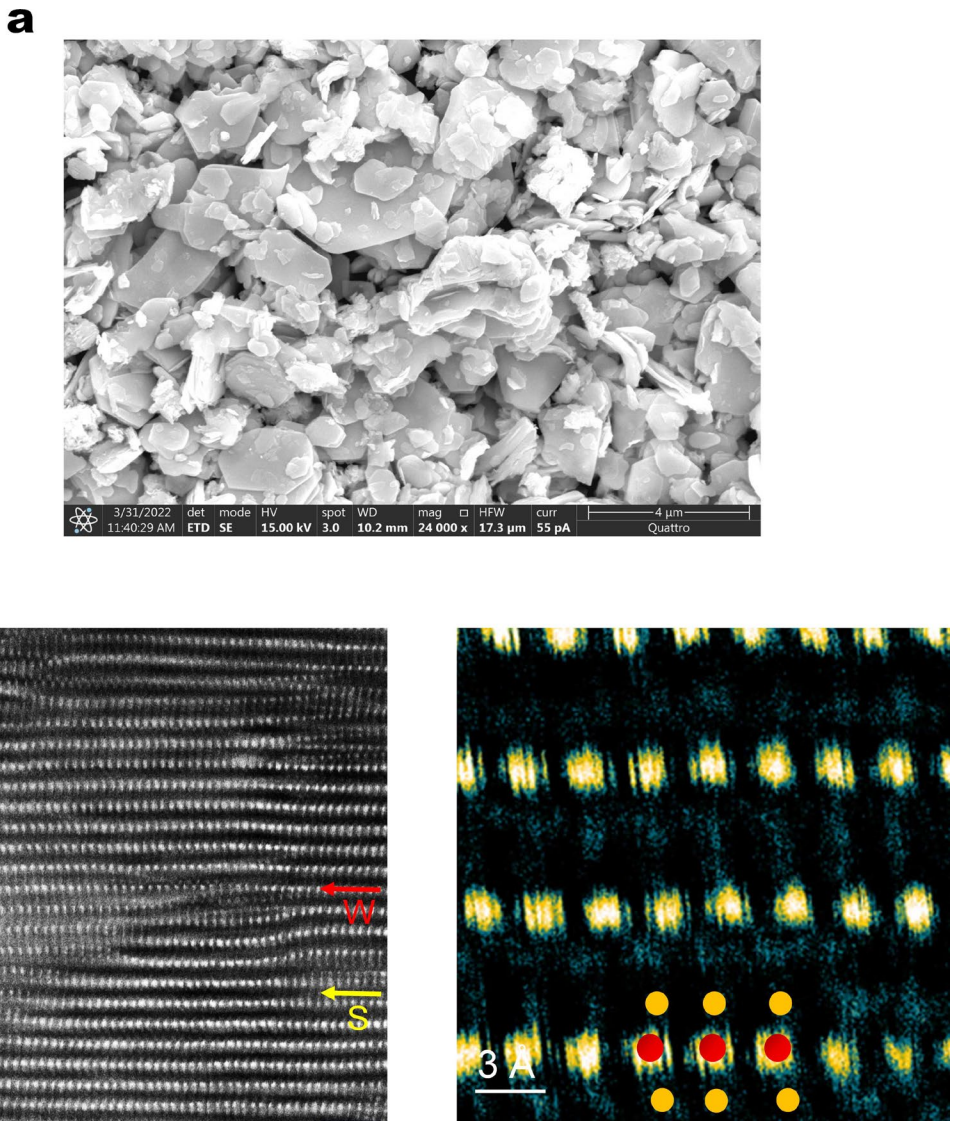

Supplementary Fig. 2 | Characterizations of bulk WS_2 powder. a, SEM images of WS_2 powder. The layered structures of bulk WS_2 are clearly observed, and the size are in the range of 2-5µm. **b,** Cross-sectional HAADF-STEM images of bulk WS_2 with different magnifications. The 2H structure is clearly observed from the magnified image of bulk WS_2. Red and yellow circles denote the W and S atoms.

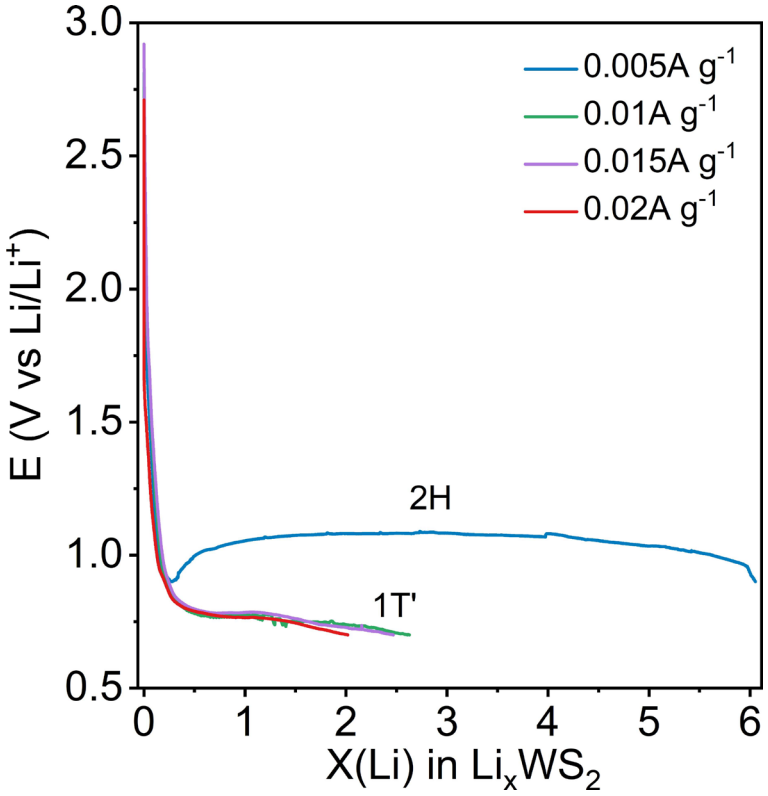

Supplementary Fig. 3 | Electrochemical Li^+ intercalation of WS_2. Galvanostatic discharge curves for the lithium intercalation of WS_2 under different discharge current densities.

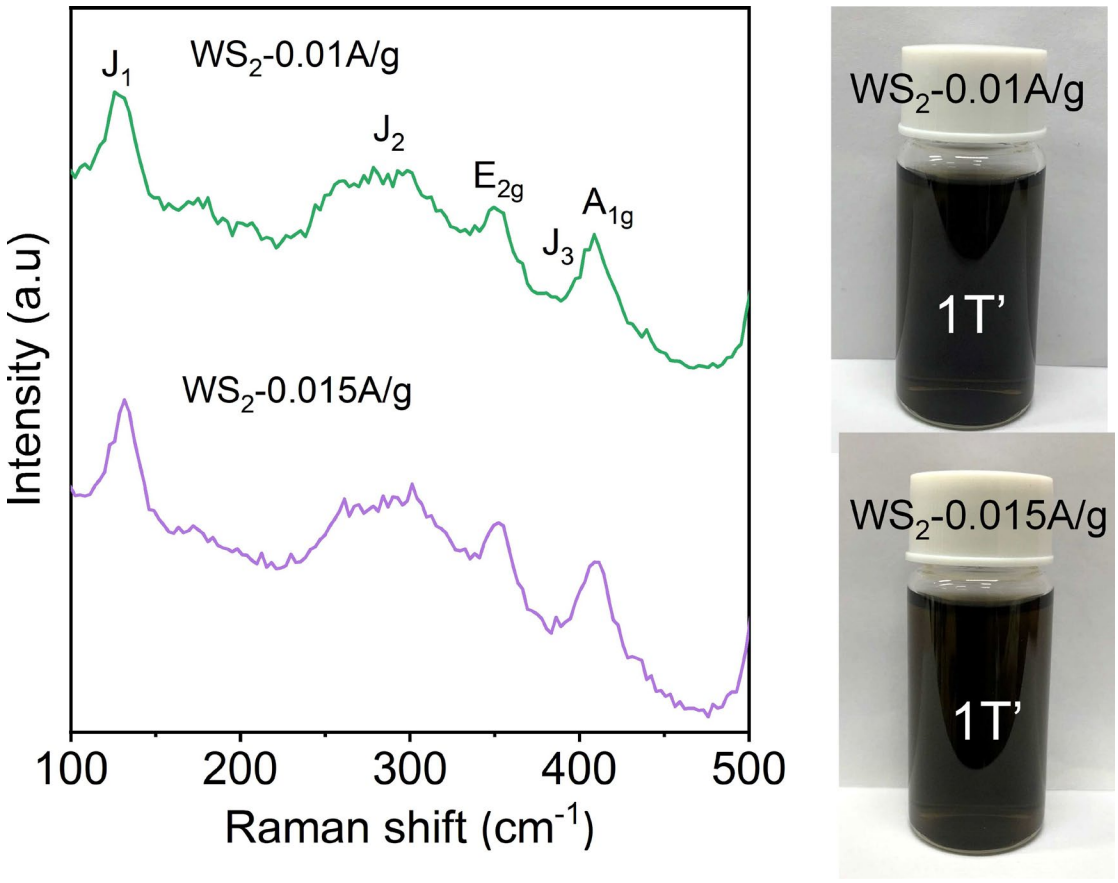

Supplementary Fig. 4 | Characterization of exfoliated WS_2. Raman spectra of WS_2 exfoliated under discharge current densities of 0.01 A g^{-1} and 0.015 A g^{-1}, right-side show the corresponding photographs of exfoliated solution.

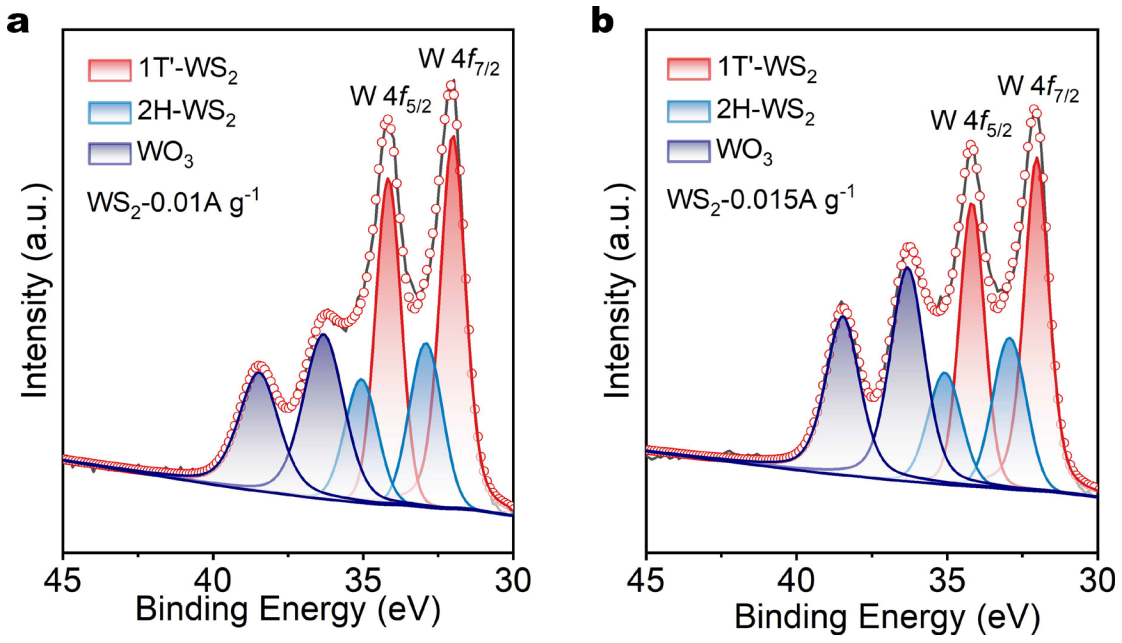

Supplementary Fig. 5 | Characterization of exfoliated WS_2. XPS W4*f* spectra of WS_2 exfoliated under discharge current densities of **a** 0.01 A g^{-1} and **b** 0.015 A g^{-1}.

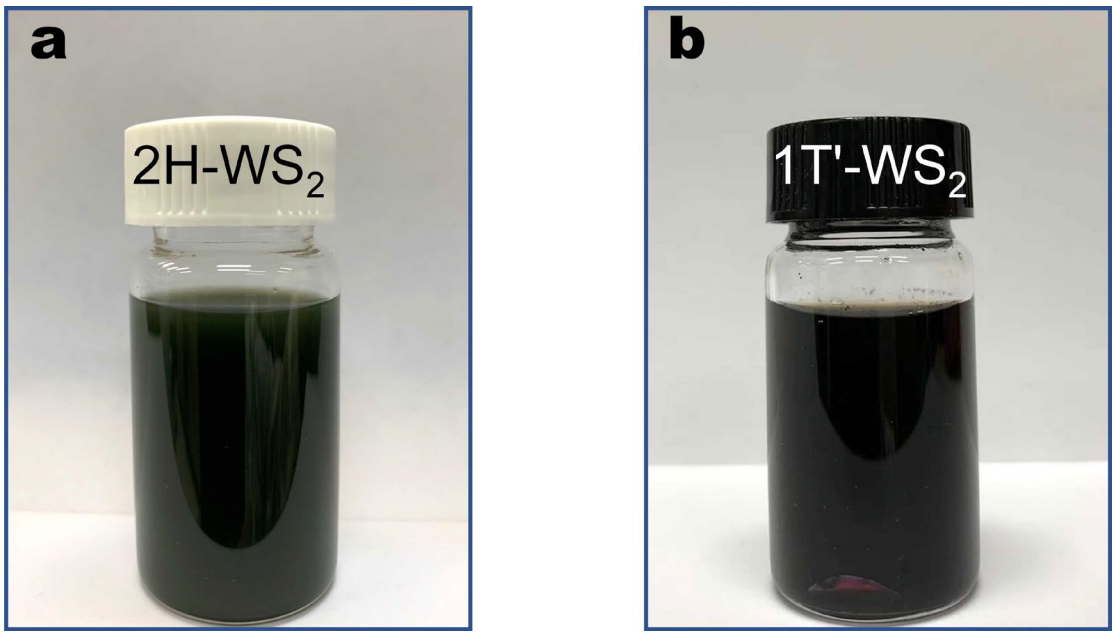

Supplementary Fig. 6 | Photographs of exfoliated 2H- and 1T′-WS_2 NSs solution before washing steps. The S-Li_xWS_2 and L-Li_xWS_2 electrodes were well exfoliated in ethanol and DI water, respectively. After 5-10 min, two opaque suspensions exhibited dark green and dark black obtained. S-Li_xWS_2, L-Li_xWS_2 denote as Li^+ intercalation of WS_2 by small and large discharge current densities, respectively.

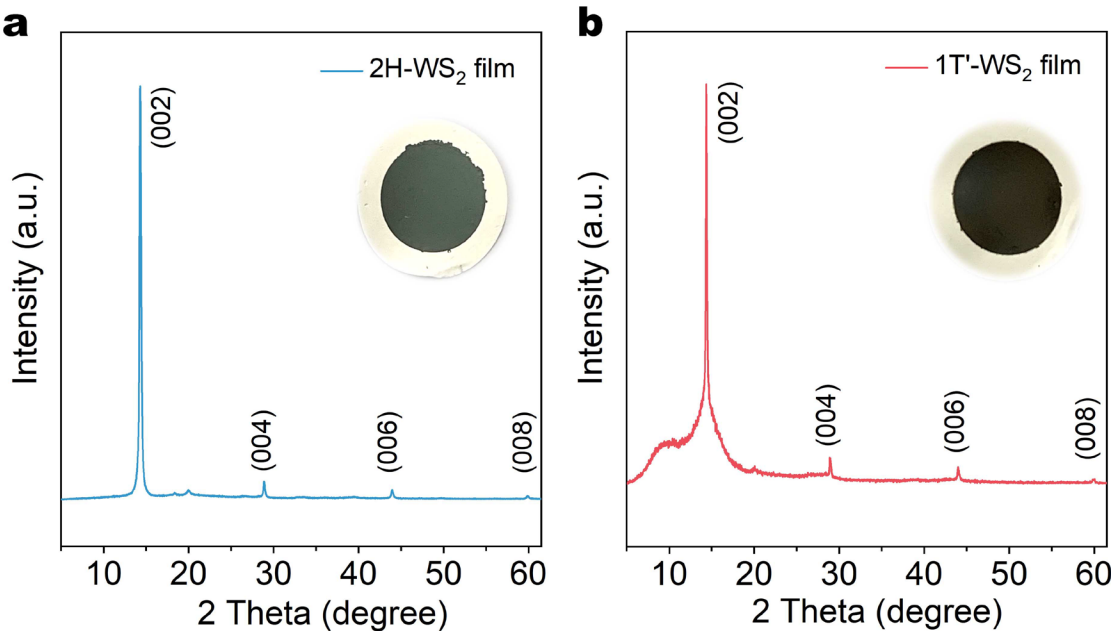

Supplementary Fig. 7 | a-b, XRD patterns of the 2H- and 1T′-WS_2 thin films. These thin films were prepared via vacuum filtration of the corresponding exfoliated WS_2 NSs onto polyvinylidene difluoride (PVDF) substrate, demonstrating well-controlled assembly along the (001) direction. Insets show the photographs of the corresponding films. The 2H-WS_2 film exhibits a green color, whereas 1T′-WS_2 film appears black.

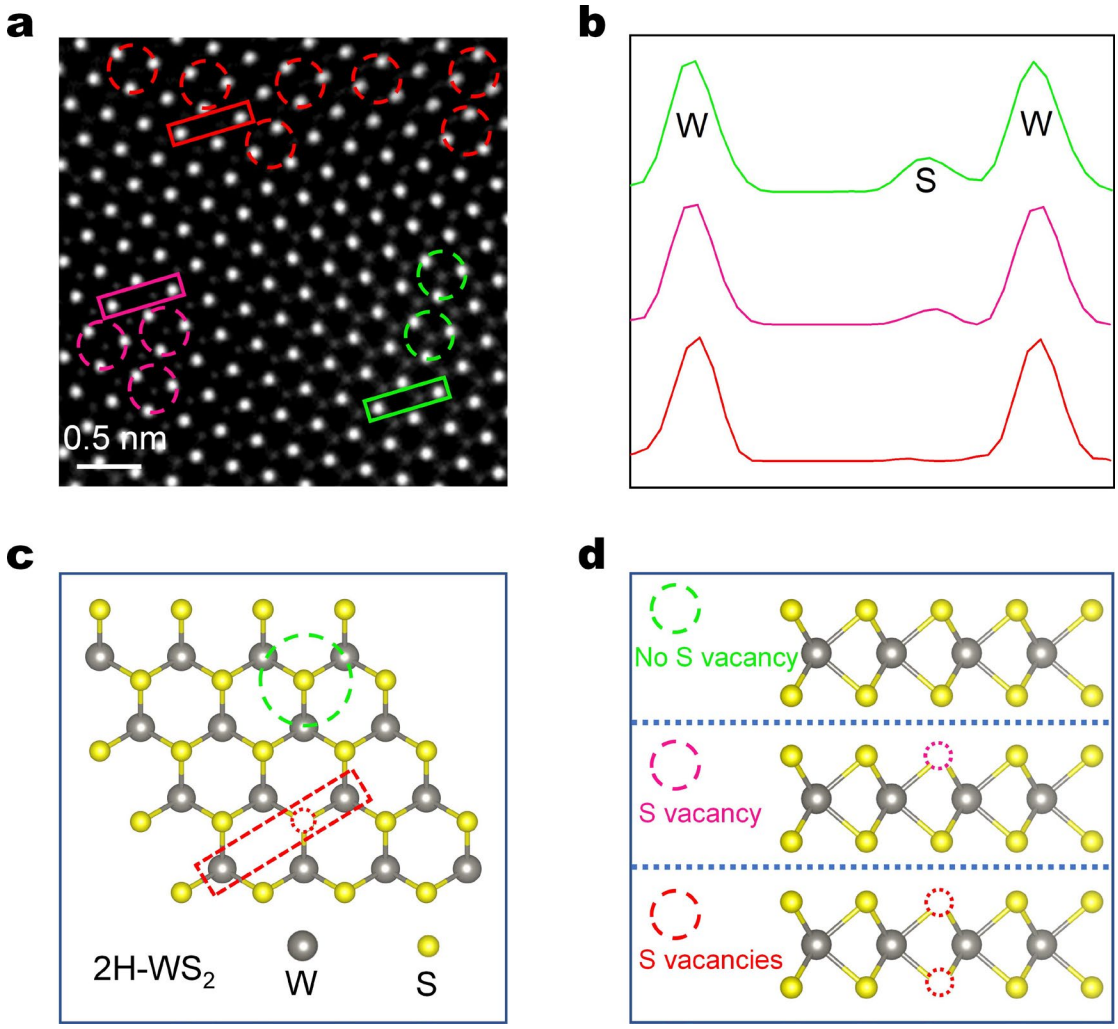

Supplementary Fig. 8 | Structure characterization of exfoliated 2H-WS_2 NSs. a, Atomic-resolution annular dark field (ADF) images showing different types of S vacancies in 2H-WS_2. **b**, Line intensity profile scans along the red, green and magenta boxed atoms in **a**. **c-d**, Schematic of S vacancies in the atomic model of 2H-WS_2 from the top and main view. HAADF-STEM results confirm the existence of S vacancies in exfoliated 2H-WS_2 NSs, which are consistent with electron paramagnetic resonance (EPR) results (**Supplementary Fig. 10**).

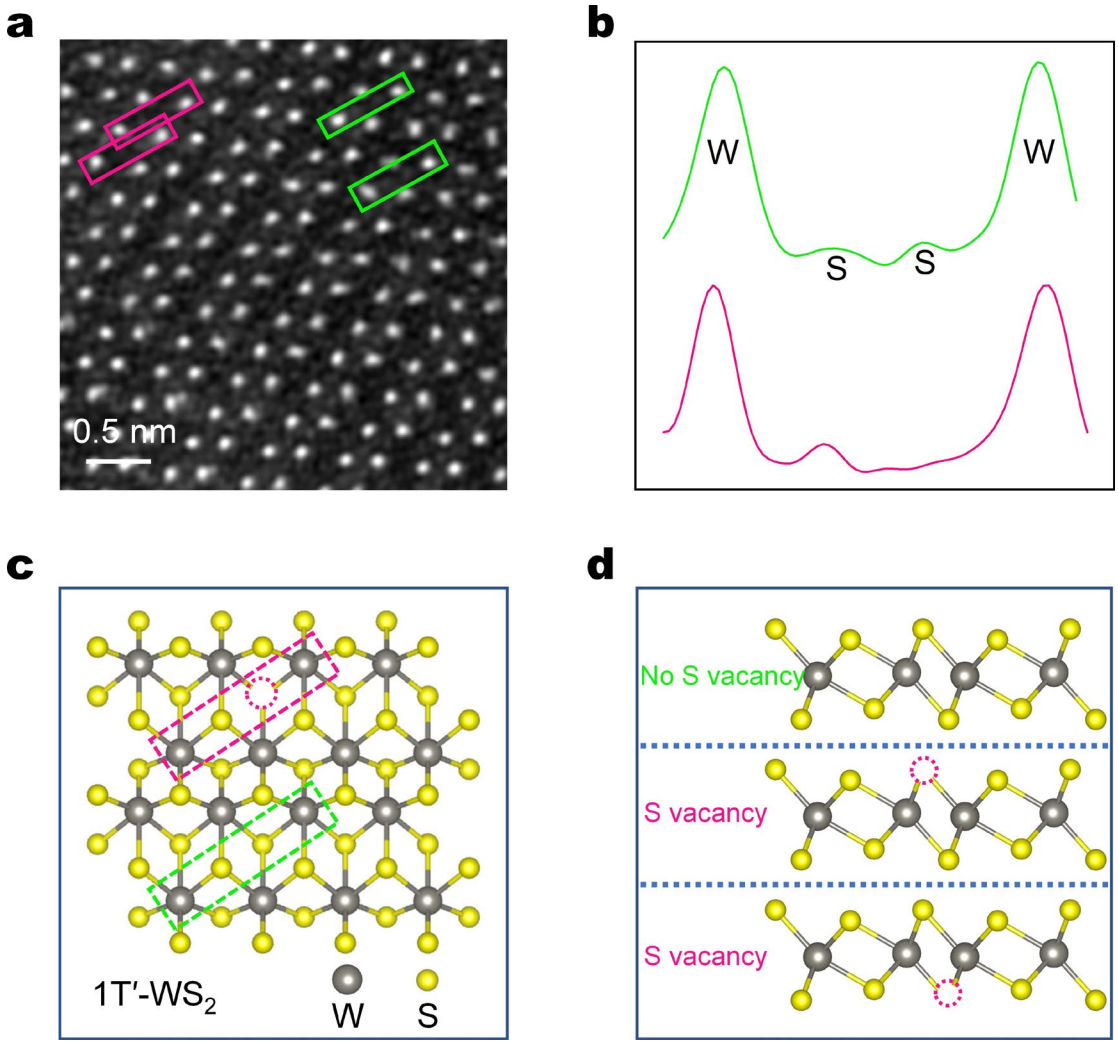

Supplementary Fig. 9 | Structure characterization of exfoliated 1T′-WS_2 NSs. a, Atomic-resolution annular dark field (ADF) images showing different types of S vacancies in 1T′-WS_2. **b**, Line intensity profile scans along the green and magenta boxed atoms in **a**. **c-d**, Schematic of S vacancies in the atomic model of 1T′-WS_2 from the top and main view. HAADF-STEM results confirm the existence of S vacancies in exfoliated 1T′-WS_2 NSs, which agree well with electron paramagnetic resonance (EPR) results (**Supplementary Fig. 10**).

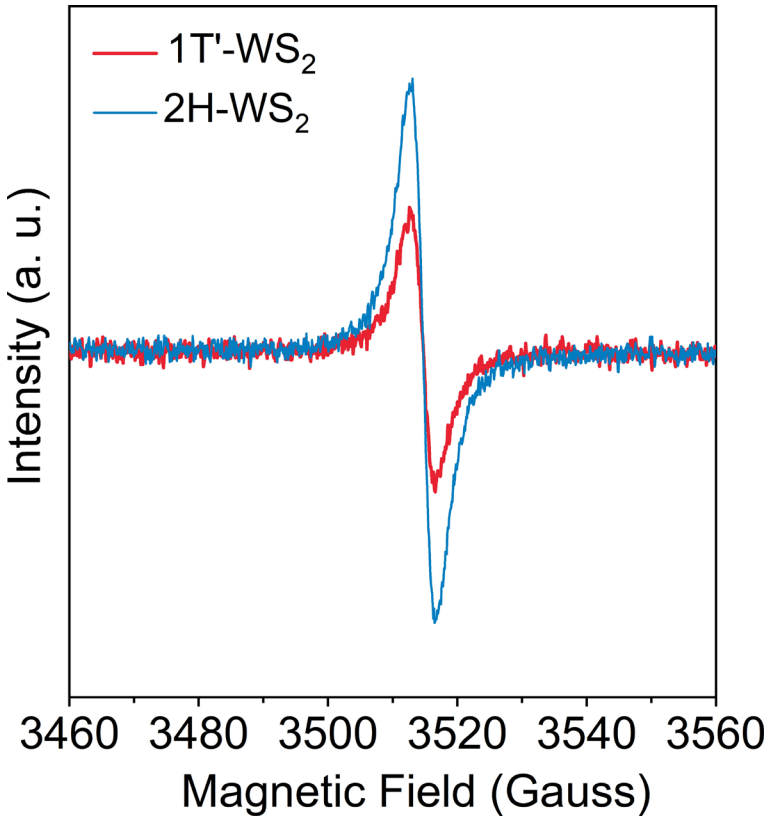

Supplementary Fig. 10 | Structure characterization of 2H- and 1T′-WS_2 NSs. EPR spectrums of exfoliated 2H- and 1T′-WS_2 NSs, revealing that there exist more S vacancies in 2H-WS_2 than that in 1T′-WS_2 NSs.

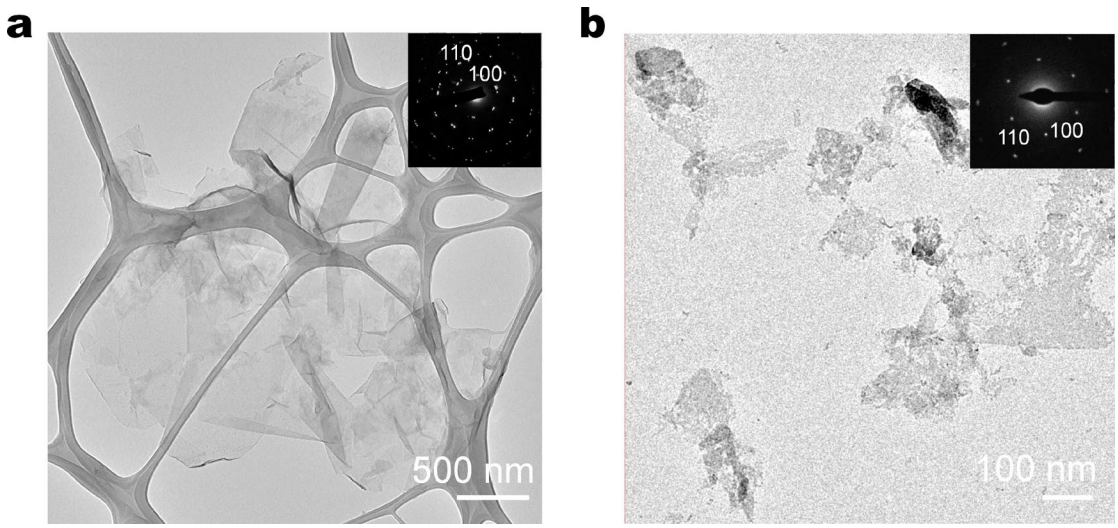

Supplementary Fig. 11 | Morphology characterization of exfoliated 2H- and 1T′-WS_2. TEM images of **a** 2H- and **b** 1T′-WS_2. Both the 2H- and 1T′-WS_2 exhibit the NSs morphology in TEM images with lateral sizes ranging from 300-600 nm and 100-200 nm, respectively. The variance in size for 2H- and 1T′-WS_2 NSs can be ascribed to a higher quantity of intercalated lithium within the interlayer of WS_2 for L-Li_xWS_2 in comparison to S-Li_xWS_2. This disparity leads to a reduction in the NSs size after the exfoliation process. S-Li_xWS_2, L-Li_xWS_2 denote as Li^+ intercalation of WS_2 by small and large discharge current densities, respectively.

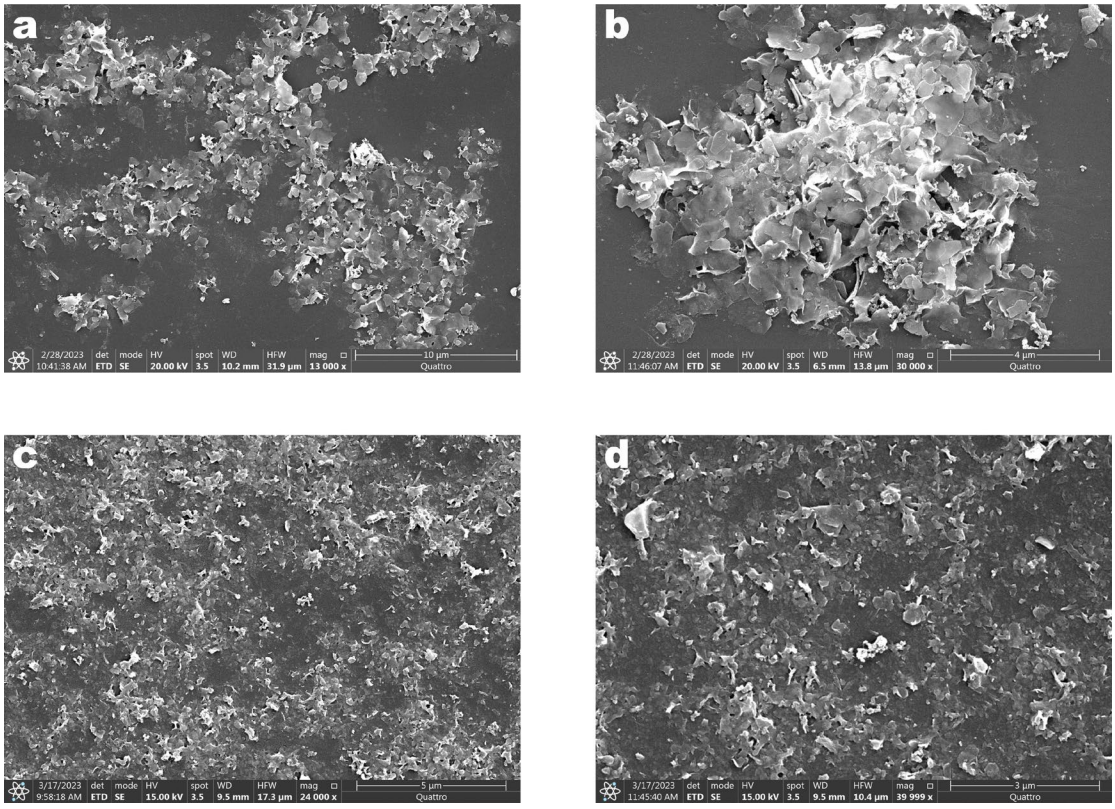

Supplementary Fig. 12 | Morphology characterization of exfoliated 2H- and 1T′-WS_2. SEM images of 2H- (**a-b**) and 1T′-WS_2 (**c-d**) NSs with different magnification.

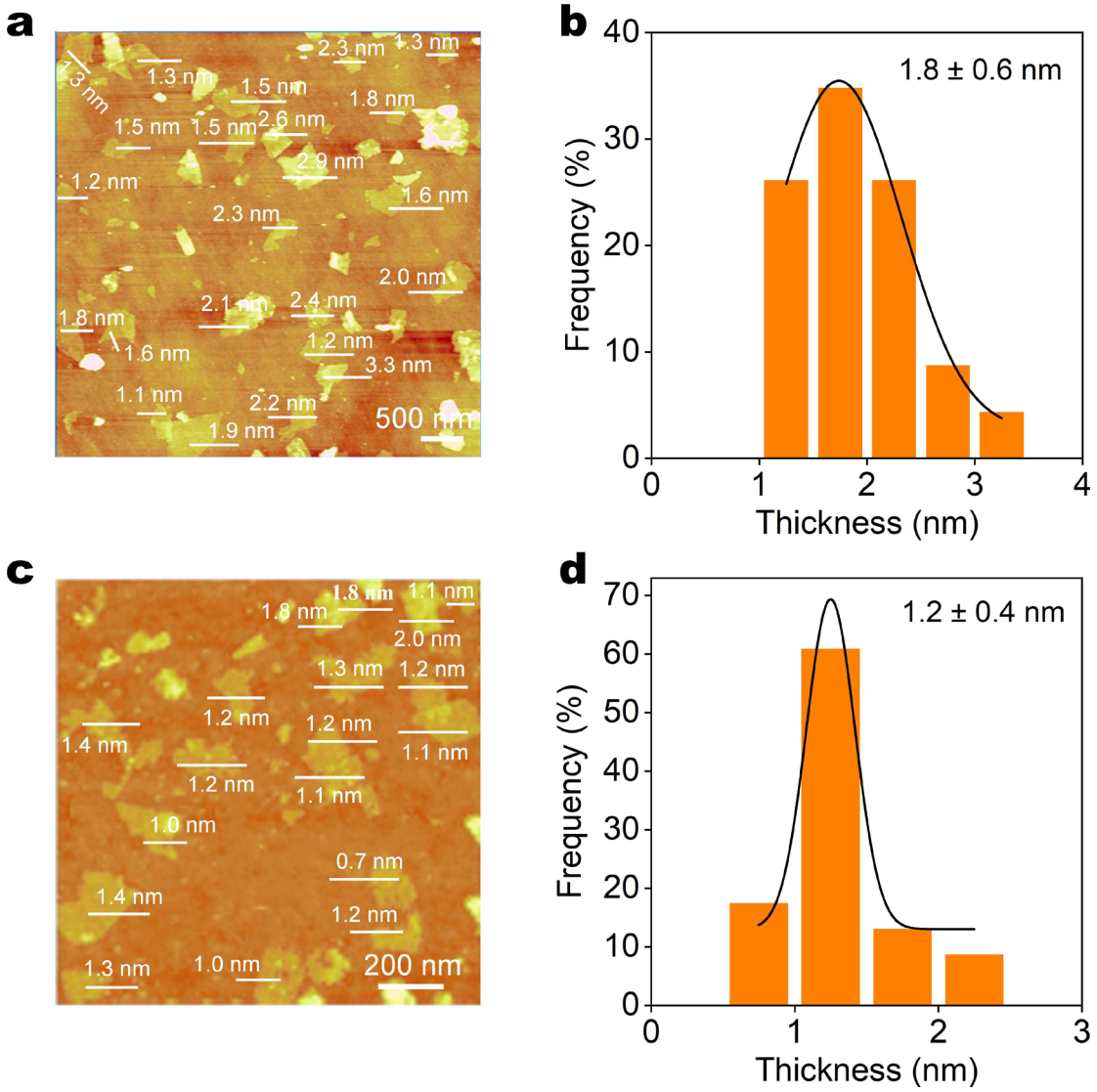

Supplementary Fig. 13 | Characterization of 2H- and 1T′-WS_2 NSs. AFM images of the exfoliated 2H- (**a**) and 1T′-WS_2 NSs (**c**). The corresponding thickness distribution histogram are shown in (**b**) and (**d**). The mean thickness of the 2H-WS_2 NSs is determined to be 1.8 nm with a standard deviation of 0.6 nm. In contrast, the corresponding values for the 1T′-WS_2 NSs are 1.2 nm and 0.4 nm, respectively. These analyses conclusively demonstrate the fabrication of bilayer 2H-WS_2 and monolayer 1T′-WS_2 NSs.

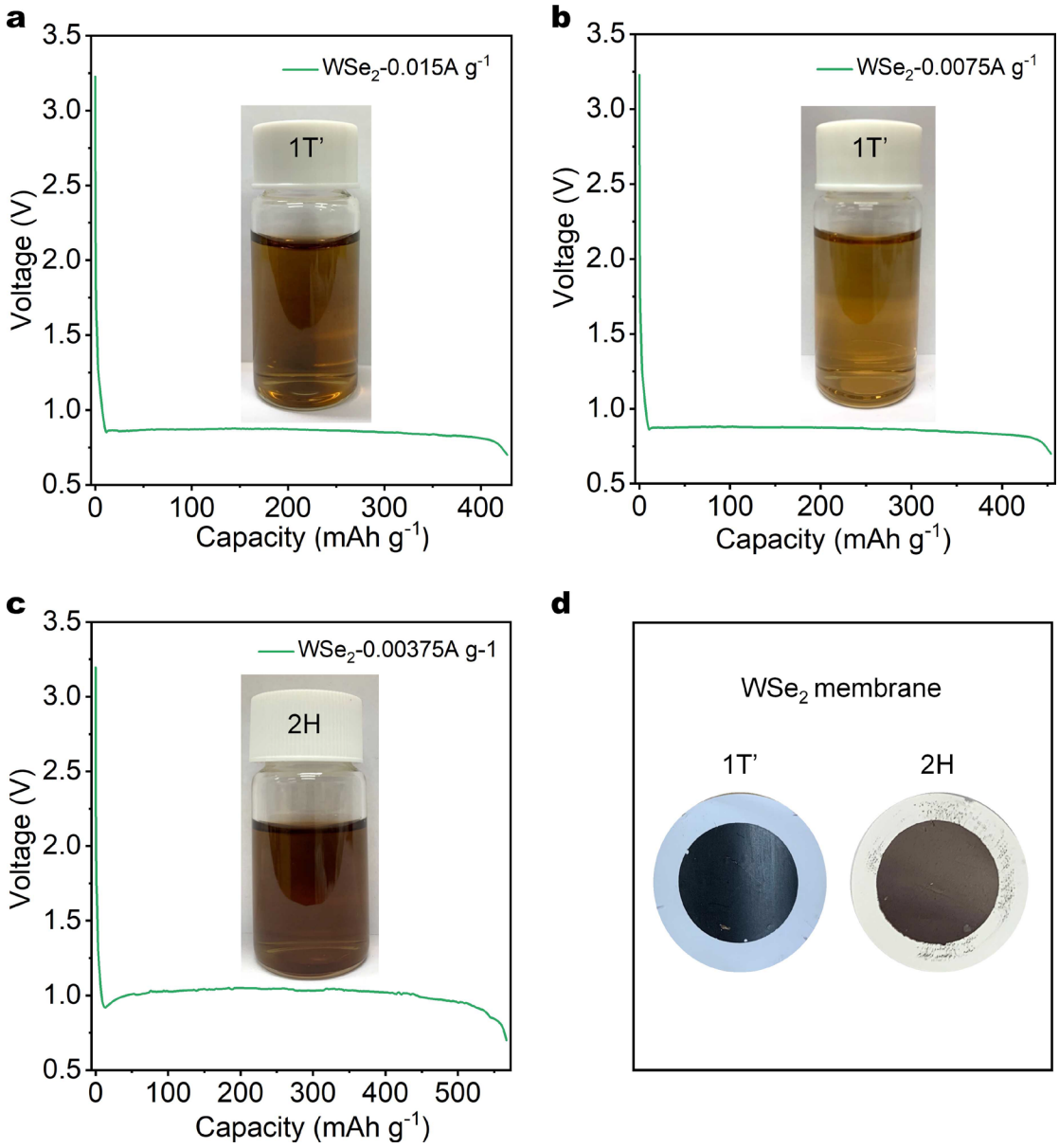

Supplementary Fig. 14 | Electrochemical Li^+ intercalation and exfoliation of WSe_2. **a-c,** Discharge curves of Li^+ intercalation of WSe_2 under different discharge current densities, inset show the photographs of corresponding exfoliated nanosheets solution. **d**, The photographs of 1T′- and 2H WSe_2 membrane prepared via vacuum filtration of the corresponding exfoliated nanosheets solution onto porous substrate.

We can also achieve phase-switchable preparation of WSe_2 by adjusting the discharging current density. As shown in **Supplementary Fig. 14a-c**, decreasing the discharge current density from 0.015 A g^{-1} to 0.00375 A g^{-1} results in a discharge curve similar to that observed in WS_2. Following exfoliation, the dispersions of WSe_2 NSs exhibits a brown color (**Supplementary Fig. 14c**), indicating partial absorption in the visible

range. This is confirmed by the ultraviolet-visible absorption spectrum (**Supplementary Fig. 15**), which verifies the formation of semiconducting 2H phase WSe_2 NSs under a low discharging current density (0.00375 A g^{-1}). In contrast, the dispersions of WSe_2 NSs exfoliated at high discharge current densities (0.0075 A g^{-1} and 0.015 A g^{-1}) appears light black (**Supplementary Fig. 14a**, **b**, **d**), suggesting complete and featureless absorption in the visible range (**Supplementary Fig. 15**). This change indicates a phase transition, resulting in the formation of metallic 1T/1T′ phase WSe_2 NSs under high discharge current densities.

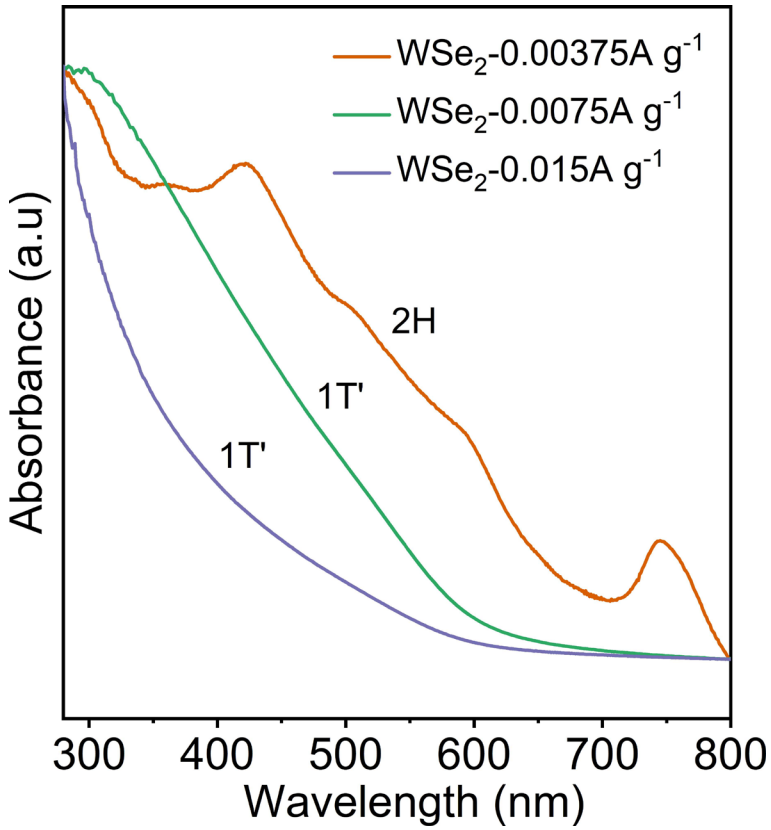

Supplementary Fig. 15 | Characterization of exfoliated WSe_2. Visible-near infrared absorption spectra of exfoliated WSe_2 NSs solution that fabricated under different discharge current densities.

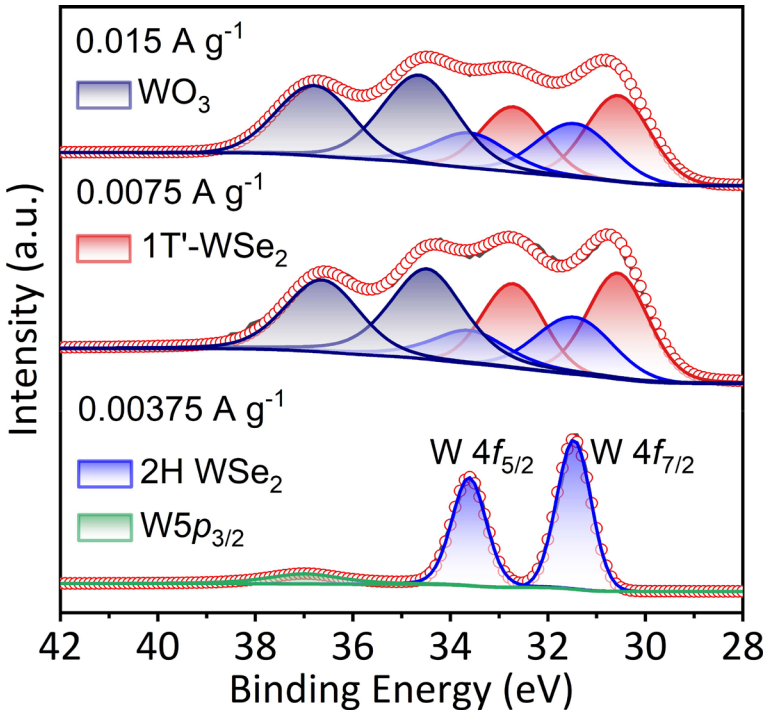

Supplementary Fig. 16 | Characterization of exfoliated WSe_2. XPS W 4*f* spectra of exfoliated WSe_2 prepared by Li^+ intercalation under different discharge current densities.

Additionally, XPS spectra confirm that a small discharge current density (0.00375 A g^{-1}) yields pure 2H phase WSe_2 (**Supplementary Fig. 16**), whereas large discharge current densities (0.0075 A g^{-1}, 0.015 A g^{-1}) induce a phase transition from 2H to 1T′, leading to predominantly 1T′ phase WSe_2. Thus, this method enables phase-switchable preparation of WSe_2 NSs.

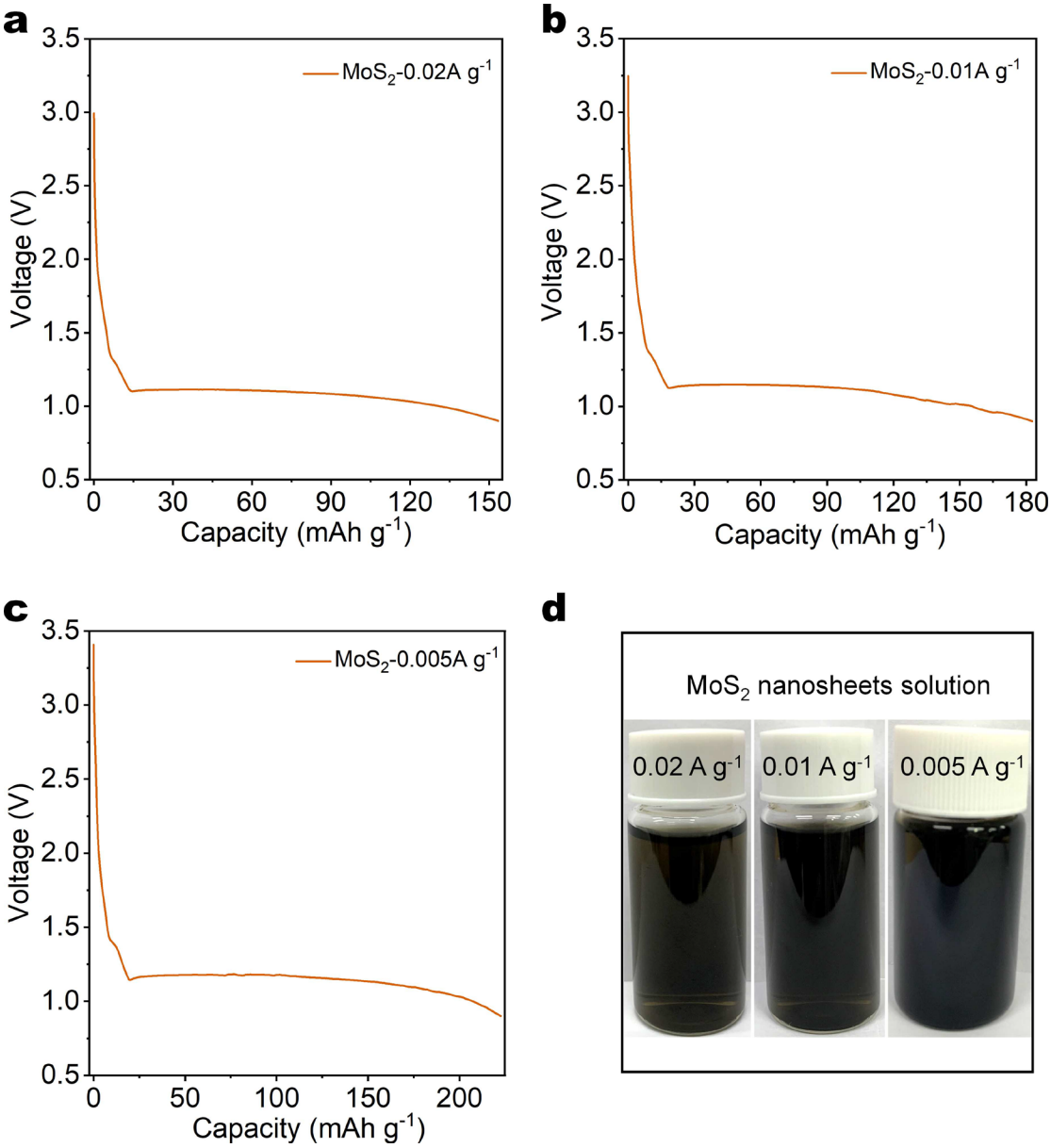

Supplementary Fig. 17 | Electrochemical Li^+ intercalation and exfoliation of MoS_2. **a-c,** Discharge curves of Li^+ intercalation of MoS_2 under different discharge current densities. **d**, The corresponding photographs of exfoliated MoS_2 NSs solution.

As shown in **Supplementary Fig. 17a-c**, applying different discharge current densities for Li^+ intercalation of MoS_2 slightly increased the intercalated Li^+ amounts upon decreasing the current density. After exfoliation, all the MoS_2 NSs dispersions showed black color (**Supplementary Fig. 17d**), indicating the formation of metallic 1T′ phase MoS_2 NSs under these discharge current densities.[1]

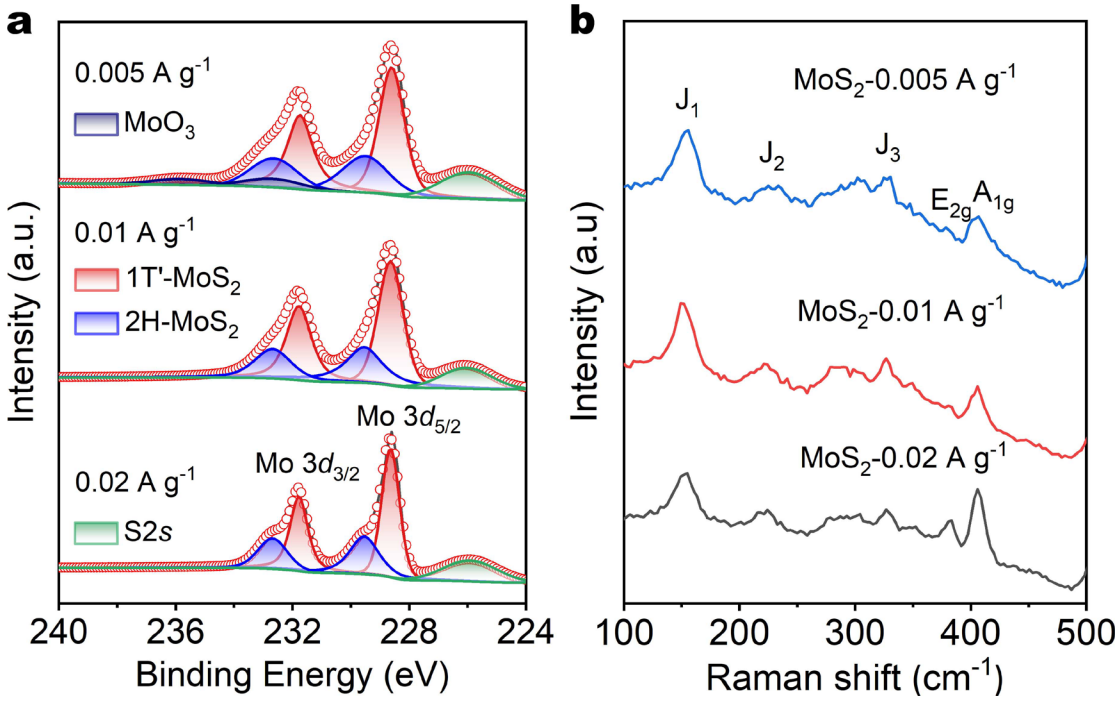

Supplementary Fig. 18 | Characterization of exfoliated MoS_2. a, XPS Mo 3*d* and **b**, Raman spectra of exfoliated MoS_2 prepared by Li^+ intercalation under different discharge current densities.

Furthermore, both XPS (**Supplementary Fig. 18a**) and Raman spectra (**Supplementary Fig. 18b**) confirmed that these exfoliated MoS_2 samples, prepared under different discharge current densities, all exhibit a 1T′ phase-dominated structure. No pure 2H MoS_2 was prepared by tuning the discharge current densities. Therefore, this phase-switchable method is not suitable for MoS_2.

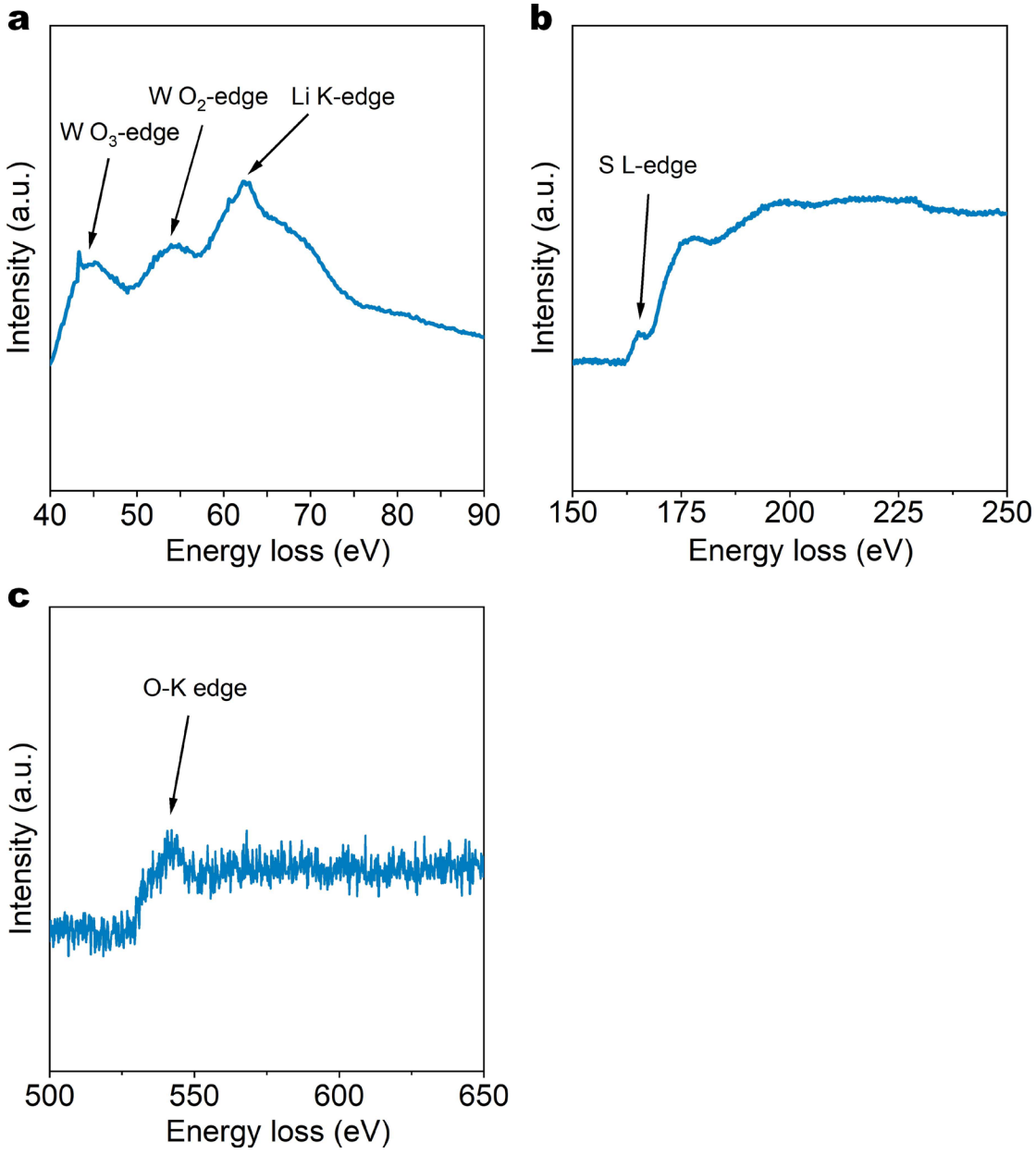

Supplementary Fig. 19 | EELS spectra of S-Li_xWS_2 electrode. a, Li K-edge, W O_2-edge and W O_3-edge. **b**, S L-edge. **c**, O K-edge. S-Li_xWS_2 denotes as Li^+ intercalation of WS_2 by a small discharge current density.

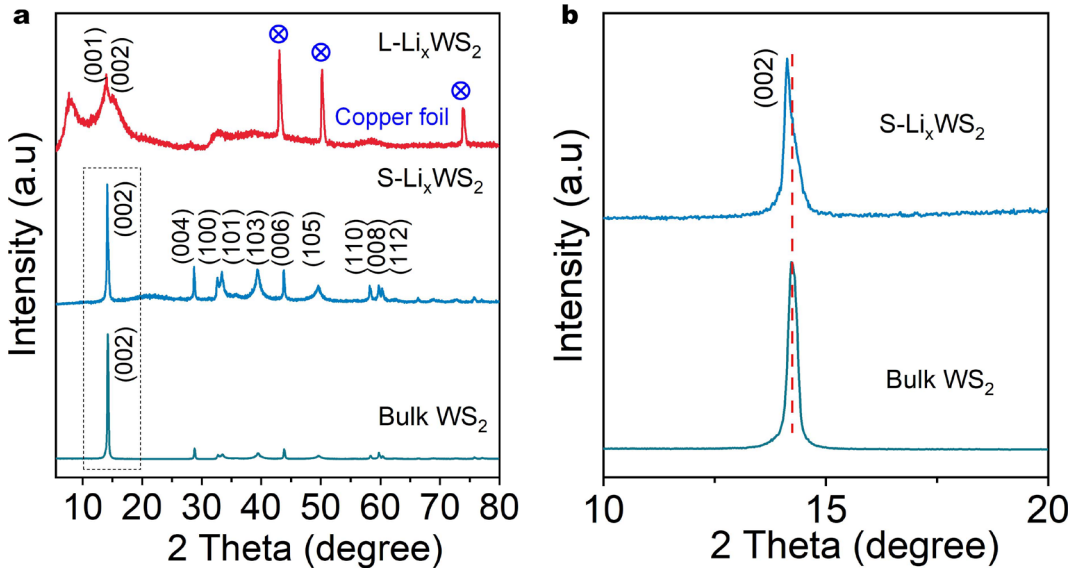

Supplementary Fig. 20 | Characterizations of S-Li$_x$WS$_2$ and L-Li$_x$WS$_2$. a, XRD patterns of bulk WS_2, S-Li$_x$WS$_2$ and L-Li$_x$WS$_2$. **b**, Magnified XRD patterns of the (002) peak of bulk WS_2 (bottom) and S-Li$_x$WS$_2$ (top) from the area within the dotted line in **a**. S-Li$_x$WS$_2$, L-Li$_x$WS$_2$ denote as Li^+ intercalation of WS_2 by small and large discharge current densities, respectively.

X-ray diffraction (XRD) analysis reveals an expansion of the interlayer galleries after lithiation. The (002) peak shifts from 14.30° in bulk WS_2 to 14.13° in S-Li$_x$WS$_2$ and 13.96° in L-Li$_x$WS$_2$, indicating an increase in interlayer spacing from 6.19 to 6.26 Å and 6.34 Å, respectively. Additionally, the peak at 14.17° in L-Li$_x$WS$_2$ can be attributed to the (001) plane of Li-intercalated 1T′-WS_2,[2,3] providing further confirmation of the phase transition occurring in this lithium intercalation pathway. Notably, the intensity of the characteristic peaks of hexagonal 2H-WS_2 decreases significantly in L-Li$_x$WS$_2$ due to the loss of long-range order resulting from the formation of both 2H- and 1T′ phases.[4] Furthermore, the peak at 7.87° in L-Li$_x$WS$_2$ is formed by the hydration,[4] which may contribute to the oxidation of L-Li$_x$WS$_2$, as analyzed in the XPS spectrum (**Supplementary Fig. 22b**). In contrast, all the peaks in S-Li$_x$WS$_2$ can be indexed to 2H-WS_2 (PDF-08-0237), indicating that no phase transition occurs during lithium intercalation using small discharge current. These results are highly consistent with Raman (**Supplementary Fig. 22a**), XPS (**Supplementary Fig. 22b**, **Supplementary Fig. 23**) and HAADF-STEM (**Fig. 2d, j**) results.

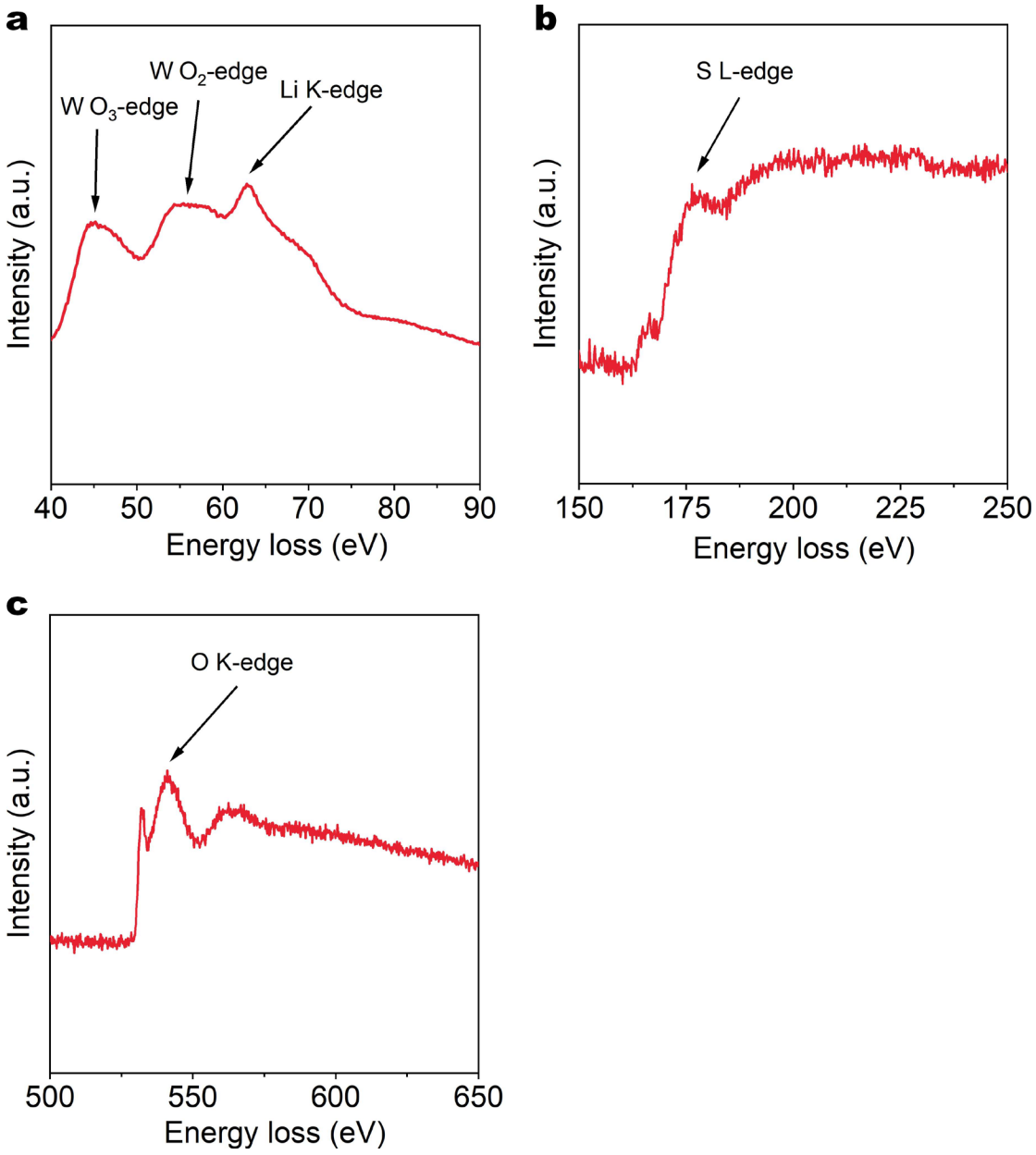

229

230 **Supplementary Fig. 21 | EELS spectra of L-Li$_x$WS$_2$ electrode. a**, Li K-edge, W O_2-

231 edge and W O_3-edge. **b**, S L-edge. **c**, O K-edge. L-Li$_x$WS$_2$ denotes as Li^+ intercalation

232 of WS_2 by a large discharge current density.

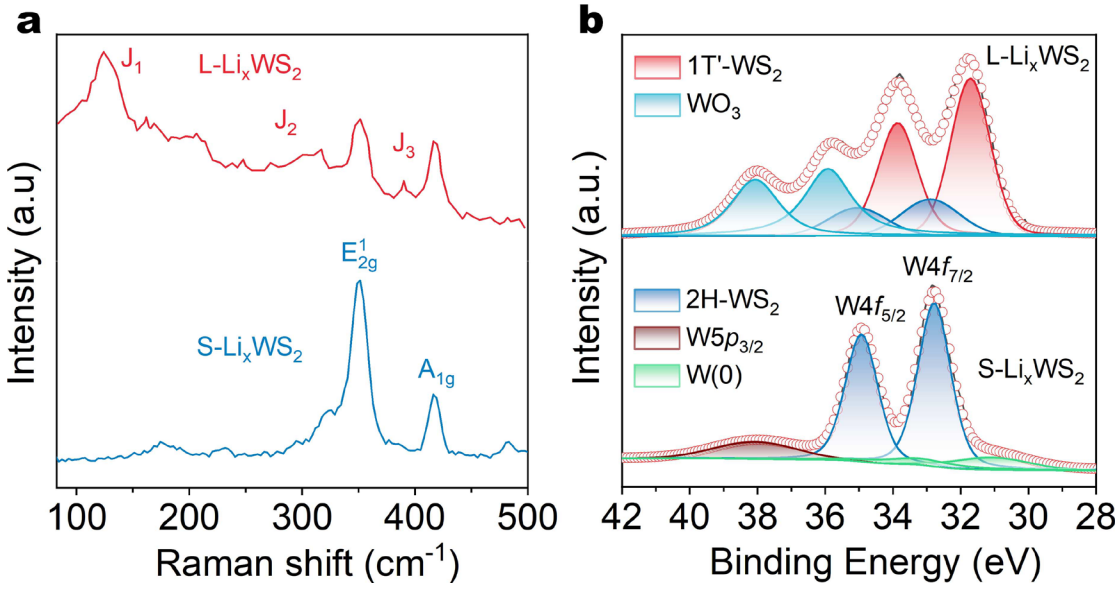

233

234 **Supplementary Fig. 22 | Characterizations of S-Li$_x$WS$_2$ and L-Li$_x$WS$_2$. a**, Raman

235 spectrum **b**, and W 4*f* XPS spectrum. S-Li$_x$WS$_2$, L-Li$_x$WS$_2$ denote as Li^+ intercalation

236 of WS$_2$ by small and large discharge current densities, respectively.

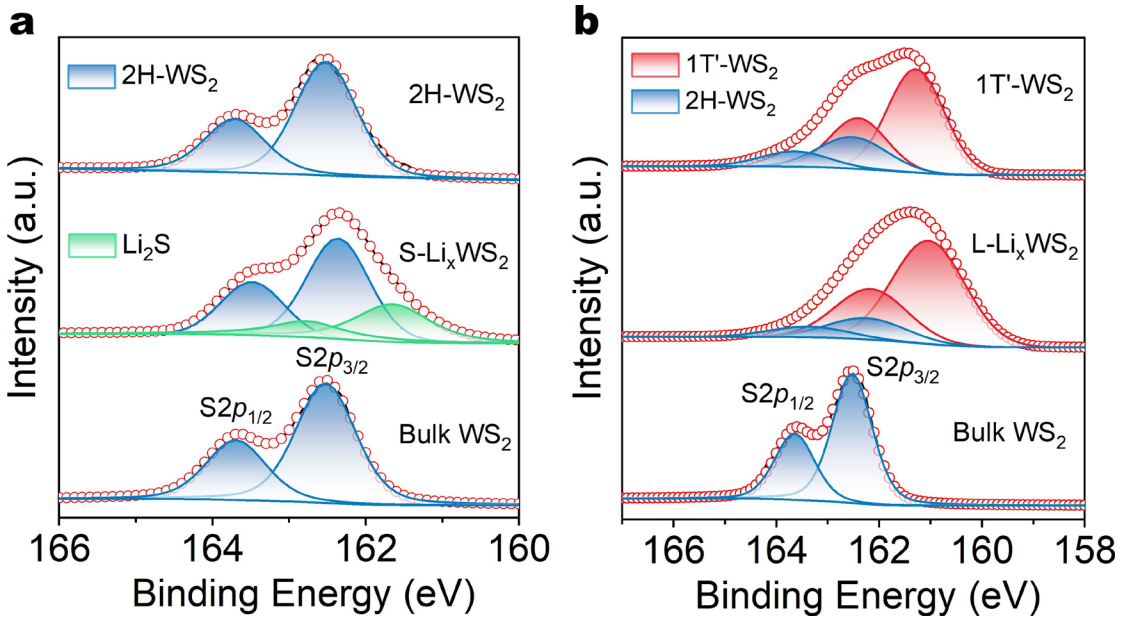

237

238 **Supplementary Fig. 23 | a-b, S 2*p* XPS spectrum of bulk WS_2, S-Li_xWS_2, L-Li_xWS_2,**
239 **as well as exfoliated 2H- and 1T′-WS_2.** S-Li_xWS_2, L-Li_xWS_2 denote as Li^+
240 intercalation of WS_2 by small and large discharge current densities, respectively.

241 As shown in **Supplementary Fig. 23a**, both bulk WS_2 and the corresponding exfoliated
242 WS_2 exhibit the same peak positions for S2$p_{3/2\text{-}1/2}$ (162.52 and 163.64 eV). However,
243 these peaks show a slight shift of approximately 0.14 eV toward lower binding energy
244 for discharged S-Li_xWS_2. This shift can be attributed to electron donation from
245 intercalated Li to WS_2.[4] However, the limited electron transfer is insufficient to induce
246 the phase transition,[5,6] keeping S-Li_xWS_2 in the 2H phase. Conversely, in addition to
247 the doublets at 162.52 and 163.64 eV, assigned to the S2$p_{3/2\text{-}1/2}$ of 2H-WS_2, two
248 dominant peaks at lower binding energies of 162.40 and 161.28 eV corresponding to
249 1T′-WS_2 are also noted (**Supplementary Fig. 23b**). These XPS results confirm the
250 absence of phase transition for S-Li_xWS_2 and the subsequent exfoliation process, while
251 a phase transition from 2H to 1T′ occurred for L-Li_xWS_2 and the corresponding
252 exfoliated product. These findings are consistent with the results obtained from Raman
253 (**Fig. 1d**, **Supplementary Fig. 22a**) and HAADF-STEM analyses (**Fig. 2d, j**).

254 Notably, the peaks corresponding to W(0) and Li_2S are evident in the W4*f*
255 (**Supplementary Fig. 22b**) and S2*p* (**Supplementary Fig. 23a**) spectra of S-Li_xWS_2,

indicating that partial WS_2 decomposed into W(0) and Li_2S during the lithium intercalation. These results aligned well with the observation of S vacancies in the cross-sectional HAADF-STEM image of S-Li_xWS_2 (**Fig. 2d**).

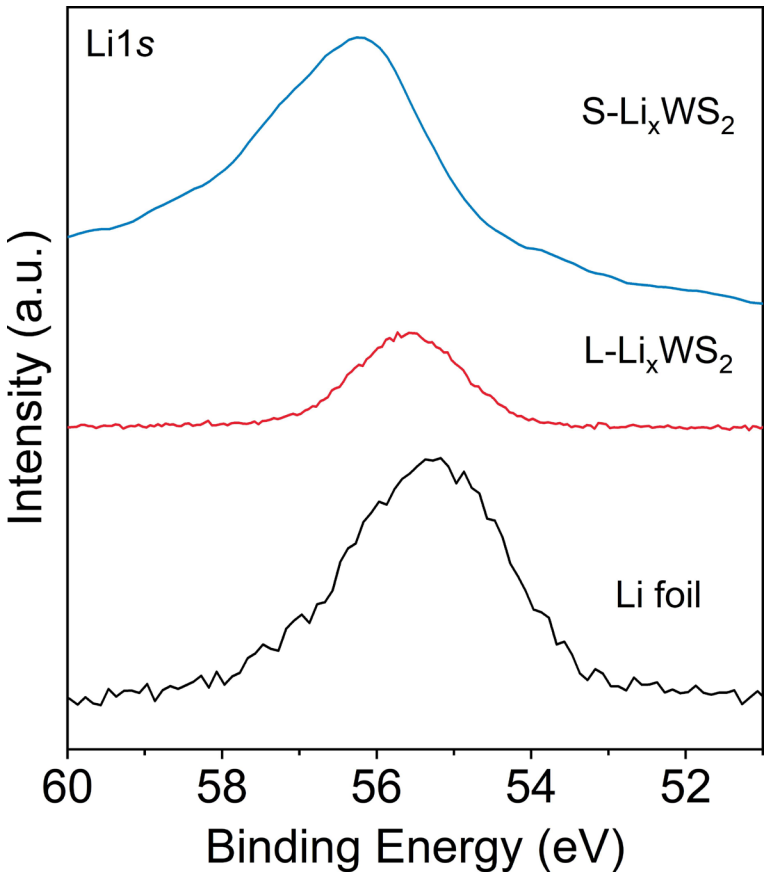

Supplementary Fig. 24 | High-resolution XPS Li1*s* spectra of S-Li$_x$WS$_2$, L-Li$_x$WS$_2$ and Li foil. Three samples are tested in the same batch. S-Li$_x$WS$_2$, L-Li$_x$WS$_2$ denote as Li^+ intercalation of WS$_2$ by small and large discharge current densities, respectively.

As shown in **Supplementary Fig. 24**, the binding energy of Li in Li foil, L-Li$_x$WS$_2$, and S-Li$_x$WS$_2$ is measured at 55.24 eV, 55.57 eV and 56.25 eV, respectively. These values reveal that the valence of Li in L-Li$_x$WS$_2$ is slightly higher than that in Li foil, which is indicative of electrons transferring from the intercalated Li to WS$_2$.[1] However, the valence of Li in L-Li$_x$WS$_2$ is significantly lower than that in S-Li$_x$WS$_2$, primarily due to the presence of the solid electrolyte interphase (SEI) and Li$_2$S in S-Li$_x$WS$_2$. Furthermore, it's worth noting that the peak intensity in L-Li$_x$WS$_2$ is notably weaker compared to S-Li$_x$WS$_2$.

This observation likely stems from the increased concentration of intercalated Li within the surface SEI of S-Li$_x$WS$_2$ and the formation of Li$_2$S (**Fig. 2a-c, f**). Notably, the XPS technique exactly performs surface measurements.

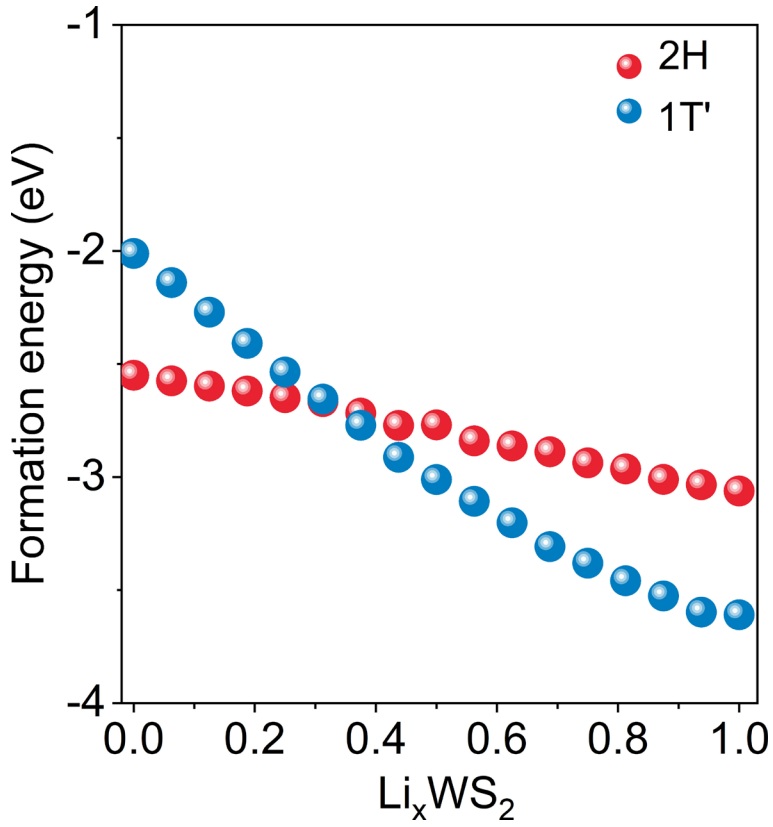

Supplementary Fig. 25 | Phase formation energy of different intercalated Li content in Li_xWS_2.

As illustrated in **Supplementary Fig. 25**, when the intercalated Li content (x) in the interlayer spacing of WS_2 exceeds 0.3, the formation energy for 1T′-WS_2 becomes more negative than that for 2H-WS_2. This suggests a phase transition from 2H to 1T′ occurs because the energy is more favorable for the 1T′ structure.

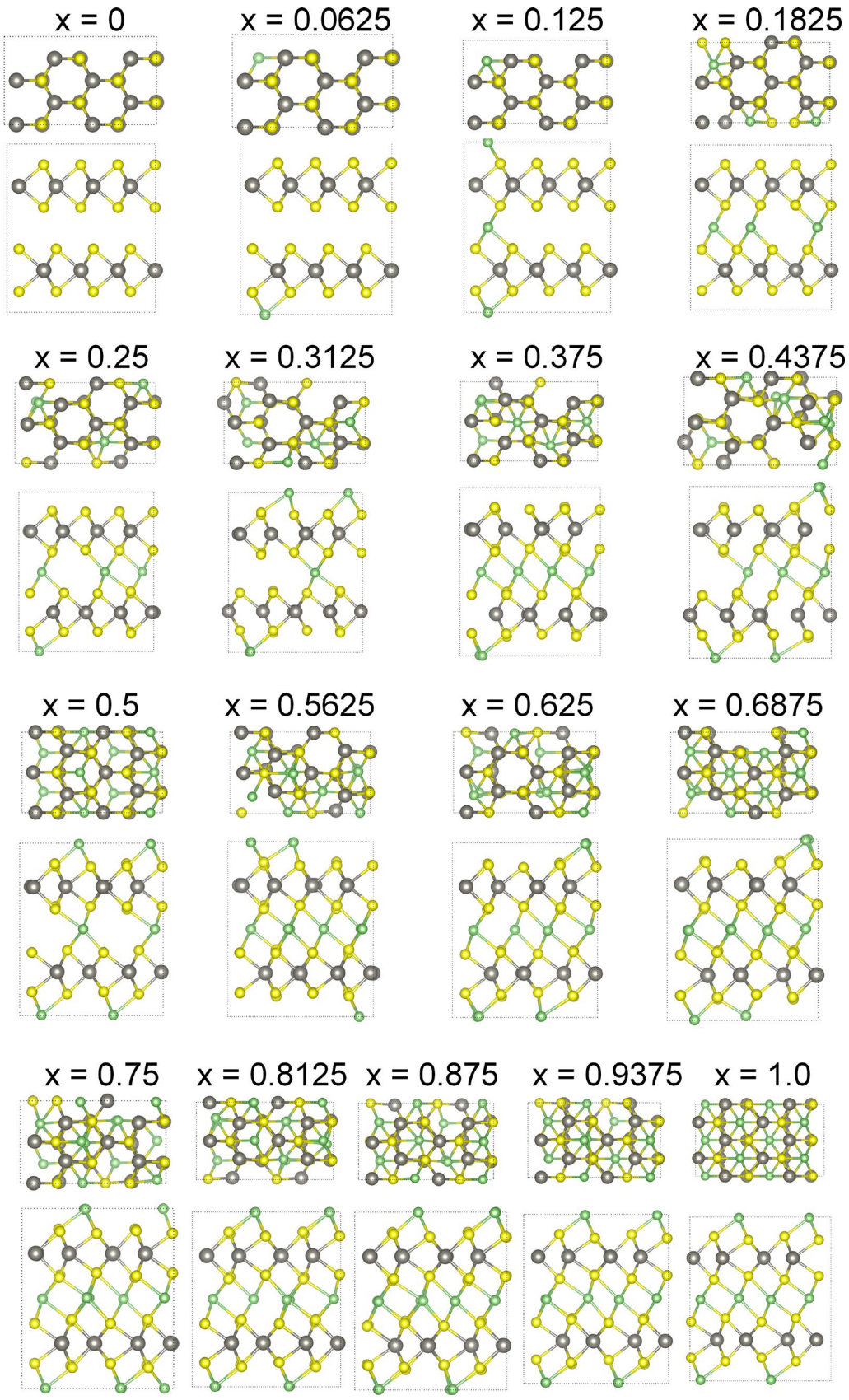

Supplementary Fig. 26 | Top and side views of optimized Li-intercalated 2H-WS_2 structures. x denote as the mole ratio of Li versus WS_2 (Li_xWS_2).

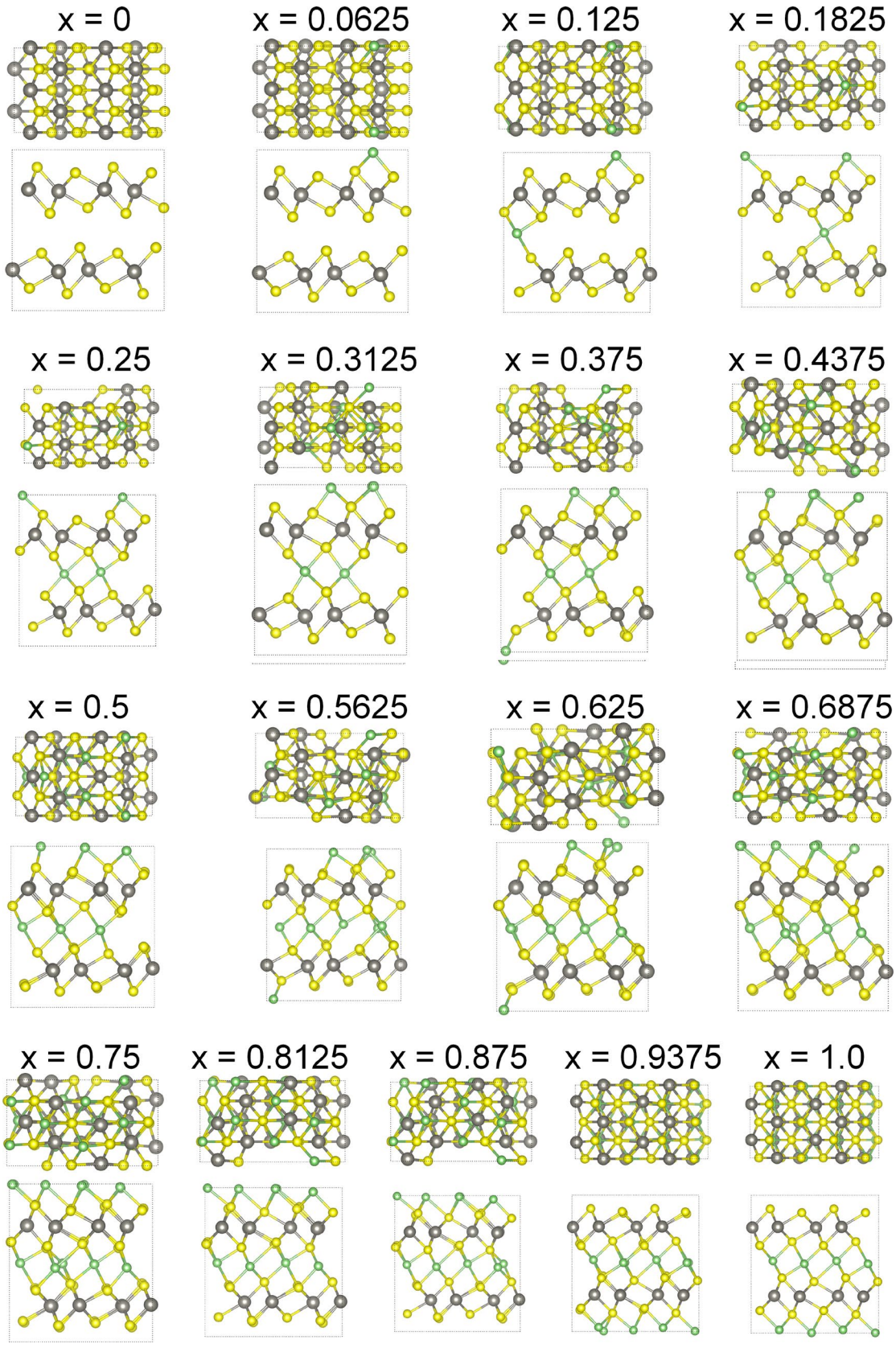

Supplementary Fig. 27 | Top and side views of optimized Li-intercalated 1T′-WS_2 structures. x denote as the mole ratio of Li versus WS_2 (Li_xWS_2).

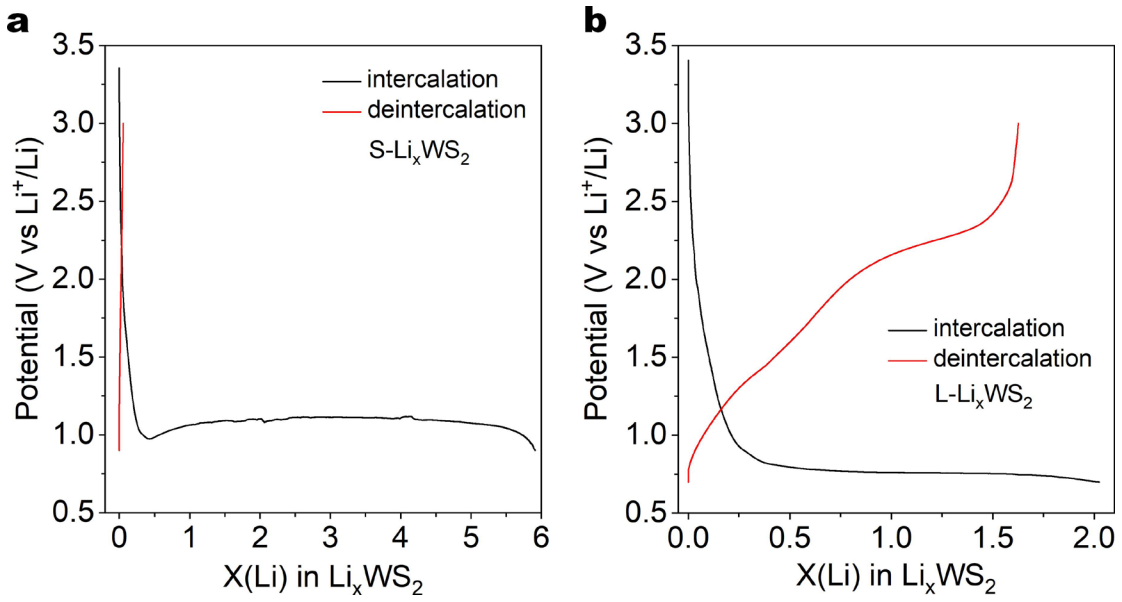

Supplementary Fig. 28 | Galvanostatic charge/discharge profiles of WS_2. a, discharge /charge current at 0.005 A g^{-1} and cutoff voltage at 0.9 V. **b**, discharge /charge current at 0.02 A g^{-1} and cutoff voltage at 0.7 V. S-Li$_x$WS$_2$, L-Li$_x$WS$_2$ denote as Li^+ intercalation of WS_2 by small and large discharge current densities, respectively.

As shown in **Supplementary Fig. 28a**, when operating with a smaller current during the discharge/charge process, a significant portion of the lithium (about 99.06%) cannot be effectively deintercalated. This leads to a rapid completion of the charge process. This outcome is a result of a substantial portion of the lithium in S-Li$_x$WS$_2$ not intercalating into the interlayer of WS_2 but rather forming the SEI and Li_2S on the surface. Consequently, S-Li$_x$WS$_2$ maintains its 2H phase. The reactions responsible for generating the SEI and Li_2S are irreversible, which significantly shortens the duration of the charge process. Conversely, in the discharge/charge process using a larger current (**Supplementary Fig. 28b**), about 81.32% of the lithium can be successfully extracted from the L-LixWS$_2$. This is because lithium can readily penetrate into the interlayer of WS_2, causing a phase transition, which is a reversible process.

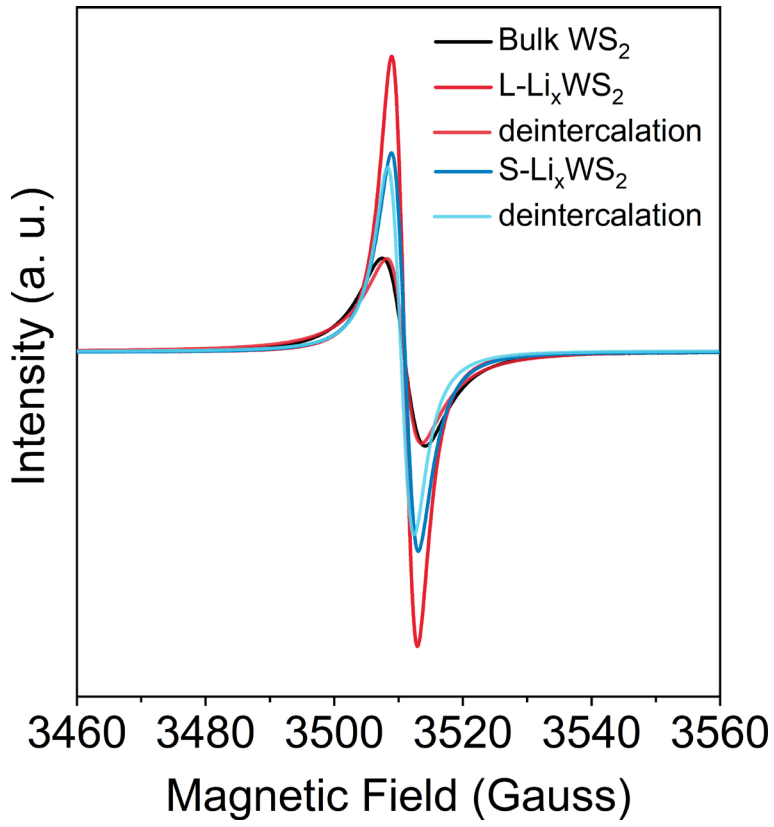

Supplementary Fig. 29 | Structure characterization of bulk WS_2 after discharge and charge process. EPR spectrums of bulk WS_2, L-Li_xWS_2, L-Li_xWS_2-deintercalation, S-Li_xWS_2 and S-Li_xWS_2-deintercalation. S-Li_xWS_2, L-Li_xWS_2 denote as Li^+ intercalation of WS_2 by small and large discharge current densities, respectively. Five samples are tested in the same batch.

As illustrated in **Supplementary Fig. 29**, following the deintercalation of L-Li_xWS_2 through the charge process under the same current, there is a substantial decrease in S vacancies, which remains slightly higher than that in bulk WS_2. This decrease in vacancies can be attributed to the extraction of a significant amount of intercalated lithium from the interlayer of WS_2. Conversely, after the deintercalation of S-Li_xWS_2, the reduction in S vacancies is minimal. This minimal decrease can be attributed to the fact that only a very small amount (0.94%) of lithium is extracted from S-Li_xWS_2. These EPR results highly aligns with the conclusions drawn from the discharge/charge curves (**Supplementary Fig. 28**).

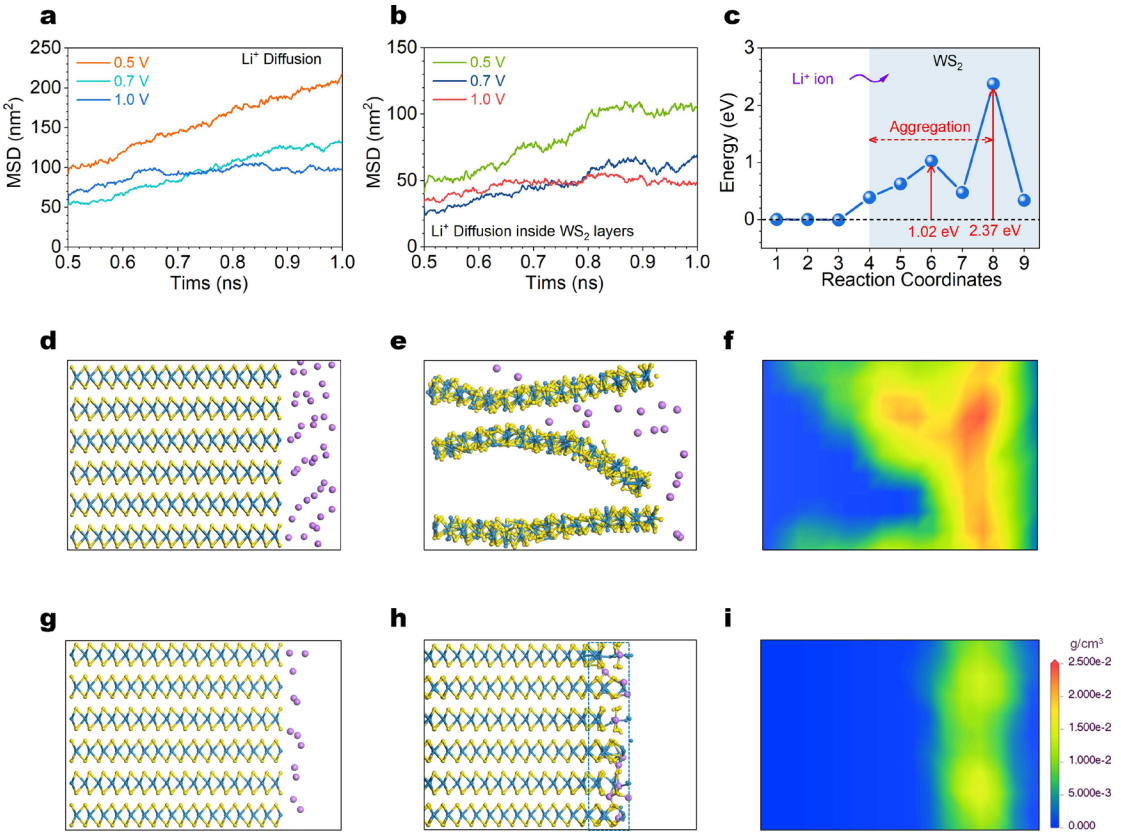

Supplementary Fig. 30 | Theoretical simulations of the formation of the solid electrolyte interface (SEI) under large and small discharge current densities. a, The mean square displacement (MSD) of Li^+ under different potentials. **b**, The MSD of Li^+ within the interlayer direction (y-axis) of WS_2. **c**, The diffusion energy barriers of Li^+ in the WS_2 layers. The structure models under **d** large discharge current density and **g** small discharge current density simulations. The structures of WS_2 for **e** large discharge current density and **h** small discharge current density. The Li^+ density distributions in WS_2 under the **f** large discharge current density and **i** small discharge current density.

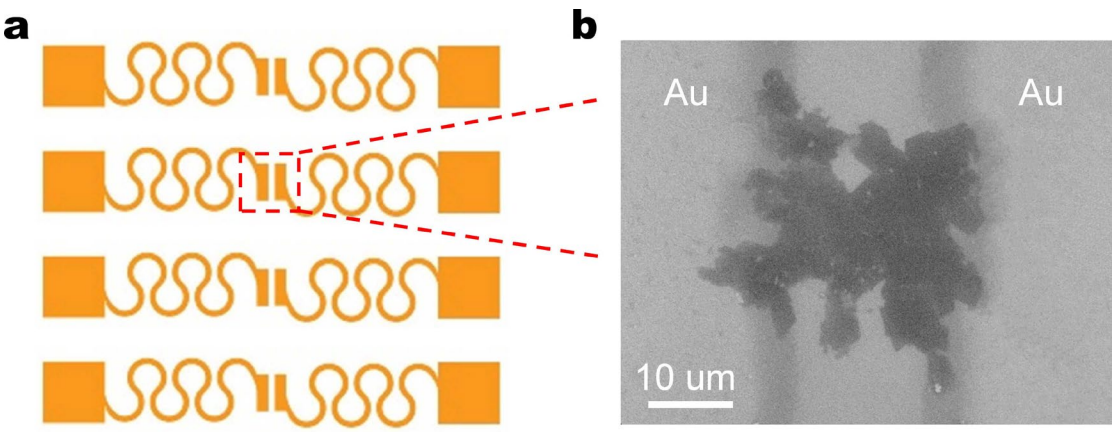

Supplementary Fig. 31 | Morphology characterization of 2H-WS_2 NSs based humidity sensor device. a, Schematic of the device. **b**, SEM image of 2H-WS_2 NSs as the active channel for device fabrication.

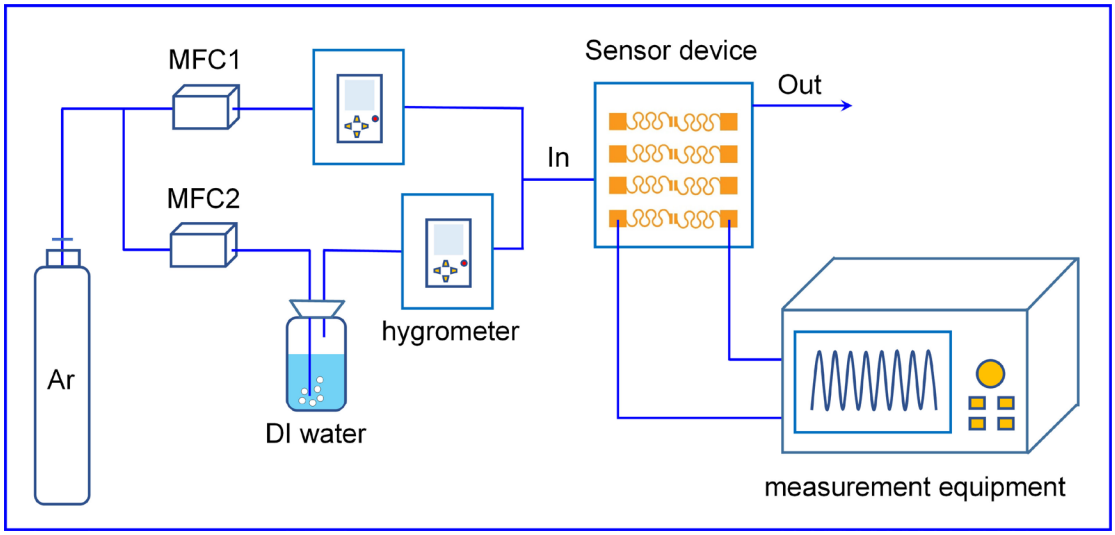

Supplementary Fig. 32 | Schematic diagram of home-made equipment for humidity sensing performance tests. MFC denotes as mass flow controller. MFC1 and MFC2 are the mass flowmeter.

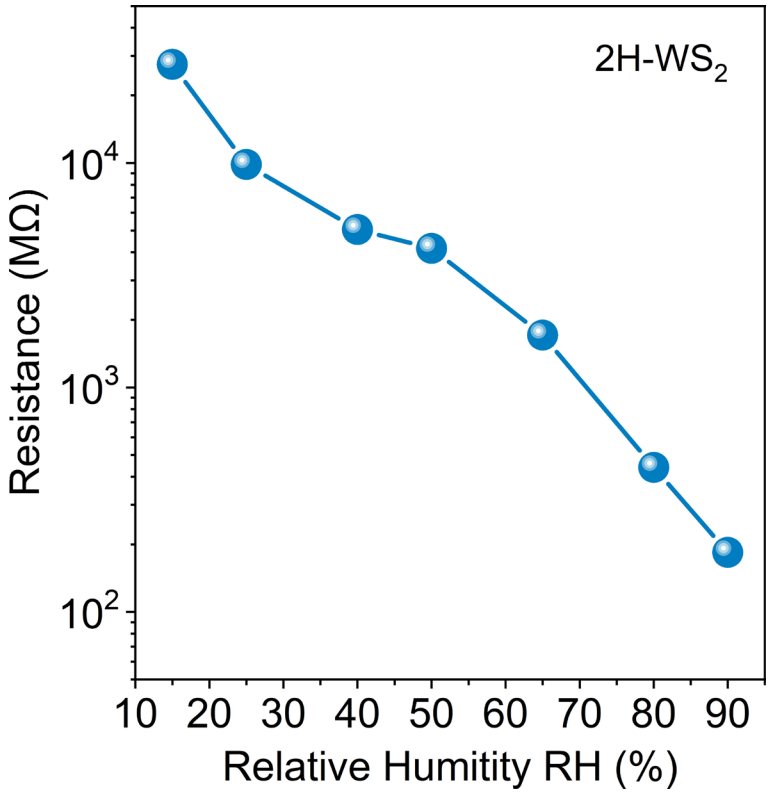

Supplementary Fig. 33 | Resistance variation of the 2H-WS_2 NSs based humid sensor under different RH levels.

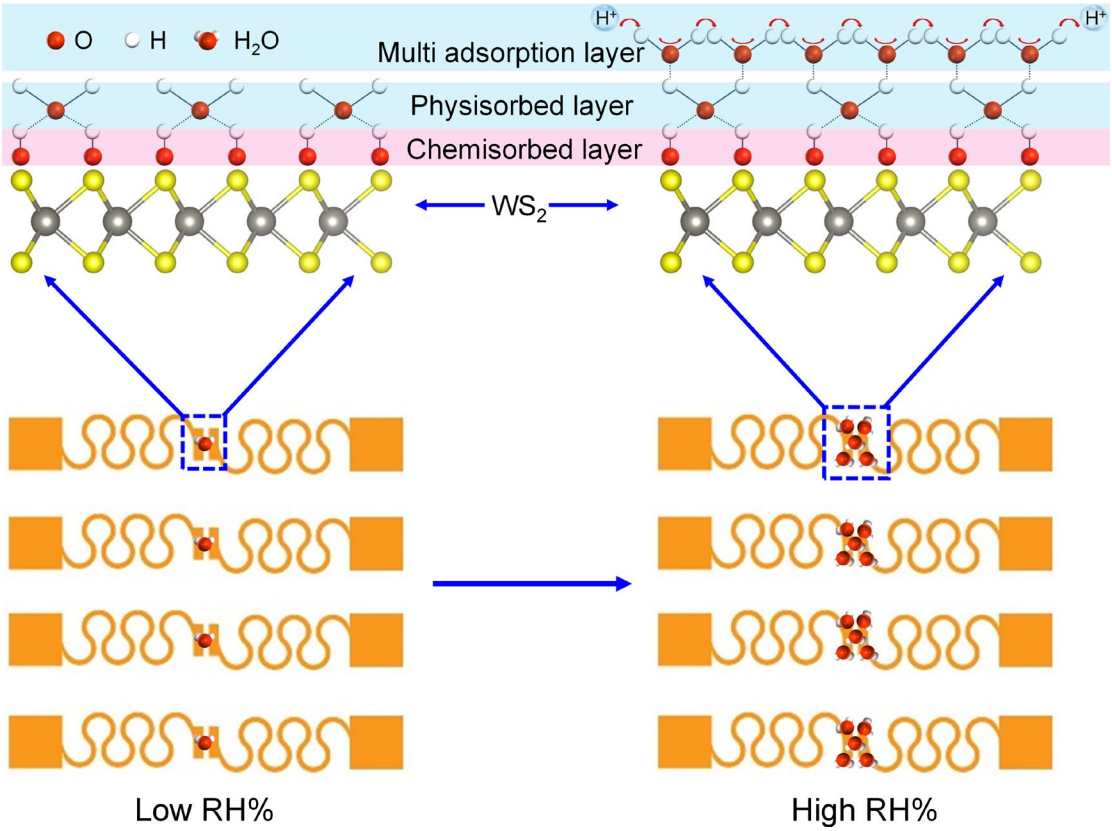

Supplementary Fig. 34 | Schematic of the humidity-sensing mechanism for WS_2 NSs under different RH% level.

The WS_2 humidity sensing mechanism closely resembles that of most humidity sensors, as depicted in **Supplementary Fig. 34**. At lower relative humidity (RH) levels, only a small quantity of water molecules from the surrounding air adhere to the WS_2 surface, where they ionize into H_3O^+ and OH^- ions. These OH^- ions are captured by surface atoms within the sensing layer, forming a chemisorbed layer. These ions exhibit limited mobility, resulting in an elevated sensor resistance. As RH levels increase, water molecules continue to accumulate on the chemisorbed layer through hydrogen bonding, forming the initial physical adsorption layer. With exposure to higher RH levels, an increasing number of water molecules adsorb onto this physical adsorption layer, creating a continuous aqueous layer that facilitates the generation of a substantial amount of H_3O^+ ions. Moreover, the H_3O^+ ions can readily transfer within the continuous aqueous layer through the Groutthuss chain reaction ($H_2O + H_3O^+ = H_3O^+ + H_2O$), ultimately leading to a reduction in sensor resistance (**Supplementary Fig. 33**).

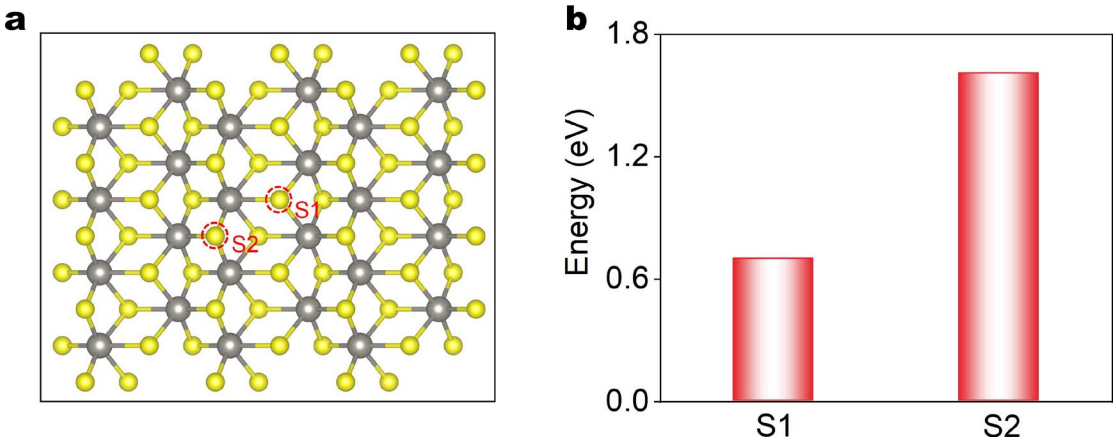

Supplementary Fig. 35 | DFT calculations for sulfur vacancy in 1T′-WS_2. a, Schematic of the possible sulfur vacancy S1 and S2 in 1T′-WS_2. **b**, The energy that need for generating S1 and S2 vacancy in **a**. Note that generation of sulfur vacancy S1 is more energy favorable than S2 (0.70 eV vs 1.61 eV), therefore sulfur vacancy S1 is selected to do the DFT calculation for H_2O molecule adsorption on 1T′-WS_2.

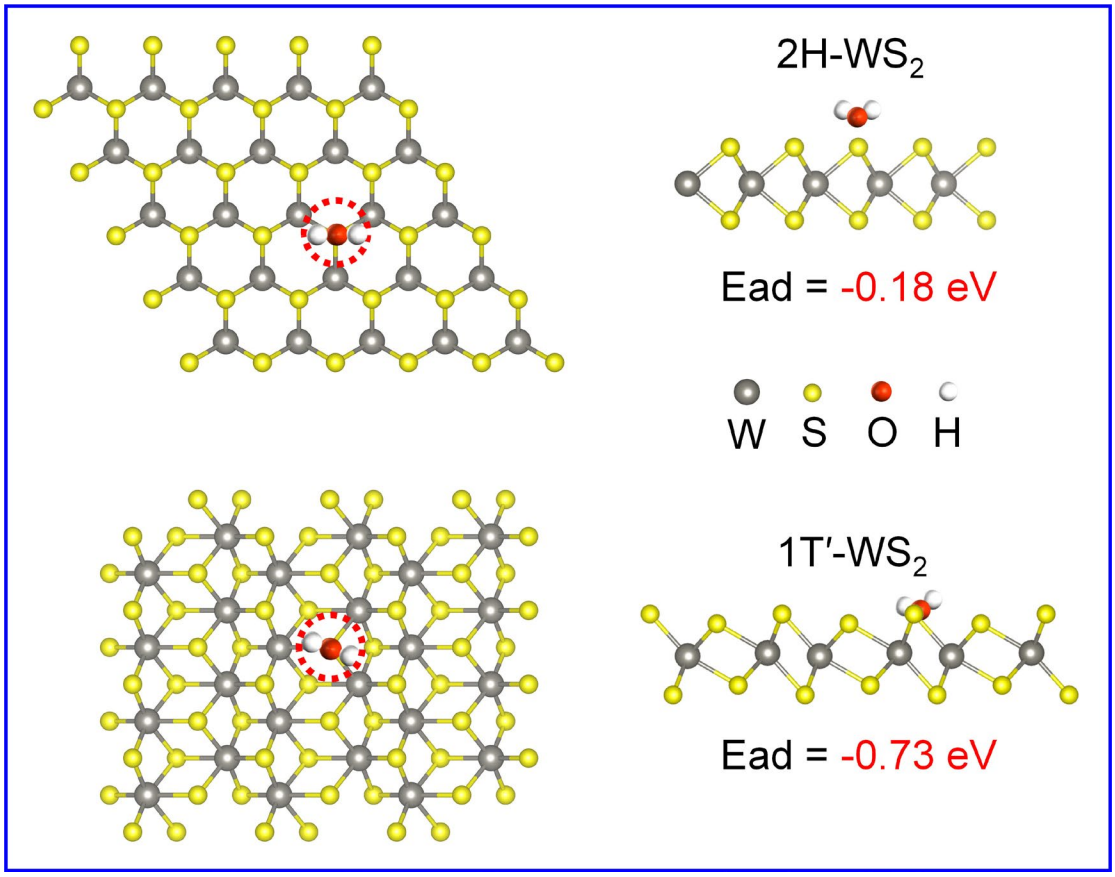

Supplementary Fig. 36 | Adsorption energy of H_2O molecule on 2H- and 1T′-WS_2.

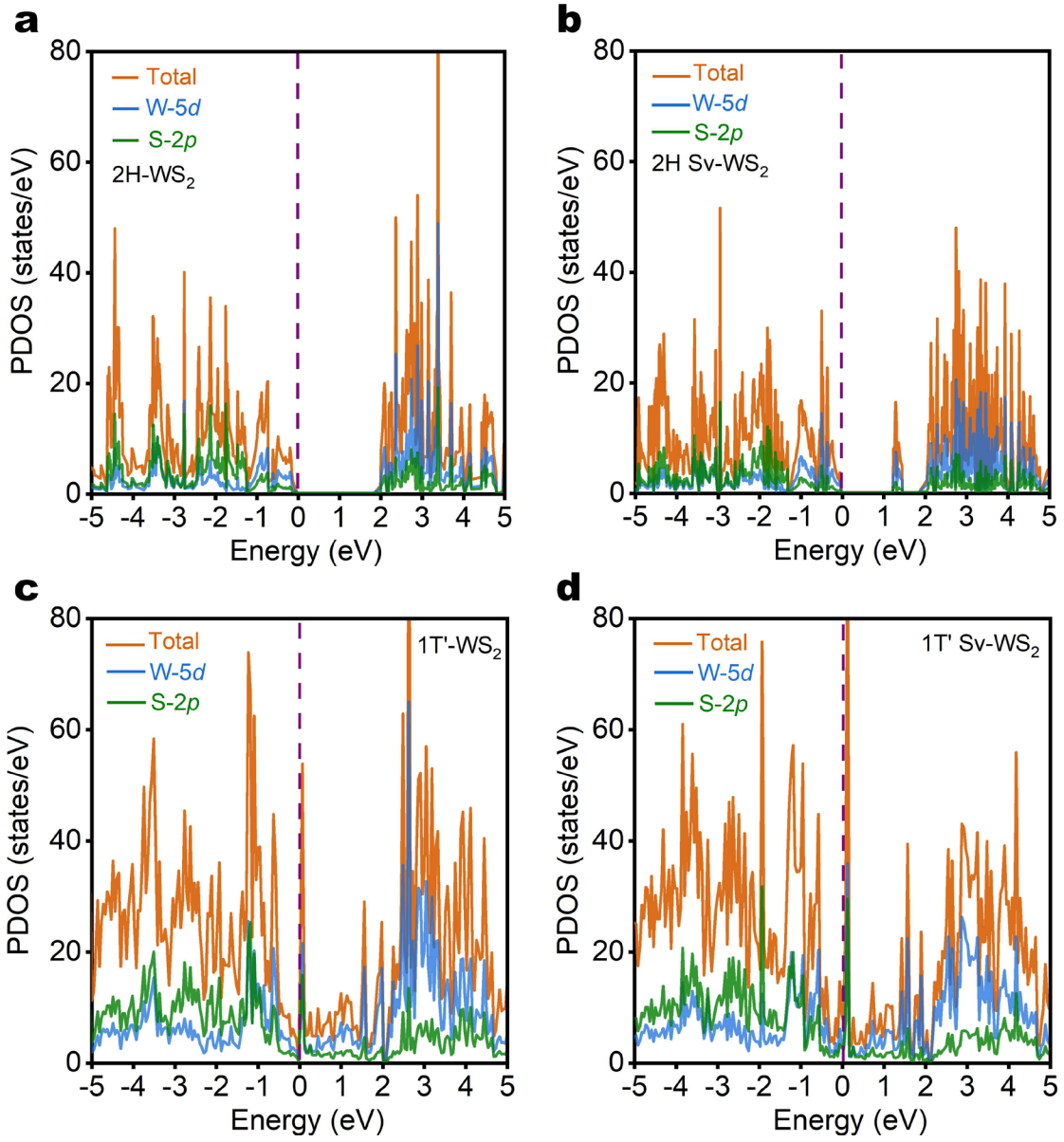

Supplementary Fig. 37 | DFT calculation of projected density of states for the 2H- and 1T′-WS_2 with the sulfur vacancy (Sv). The projected density of states for **a** 2H-WS_2 and **b** 2H Sv-WS_2, **c** 1T′-WS_2 and **d** 1T′ Sv-WS_2. The red dotted line corresponds to the Fermi level.

To gain a deeper understanding of the variation in electronic properties of 2H- and 1T′-WS_2 caused by the presence of S vacancy, we conducted calculations of the projected density of states (PDOS) for 2H-WS_2, 2H Sv-WS_2, 1T′-WS_2 and 1T′ Sv-WS_2 using density functional theory. These results are presented in **Supplementary Figure 37. Supplementary Fig. 37a** show the PDOS of pristine 2H-WS_2, which exhibits a wide bandgap of 1.88 eV, indicative of its semiconductor properties. It is worth mentioning

that this bandgap value aligns with the primitive cell calculation.[7] In the case of 2H Sv-WS_2 as shown in **Supplementary Fig. 37b**, the bandgap becomes noticeably narrower, with a value of 1.24 eV after introducing a S vacancy on the WS_2 surface. This narrowing is attributed to the hybridization of the 2p orbital of S atoms and the 5d orbital of W atoms within the forbidden band, generating a new energy level. This shift causes the bottom of the conduction band to move closer to the Fermi energy. The significant reduction in the bandgap of WS_2 after introducing a S vacancy can effectively promote electron transfer and enhance conductivity. For 1T′-WS_2, after the introduction of a S vacancy, the generation of new orbitals around the orbital energy levels, as shown in **Supplementary Fig. 37c-d**, might contribute to the adsorption of H_2O onto WS_2.

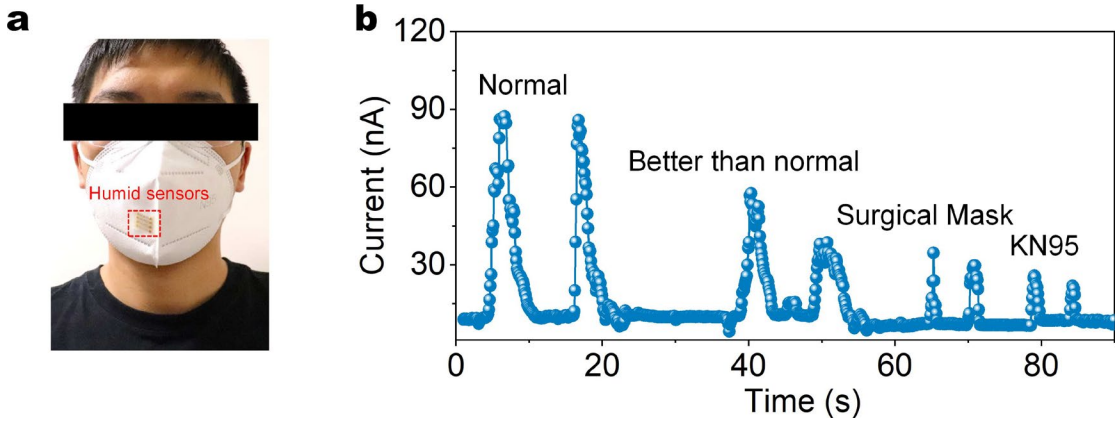

Supplementary Fig. 38 | Test the protection performance of different masks via using 2H-WS_2 based humidity sensor. **a**, Optical image of the 2H-WS_2 humidity sensor attached outside the mask. **b**, Dynamic humidity response and recovery measurement for different levels of masks.

As demonstrated in **Supplementary Fig. 38a**, the WS_2 humidity sensor was attached outside the masks to evaluate their effectiveness in protecting against moisture exhaled from the mouth under ambient conditions. To simulate a person's cough or sneeze, the subject exhaled heavily during this measurement. **Supplementary Fig. 38b** presents the dynamic current of the device in response to moisture passing through different types of masks. The normal mask without any filter layer exhibited poor protective performance, with the current response suddenly exceeding 90 nA. In contrast, the KN95 mask effectively resisted the exhaled moisture, with the current only slightly increasing to approximately 25 nA. These results highlight that our WS_2 humidity sensor can serve as a sensitive and convenient method for assessing the quality of masks.

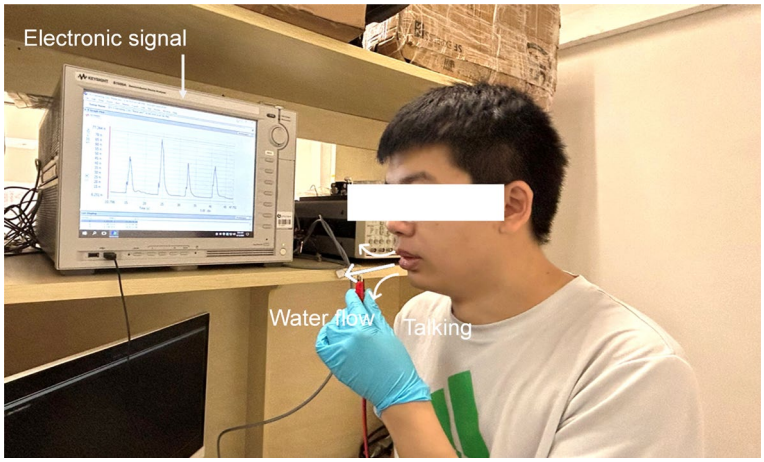

Supplementary Fig. 39 | Photograph of humidity sensor set-up for voice recognition.

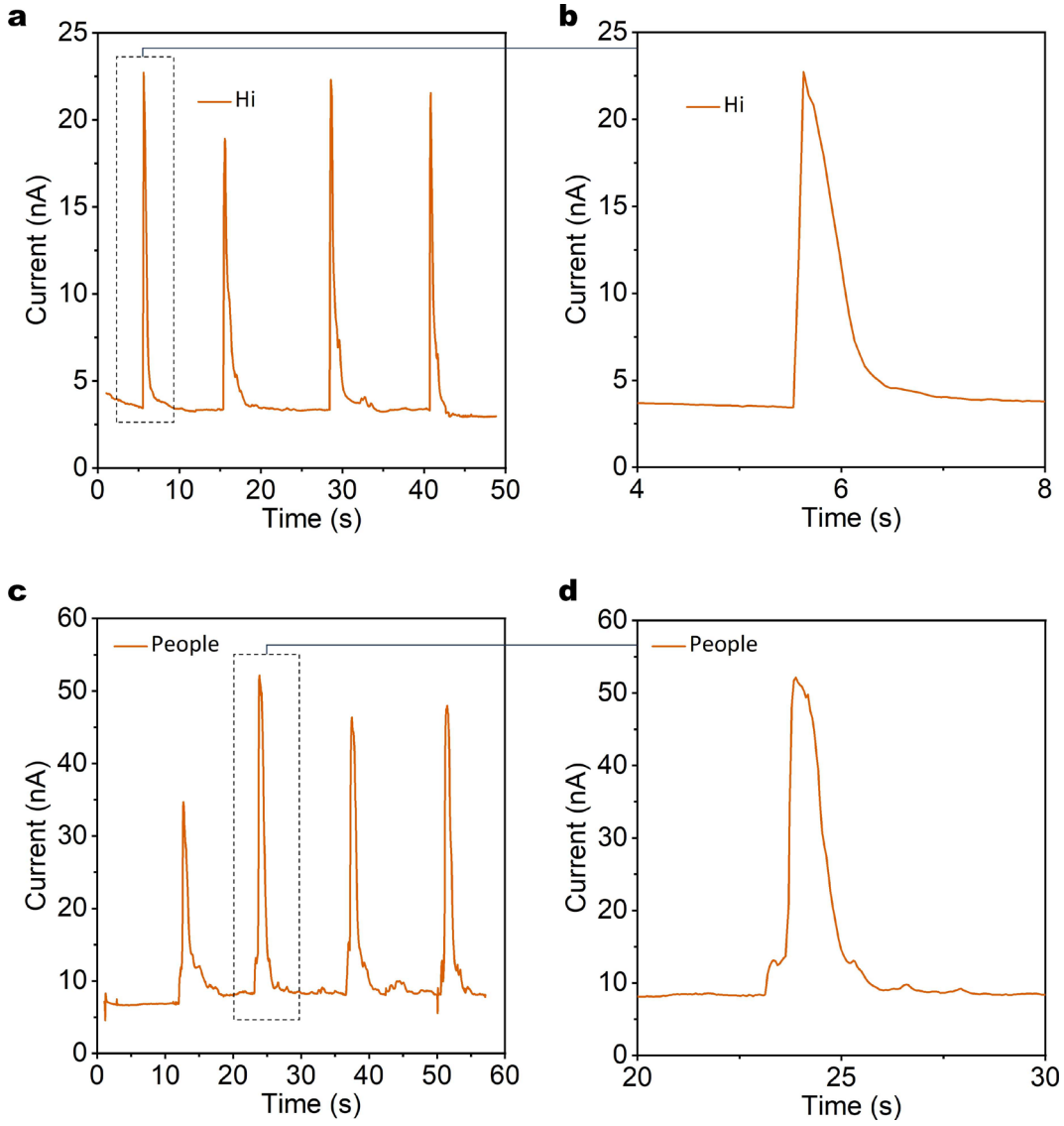

Supplementary Fig. 40 | Voice recognition of speaking different words. a-b, Response current of 2H-WS_2 while speaking "Hi", and the corresponding amplified curve. **c-d**, Response current of 2H-WS_2 while speaking "People", and the corresponding amplified curve.

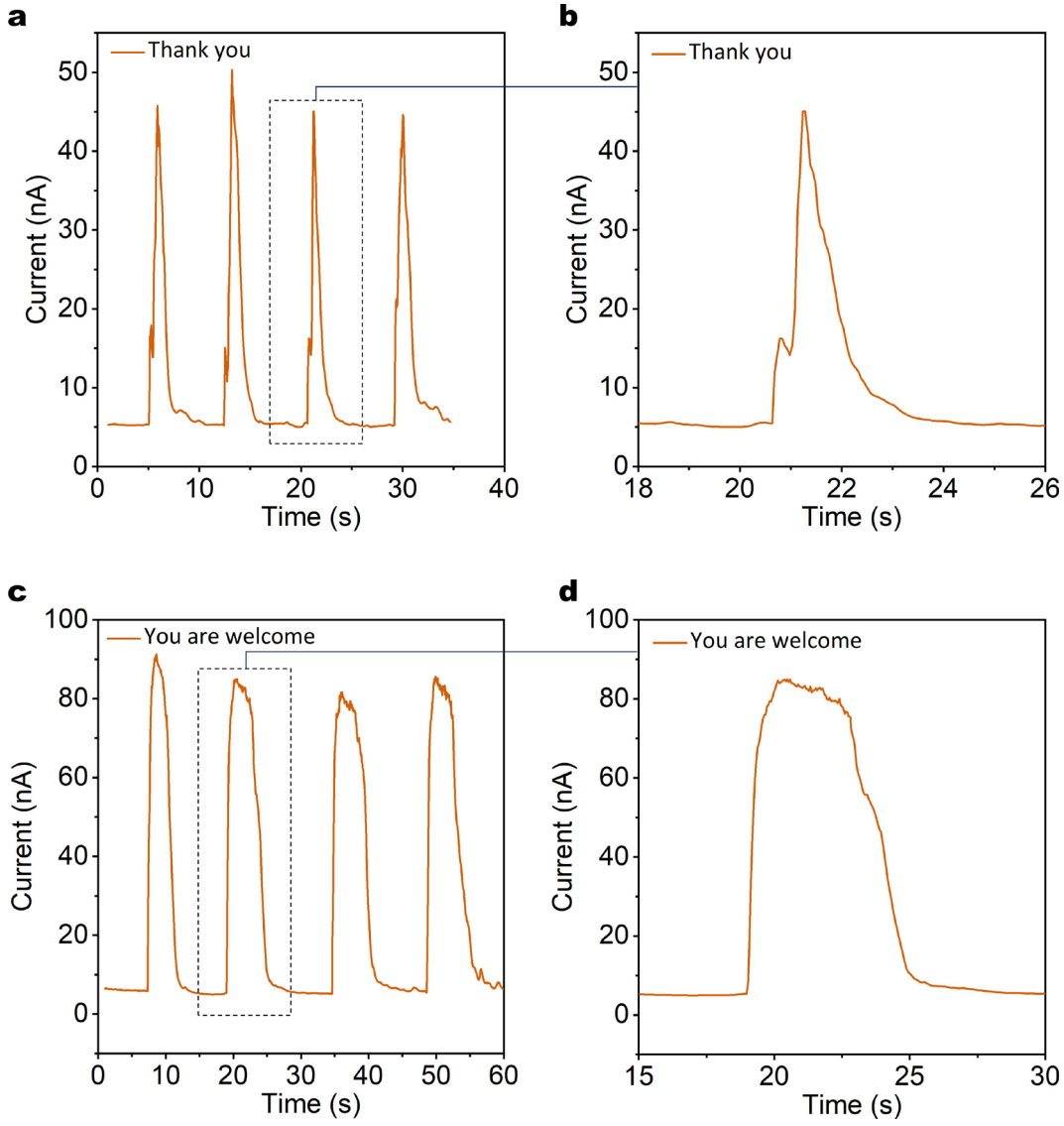

Supplementary Fig. 41 | Voice recognition of speaking different words. a-b, Response current of 2H-WS_2 while speaking "Thank you", and the corresponding amplified curve. **c-d**, Response current of 2H-WS_2 while speaking "You are welcome", and the corresponding amplified curve.

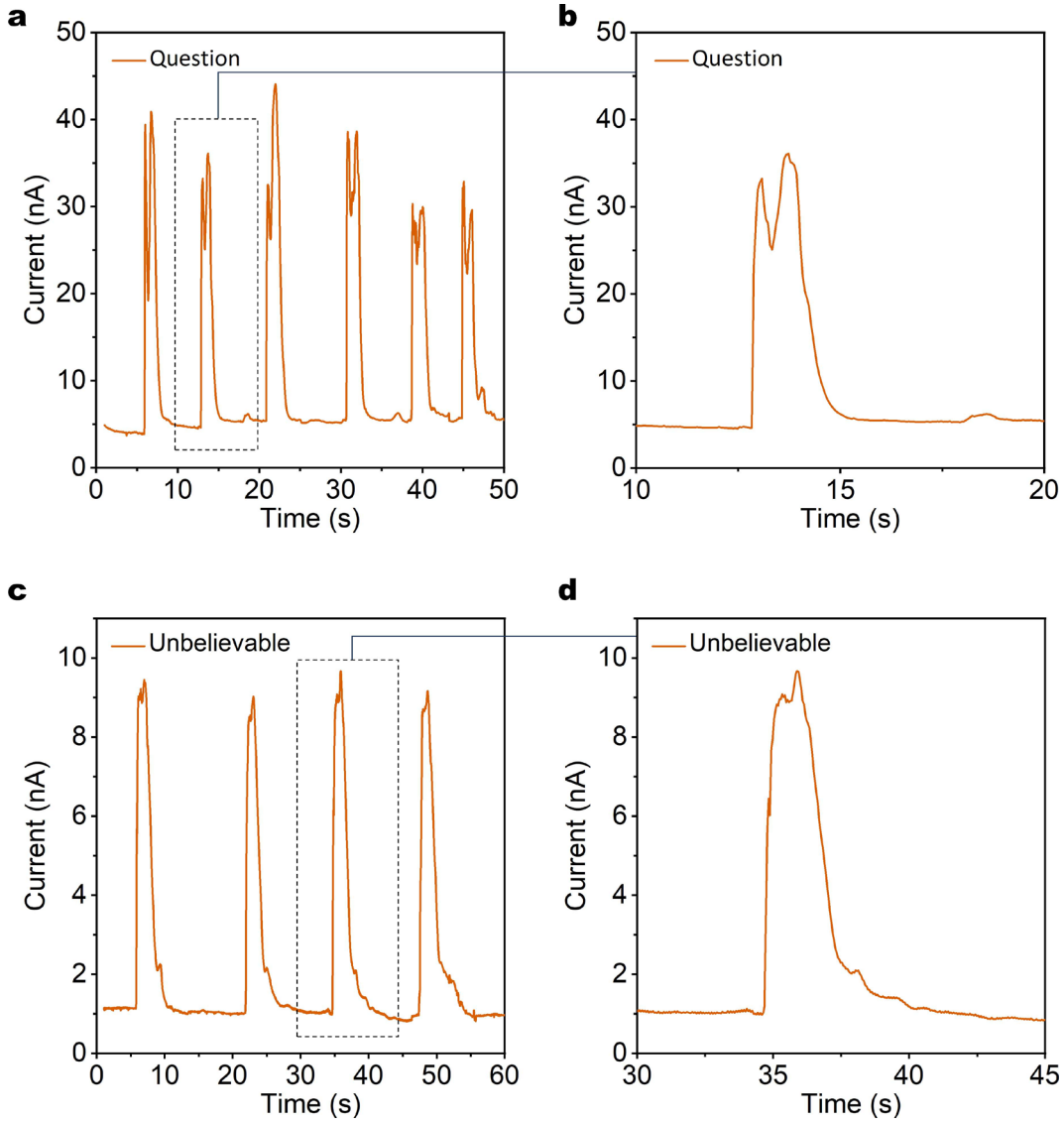

Supplementary Fig. 42 | Voice recognition of speaking different words. a-b, Response current of 2H-WS_2 while speaking "Question", and the corresponding amplified curve. **c-d**, Response current of 2H-WS_2 while speaking "Unbelievable", and the corresponding amplified curve.

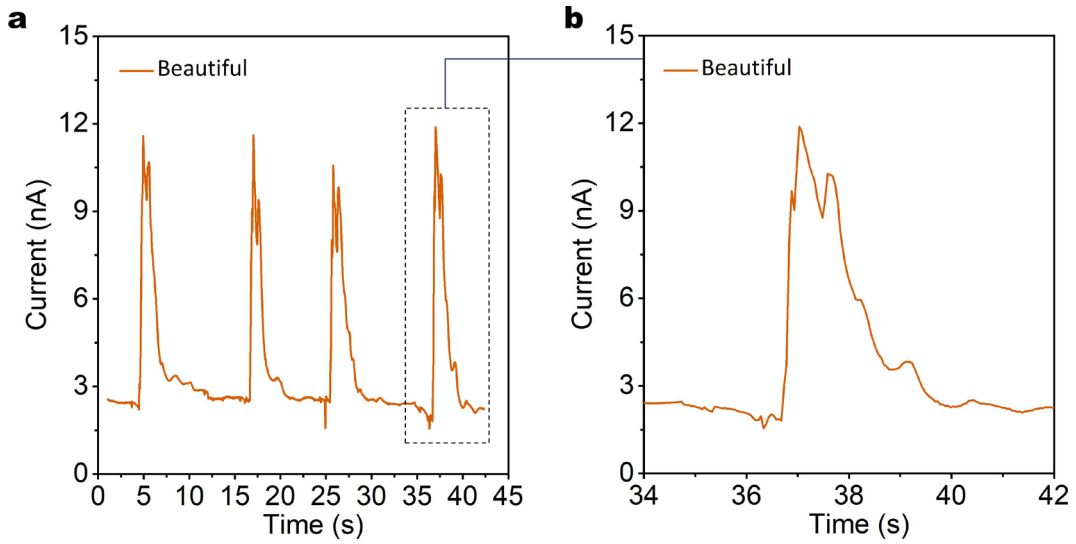

Supplementary Fig. 43 | Voice recognition of speaking different words. a-b, Response current of 2H-WS_2 while speaking "Beautiful", and the corresponding amplified curve.

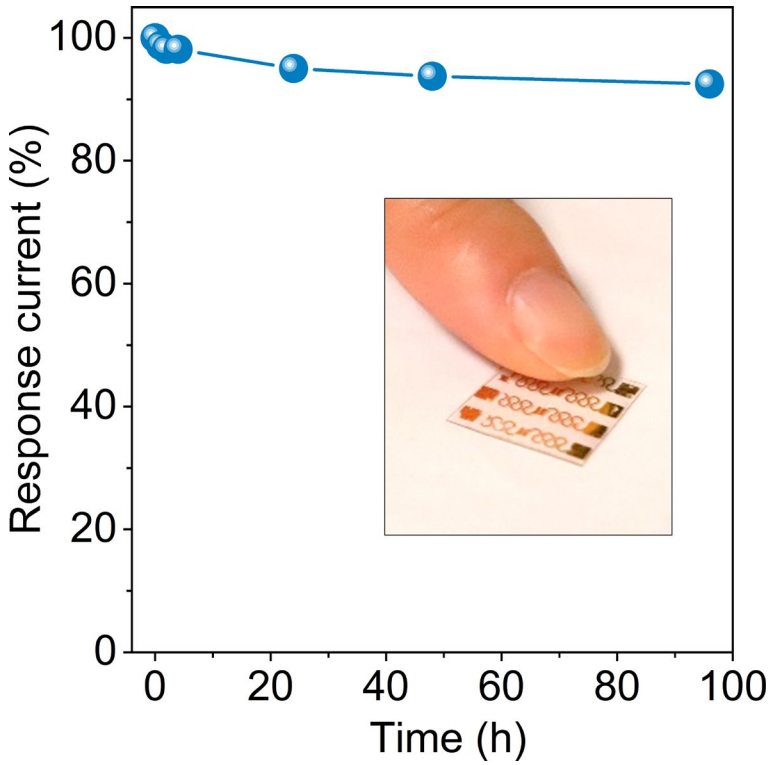

Supplementary Fig. 44 | The performance stability of 2H-WS_2 based humidity sensor device. Long-term stability test of the humidity sensor after exposing to the indoor environment (65% RH, R.T.) for different times. Inset photo shows the distance between the finger with device is 3 mm. Even after exposing for 96 h, the response current still maintains 93% of its original value, demonstrating its superior stability in indoor environment.

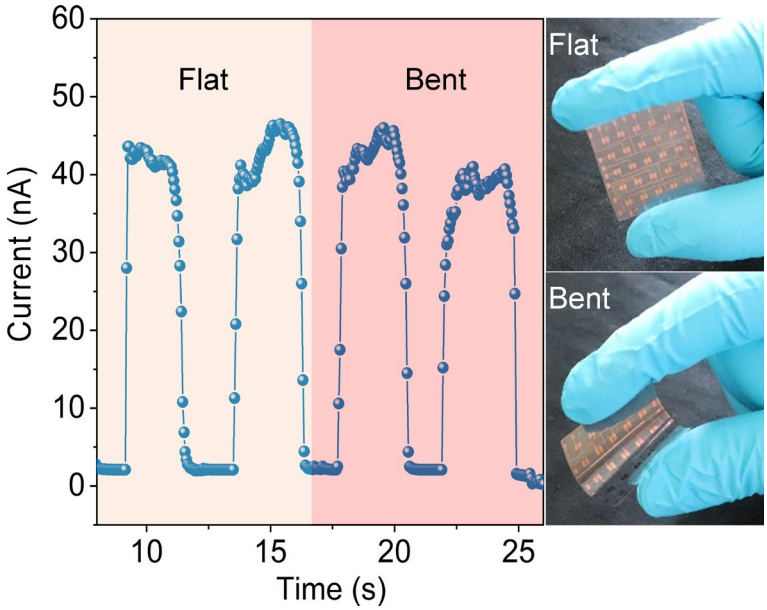

Supplementary Fig. 45 | The flexibility of 2H-WS_2 based sensor device. Dynamic humidity response and recovery measurement of the 2H-WS_2 humidity sensor array under flat and bending condition. The bend state of the device doesn't affect the sensing properties of 2H-WS_2.

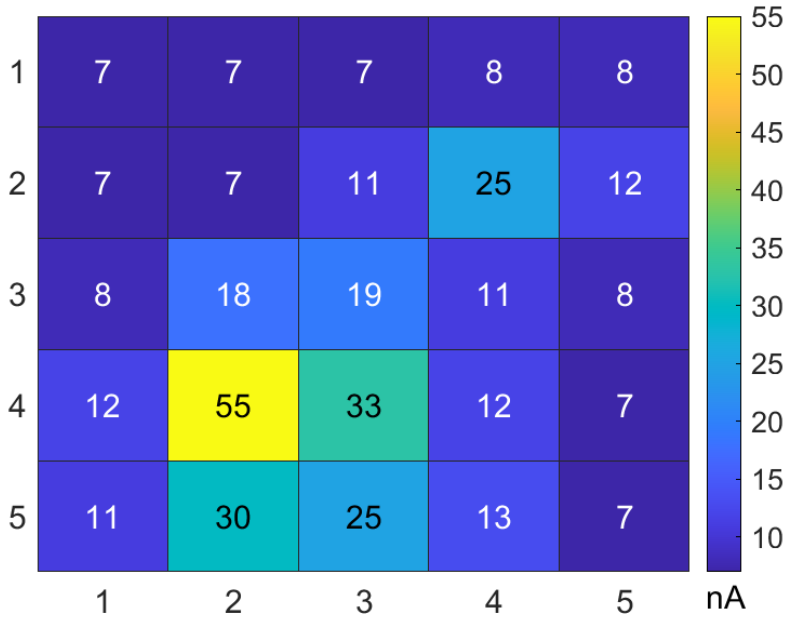

Supplementary Fig. 46 | Raw data for current distribution of humidity sensor array. Original current distribution of 5×5 humid sensor array in none-contact finger localization experiments.

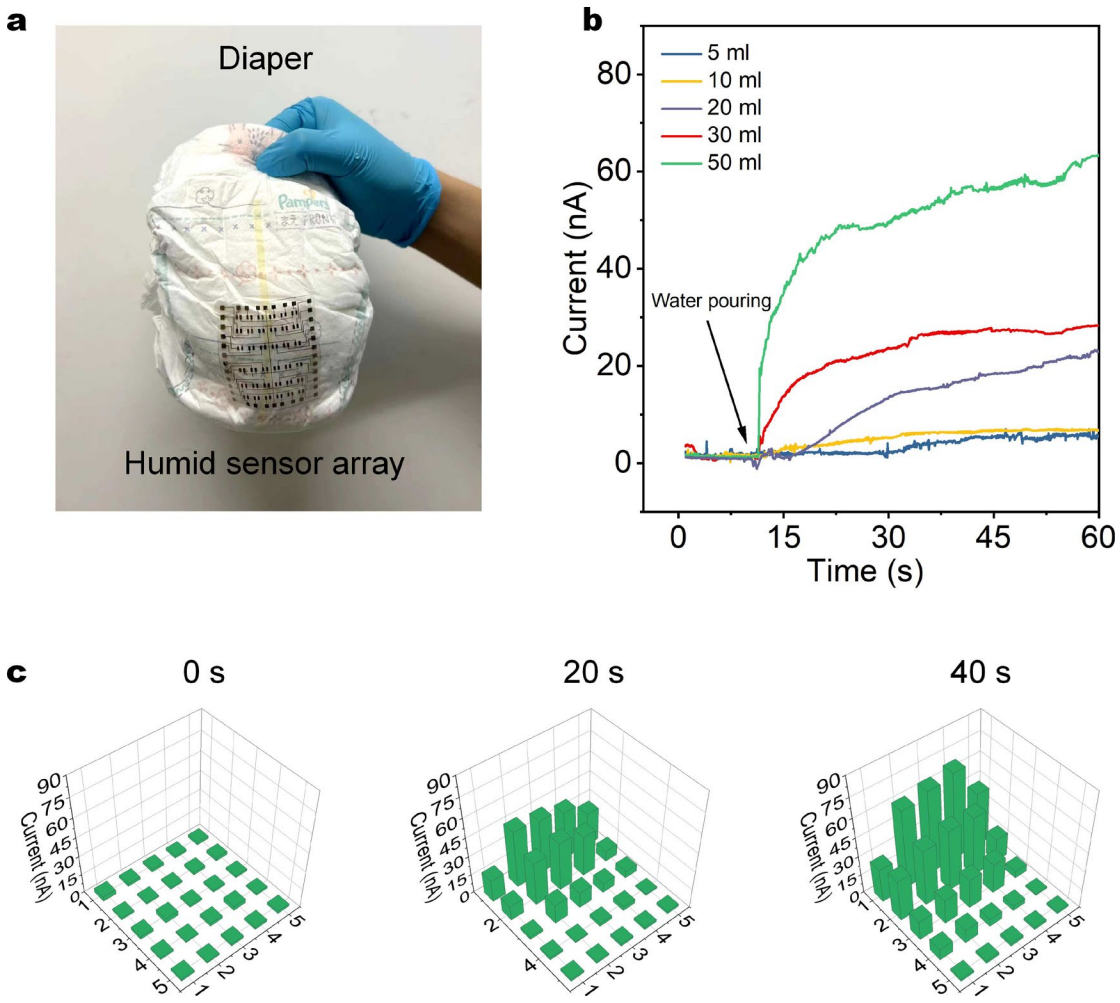

Supplementary Fig. 47 | Humidity sensor array for monitoring baby diaper wetness. a, Photograph of a baby diaper with humidity sensor array. **b**, Response current of humidity sensor array with pouring different volume of water. **c**, Current distribution of humid sensor array at different time intervals after pouring the water.

To highlight the reconfigurability and advantages of our humidity sensor array, we showcase its potential application in monitoring baby diaper wetness. Prolonged exposure to a wet diaper can lead to discomfort and potential health issues such as diaper rash or urinary tract infections. Caregivers may occasionally overlook or lack the time to manually check their baby's diaper status throughout the day. Leveraging the high sensitivity and spatial humidity resolution of our humidity sensor array, it can effectively monitor diaper moisture levels. When a baby urinates, the diaper promptly absorbs the urine into its absorbent core, causing a change in the relative humidity on the diaper's surface. By utilizing the humidity sensor array to detect these humidity

changes, we can ascertain whether the baby has urinated.

As shown in **Supplementary Fig. 47a**, the softness of the humidity sensor array enables direct and secure attachment to the outside of the baby's diaper. To test the single humidity sensor response behavior, we poured different volumes of water into the diaper (**Supplementary Fig. 47b**). When pouring 5ml or 10ml of water, due to the limited water permeation caused by the diaper's inherent absorbent capacity, the device exhibits only a weak humidity response. Upon pouring 20ml of water, there is a noticeable change in the surface humidity of the diaper, resulting in a significant increase in device current, albeit not immediately after pouring. However, pouring more than 30ml of water leads to an immediate and pronounced detection of humidity change by the device, accompanied by a clear increase in current, indicating the accumulation of a significant amount of moisture inside the diaper. This demonstrates the feasibility of individual devices for monitoring diaper wetness.

Furthermore, we measured the array current distribution at different time intervals (0s, 20s, 40s) after pouring 50ml of water. As shown in **Supplementary Fig. 47c**, as water permeates and spreads, the humidity sensor array can detect humidity gradients across large surface areas (~5×5 cm^2, enough to cover the core position) of the diaper, which are reflected in changes in the array current distribution. Higher sensor currents represent higher surface humidity. This can eliminate erroneous judgments caused by measurement errors resulting from the varying positions of individual devices. This data also provide potential aids in establishing the alarm threshold within the operational circuit system.

Supplementary Table 1 | DFT calculated phase formation energy and corresponding interlayer spacing for lithium intercalation of WS_2.

Li	2H Li_xWS_2		1T′ Li_xWS_2	
x	interlayer spacing (Å)	Formation energy (eV)	interlayer spacing (Å)	Formation energy (eV)
0	6.214	-2.549	6.034	-2.011
0.0625	6.281	-2.574	6.116	-2.140
0.125	6.361	-2.597	6.217	-2.270
0.1875	6.411	-2.619	6.244	-2.409
0.25	6.506	-2.649	6.303	-2.536
0.3125	6.546	-2.666	6.362	-2.655
0.375	6.592	-2.717	6.350	-2.771
0.4375	6.677	-2.771	6.389	-2.912
0.5	6.645	-2.769	6.405	-3.011
0.5625	6.653	-2.840	6.456	-3.107
0.625	6.704	-2.862	6.396	-3.202
0.6875	6.696	-2.888	6.386	-3.307
0.75	6.647	-2.937	6.379	-3.381
0.8125	6.635	-2.964	6.327	-3.459
0.875	6.598	-3.010	6.323	-3.526
0.9375	6.616	-3.034	6.308	-3.597
1	6.614	-3.062	6.339	-3.609

Supplementary Table 2 | Comparison of humidity sensing performance of the developed 2H and 1T′ WS_2 NSs with other reported humidity sensors.

Materials	Response time (s)	Recover time (s)	Reference
VS_2	35	31	*Adv. Mater.* **24**, 1969-1974 (2012) [8]
2H MoS_2	10	60	*Adv. Mater.* **29**, 1702076 (2017) [9]
2H MoS_2	300	600	*ACS Nano* **7**, 4879-4891 (2013) [10]
Graphene/Silk	3	6	*Adv. Funct. Mater.* **29**, 1808695 (2019)[11]
Graphene Oxide	1.4	10	*Adv. Mater.* **27**, 1370-1375 (2015)[12]
Graphene Fiber	180	125	*Small* **14**, 1703934 (2018)[13]
Paper	600	1500	*Angew. Chem. Int. Ed.* **55**, 5727-5732 (2016)[14]
MXene	1	201	*ACS Sens.* **4**, 1261-1269 (2019)[15]
MXene/Ag	5	80	*Adv. Funct. Mater.* **29**, 1905197 (2019).[16]
MXene	1000	2000	*Adv. Mater.* **33**, 2104878 (2021)[17]
Graphene	40	20	*Adv. Mater.* **33**, 2100218 (2021)[18]
PEDOT:PSS	1	4	*Sci. Adv.* **6**, eaba0931 (2020)[19]
Graphene Oxide	170	190	*Adv. Mater.* **28**, 2601-2608 (2016).[20]
Al/PI	1.5	50.6	*Nat. Commun.* **9**, 244 (2018)[21]
Perovskite	5	5	*Adv. Funct. Mater.* **30**, 1907449 (2020)[22]
Cleancool/Cu fiber	3.5	4	*Adv. Funct. Mater.* **29**, 1904549 (2019)[23]
Graphene Oxide	4.5	5.5	*Adv. Mater.* **28**, 3549-3556 (2016)[24]
TiO_2	45	200	*Adv. Mater.* **30**, 1705925 (2018)[25]
SnS_2/rGO	6	15	*Nano Energy* **67**, 104251 (2020)[26]
MXene/Cellulose	20	70	*ACS Nano* **15**, 16811-16818 (2021)[27]
GO/SF	1.05	0.8	*Nat. Commun.* **13**, 5416 (2022)[28]
1T′-WS_2	**0.30**	**1.20**	**This work**
2H-WS_2	**0.48**	**0.32**	**This work**

Supplementary References

1 Lin, Z. Y. *et al.* Solution-processable 2D semiconductors for high-performance large-area electronics. *Nature* **562**, 254-258, doi:10.1038/s41586-018-0574-4 (2018).

2 Leng, K. *et al.* Phase Restructuring in Transition Metal Dichalcogenides for Highly Stable Energy Storage. *ACS Nano* **10**, 9208-9215, doi:10.1021/acsnano.6b05746 (2016).

3 Zhu, K. X. *et al.* Solution-Phase Synthesis of Vanadium Intercalated 1T'-WS_2 with Tunable Electronic Properties. *Nano Lett.* **23**, 4471-4478, doi:10.1021/acs.nanolett.3c00826 (2023).

4 Fan, X. B. *et al.* Controlled Exfoliation of MoS_2 Crystals into Trilayer Nanosheets. *J. Am. Chem. Soc.* **138**, 5143-5149, doi:10.1021/jacs.6b01502 (2016).

5 Wang, Y. *et al.* Structural phase transition in monolayer $MoTe_2$ driven by electrostatic doping. *Nature* **550**, 487-491, doi:10.1038/nature24043 (2017).

6 Li, Y. *et al.* Structural semiconductor-to-semimetal phase transition in two-dimensional materials induced by electrostatic gating. *Nat. Commun.* **7**, 10671, doi:10.1038/ncomms10671 (2016).

7 Wang, Q. H. *et al.* Electronics and optoelectronics of two-dimensional transition metal dichalcogenides. *Nat. Nanotechnol.* **7**, 699-712, doi:10.1038/nnano.2012.193 (2012).

8 Feng, J. *et al.* Giant Moisture Responsiveness of VS_2 Ultrathin Nanosheets for Novel Touchless Positioning Interface. *Adv. Mater.* **24**, 1969-1974, doi:10.1002/adma.201104681 (2012).

9 Zhao, J. *et al.* Highly Sensitive MoS_2 Humidity Sensors Array for Noncontact Sensation. *Adv. Mater.* **29**, 1702076. doi:10.1002/adma.201702076 (2017).

10 Late, D. J. *et al.* Sensing Behavior of Atomically Thin-Layered MoS_2 Transistors. *ACS Nano* **7**, 4879-4891, doi:10.1021/nn400026u (2013).

11 Wang, Q. *et al.* Self-Healable Multifunctional Electronic Tattoos Based on Silk

and Graphene. *Adv. Funct. Mater.* **29**, 1808695, doi:10.1002/adfm.201808695 (2019).

12 Wang, X. W. *et al.* Exfoliation at the Liquid/Air Interface to Assemble Reduced Graphene Oxide Ultrathin Films for a Flexible Noncontact Sensing Device. *Adv. Mater.* **27**, 1370-1375, doi:10.1002/adma.201404069 (2015).

13 Choi, S. J. *et al.* Nitrogen-Doped Single Graphene Fiber with Platinum Water Dissociation Catalyst for Wearable Humidity Sensor. *Small* **14**, 1703934, doi:10.1002/smll.201703934 (2018).

14 Guder, F. *et al.* Paper-Based Electrical Respiration Sensor. *Angew. Chem. Int. Ed.* **55**, 5727-5732, doi:10.1002/anie.201511805 (2016).

15 Yang, Z. J. *et al.* Improvement of Gas and Humidity Sensing Properties of Organ-like MXene by Alkaline Treatment. *ACS Sens.* **4**, 1261-1269, doi:10.1021/acssensors.9b00127 (2019).

16 Liu, L. X. *et al.* Flexible and Multifunctional Silk Textiles with Biomimetic Leaf-Like MXene/Silver Nanowire Nanostructures for Electromagnetic Interference Shielding, Humidity Monitoring, and Self-Derived Hydrophobicity. *Adv. Funct. Mater.* **29**, 1905197, doi:10.1002/adfm.201905197 (2019).

17 Pazniak, H. *et al.* 2D Molybdenum Carbide MXenes for Enhanced Selective Detection of Humidity in Air. *Adv. Mater.* **33**, 2104878, doi:10.1002/adma.202104878 (2021).

18 Lu, L. J. *et al*. Flexible Noncontact Sensing for Human-Machine Interaction. *Adv. Mater.* **33**, 2100218, doi:10.1002/adma.202100218 (2021).

19 Wang, W. Y. *et al.* Inflight fiber printing toward array and 3D optoelectronic and sensing architectures. *Sci. Adv.* **6**, eaba0931, doi:10.1126/sciadv.aba0931 (2020).

20 Ho, D. H. *et al.* Stretchable and Multimodal All Graphene Electronic Skin. *Adv. Mater.* **28**, 2601-2608, doi:10.1002/adma.201505739 (2016).

21 Hua, Q. L. *et al.* Skin-inspired highly stretchable and conformable matrix networks for multifunctional sensing. *Nat. Commun.* **9**, 244, doi:10.1038/s41467-017-02685-9 (2018).

538 22 Cho, M. Y. *et al.* Perovskite-Induced Ultrasensitive and Highly Stable Humidity
539 Sensor Systems Prepared by Aerosol Deposition at Room Temperature. *Adv.*
540 *Funct. Mater.* **30***,* 1907449, doi:10.1002/adfm.201907449 (2020).
541 23 Ma, L. Y. *et al.* Full-Textile Wireless Flexible Humidity Sensor for Human
542 Physiological Monitoring. *Adv. Funct. Mater.* **29**, 1904549,
543 doi:10.1002/adfm.201904549 (2019).
544 24 Hu, K. S. *et al.* Self-Powered Electronic Skin with Biotactile Selectivity. *Adv.*
545 *Mater.* **28**, 3549-3556, doi:10.1002/adma.201506187 (2016).
546 25 Shen, D. Z. *et al.* Self-Powered Wearable Electronics Based on Moisture
547 Enabled Electricity Generation. *Adv. Mater.* **30***,* 1705925,
548 doi:10.1002/adma.201705925 (2018).
549 26 Zhang, D. Z. *et al.* High-performance flexible self-powered tin disulfide
550 nanoflowers/reduced graphene oxide nanohybrid-based humidity sensor driven
551 by triboelectric nanogenerator. *Nano Energy* **67**, 104251,
552 doi:10.1016/j.nanoen.2019.104251 (2020).
553 27 Li, P. D. *et al.* A $Ti_3C_2T_x$ MXene-Based Energy-Harvesting Soft Actuator with
554 Self-Powered Humidity Sensing and Real-Time Motion Tracking Capability.
555 *ACS Nano* **15**, 16811-16818, doi:10.1021/acsnano.1c07186 (2021).
556 28 Li, S. et al. Humidity-sensitive chemoelectric flexible sensors based on metalair
557 redox reaction for health management. *Nat. Commun.* **13**, 5416,
558 doi:10.1038/s41467-022-33133-y (2022).
559

2D materials

https://doi.org/10.1038/s44160-024-00702-6

Programmable phase switching and exfoliation

Qingdong Ou & Qiaoliang Bao

An electrochemical Li^+ intercalation-based exfoliation strategy achieves phase-switchable exfoliation of 2H- and 1T′-WS_2 nanosheets.

Phase engineering involves the manipulation of atomic arrangements in materials and enables the modulation of properties and functionalities[1]. Unconventional phases can endow nanomaterials with different properties compared to their bulk counterparts, making them promising for a variety of applications[2]. 2D group-VI transition metal dichalcogenide (TMD) nanosheets with various phases (such as 2H, 1T, 1T′), which originate from the coordination geometries of the transition metal atom, have attracted research interest owing to their unique physicochemical properties[3]. The stable 2H phase TMDs exhibit semiconductive properties with tunable bandgaps and are well suited for nanoelectronics and optoelectronics, while the metastable 1T and 1T′ phase TMDs possess metallic or semi-metallic properties with unconventional physicochemical properties and show high electrocatalytic activity[4]. A key challenge in the synthesis of phase engineered nanosheets for device application is to develop scalable strategies that precisely control the nanosheet phase.

The synthesis of 2D nanosheets can be split into two broad production strategies: bottom-up and top-down. In the bottom-up approach, atoms are assembled into 2D nanosheets and the morphology and size of the nanosheets can be controlled by applying rigorous deposition conditions or post-treatments. The obtained 2D nanosheets are mostly composed of a thermodynamically stable phase as the process is spontaneously initiated by Gibbs free energy[5], restricting the ability to engineer the phase. By contrast, the top-down method disassembles bulk materials into 2D nanosheets and is more versatile and applicable to large-scale production[6]. For example, by tuning different parameters during the exfoliation of bulk materials, 2D nanosheets with designated sizes, thicknesses and phases can be prepared. Previous studies have reported that the electrochemical intercalation exfoliation induces a phase transition in group-VI TMDs from 2H to 1T/1T′, as ion doping (accompanied with electron injection) stabilizes the 1T or 1T′ phase above the 2H phase[7]. However, the controllable synthesis of 2D nanosheets with designed phases remains elusive due to ambiguity in the phase transition mechanism.

Now, writing in *Nature Synthesis*, Gu, Li, Yu, Zeng and co-workers report a phase-switchable electrochemical approach to exfoliate 2H-WS_2 bilayer nanosheets and 1T′-WS_2 monolayer nanosheets from bulk 2H-WS_2 (ref. 8). A typical lithium battery configuration is implemented, where Li functions as the doping ion, driving the electrochemical intercalation process. Bulk 2H-WS_2 is coated on copper foil as the cathode and the Li foil anode provides Li^+ ions for intercalation (Fig. 1a). During the discharge process, Li^+ ions transfer from Li foil to WS_2 through the electrolyte (internal circuit), while electrons are transported through the external circuit, generating Li_xWS_2. By programming the discharge parameters, bulk 2H-WS_2 is intercalated by different amounts of Li^+ ions, producing different Li_xWS_2 phases (2H, 1T and 1T′, Fig.1b, c). Consequently, 2H-WS_2 bilayer nanosheets or 1T′-WS_2 monolayer nanosheets (Fig. 1d, e) can be exfoliated from Li_xWS_2 upon liquid-phase sonication.

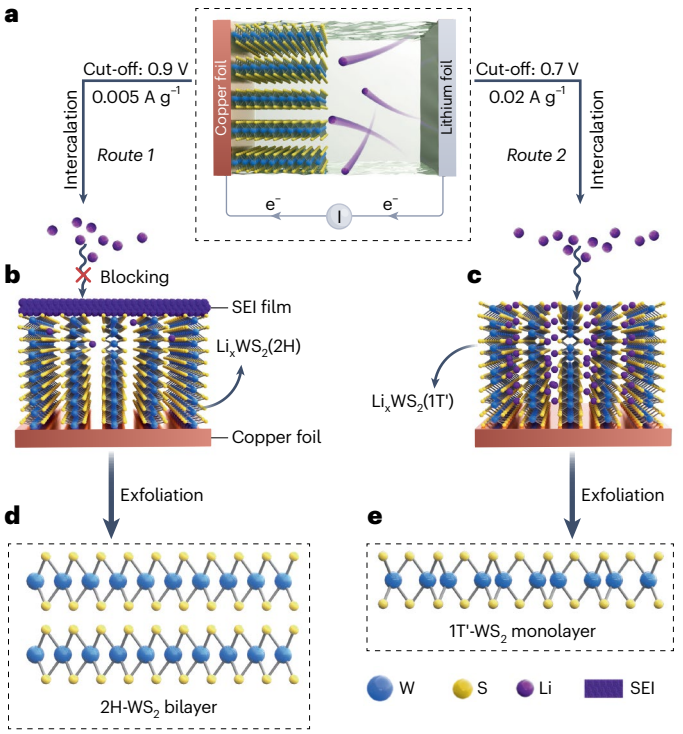

Fig. 1 | Phase-switchable synthesis of 2H- and 1T′-WS_2 nanosheets. **a**, Schematic illustration of electrochemical lithium intercalation of bulk 2H-WS_2 with different discharge current densities and cut-off voltages. The symbol "**I**" represents the discharge current. Route 1: a 0.9 V cut-off voltage and a 0.0005 A g^{-1} current density induce the formation of a solid electrolyte interface (SEI) film. Route 2: a 0.7 V cut-off voltage and a 0.02 A g^{-1} current density accelerates Li^+ intercalation. **b**,**c**, Different phases of lithium intercalated WS_2: 2H-Li_xWS_2 (**b**) and 1T′-Li_xWS_2 (**c**). **d**,**e**, Crystal structures of 2H-WS_2 bilayer nanosheet (**d**) and 1T′-WS_2 monolayer nanosheet (**e**).

The current density and cutoff voltage during the electrochemical Li^+ intercalation process serve as the switch (on–off) for triggering phase transition, leading to the transformation from bulk 2H-WS_2 to either 2H-WS_2 bilayer nanosheets or 1T/1T′-WS_2 monolayer nanosheets. Route 1 (Fig. 1a, left hand side), with a small discharge current density (0.005 A g^{-1}) and a high cutoff voltage (0.9 V), induces the formation of pure 2H-WS_2, while Route 2 (Fig. 1a, right hand side), with a larger

current density (0.02 A g^{-1}) and a lower cutoff voltage (0.7 V), will lead to a mixture of 1T-WS_2 (33%) and 1T′-WS_2 (67%).

The phase-switching mechanism is examined using atomic-scale characterizations and computational simulations. Gu, Li, Yu, Zeng and co-workers find that the appearance of a solid electrolyte interface (SEI) film on the cathode directly influences the Li^+ intercalation degree, causing the formation of different WS_2 phases. Li^+ intercalation through Route 1 with a small discharge current density induces the formation of a dense SEI film at the edge of the bulk 2H-WS_2 coated copper foil, suppressing Li^+ insertion below the phase transition threshold, therefore maintaining the original 2H phase. In contrast, Route 2 with a large discharge current density enables Li^+ to fully insert into WS_2 as no obvious SEI film is formed, inducing the phase transition from 2H to 1T/1T′.

The properties of TMDs are highly phase dependent. Compared to semiconductive 2H-WS_2, 1T′-WS_2 derived from metastable 1T-WS_2 maintains thermal stability by distorting the atomic arrangement, exhibiting semi-metallic properties[9]. The distorted octahedral coordinated 1T′-WS_2 has a higher electrical conductivity and a more active basal plane than that of 2H-WS_2, making adsorption of water molecules easier on 1T′-WS_2. As a proof of concept for material application, Gu, Li, Yu, Zeng and co-workers fabricated humidity sensors using the two exfoliated phases of WS_2. Given the different adsorption energies of 2H-WS_2 and 1T′-WS_2 towards water molecules, the 2H-WS_2 sensors exhibit a faster recovery time, while the 1T′-WS_2 sensors show a faster response time. These results validate the feasibility of this programmable electrochemical exfoliation methodology in tailoring different WS_2 phases to regulate their physicochemical properties. This advance is expected to promote applications in additional fields such as electrocatalysis, where catalytic activity is dependent on the phase-related properties.

This methodology demonstrates a pathway for synthesizing 2D TMDs with on-demand phases and provides a different perspective for manipulating phase transitions. The methodology developed here may be applied to other 2D TMDs such as MoS_2, $MoSe_2$ and WSe_2 as they possess similar layered structures and phase transitions. Assisted by artificial intelligence, the exploration of material phases that are previously difficult to synthesize, or the creation of new material phases, could be examined with this methodology. This precise control over phase transition in 2D TMDs offers a versatile and expansive platform for potential optoelectronic applications, including biosensors, photodetectors and nanophotonic circuits.

Qingdong Ou [1] ✉ **& Qiaoliang Bao** [2,3] ✉

[1]Macao Institute of Materials Science and Engineering (MIMSE), Faculty of Innovation Engineering, Macau University of Science and Technology, Taipa, Macao, China. [2]Institute of Energy Materials Science (IEMS), University of Shanghai for Science and Technology, Shanghai, China. [3]Hunan Key Laboratory for Micro-Nano Energy Materials and Devices, School of Physics and Optoelectronics, Xiangtan University, Hunan, China.

✉e-mail: qdou@must.edu.mo; qiaoliang.bao@usst.edu.cn

Published online: 5 December 2024

References

1. Chen, Y. et al. *Nat. Rev. Chem.* **4**, 243–256 (2020).
2. Shi, Z. et al. *Natl Sci. Rev.* **11**, nwae289 (2024).
3. Lai, Z. et al. *Nat. Mater.* **20**, 1113–1120 (2021).
4. Sokolikova, M. S. & Mattevi, C. *Chem. Soc. Rev.* **49**, 3952–3980 (2020).
5. Xu, L., Liang, H.-W., Yang, Y. & Yu, S.-H. *Chem. Rev.* **118**, 3209–3250 (2018).
6. Wang, J., Manga, K. K., Bao, Q. & Loh, K. P. *J. Am. Chem. Soc.* **133**, 8888–8891 (2011).
7. Li, W., Qian, X. & Li, J. *Nat. Rev. Mater.* **6**, 829–746 (2021).
8. Mei, L. et al. *Nat. Synth.* https://doi.org/10.1038/s44160-024-00679-2 (2024).
9. Song, X. et al. *Sci. Adv.* **9**, eadd6167 (2023).

Competing interests

The authors declare no competing interests.